Behavior of Concrete Filled Steel Tube (CFST) Under Different Loading Conditions

BEHAVIOR OF CONCRETE FILLED STEEL TUBE (CFST)

UNDER DIFFERENT LOADING CONDITIONS

by

Suliman Hassan Abdalla

A Thesis Presented to the Faculty of the
American University of Sharjah
College of Engineering
in Partial Fulfillment
of the Requirements
for the Degree of

Master of Science in
Civil Engineering

Sharjah, United Arab Emirates

June 2012

Approval Signatures

We, the undersigned, approve the Master's Thesis of Suliman Hassan Abdalla

Thesis Title: Behavior of Concrete Filled Steel Tube (CFST) Under Different Loading Conditions.

Signature	**Date of Signature**
_____	_____
Dr. Farid Abed Associate Professor, Department of Civil Engineering Thesis Advisor	
_____	_____
Dr. Mohammad AlHamaydeh Assistant Professor, Department of Civil Engineering Thesis Co-Advisor	
_____	_____
Dr. Salah Al-Toubat Associate Professor, Department of Civil and Environmental Engineering, University Of Sharjah Thesis Committee Member	
_____	_____
Dr. Rami Haweeleh Associate Professor, Department of Civil Engineering Thesis Committee Member	
_____	_____
Dr. Jamal Abdalla Head, Department of Civil Engineering	
_____	_____
Dr. Hany El-Kadi Associate Dean, College of Engineering	
_____	_____
Dr. Yousef Al-Assaf Dean, College of Engineering	
_____	_____
Dr. Khaled Assaleh Director of Graduate Studies	

Acknowledgement

First of all, I would like to thank Allah the almighty for his blessings that enabled me to achieve such great accomplishment in my life.

Then, my special gratitude to my main advisor Dr. Farid Abed for his tremendous support, kindness and patience through the course of this program. His background in structural analysis and finite element modeling were my guide before, through and hopefully after concluding my thesis. Special thanks to my co-advisor Dr. Mohammad AlHamaydeh for his advices and suggestions that relates to the core of my topic. Of course, I am greatly grateful to my committee members Dr. Rami Hawileh and Dr. Salah Al-Toubat for their efforts and recommendations to improve my dissertation. Special thanks to all the lab instructors that helped me carrying on the huge testing program such as Mr. Arshi, Mr. Salman, Mr. Aqeel and Mr. Ansari. Also, I would like to thank DAFCO ready mix company for their great support specially their manager Mr. Mohammad.

I also would like to thank all my friends who stood by my side all though this period specially: Abdulwahab, Gaith Al-Shamsi, Gaith Al-Gaith, Hyder, Adi, Muhannad, Reem, Alaa, Ayman Zain, Ahmad Hamid, Mohammad Bahtiti, Ahmad Ghadban, Ahmad Salama, Fadi Samir, Fadi Qanadilo, Agiad, Rami, Ayman Hilal, Esam, Omar osgi, Rana, Mohammad Azmi, Mohammad Irfan, Khalid, Saja and Nourhan.

From the deepest corners of my myogenic muscular which pumps blood throughout my blood vessels, to all my family members and friends, I say in every language known to man: شُكْرًا, Thank you, Hontōni arigatō (本当にありがとう), 谢谢, Hvala, Merci, Danke, शुक्रिया, спасибо, شکریہ کا آپ, Дзякуй, Salamat, σας ευχαριστώ, Go raibh maith agat, Gracias, teşekkür ederim.

Dedication

I would like to thank my family whom this work is dedicated to. Above all, thanks to my parents Hassan and Fadwa who were the source of my keep high spirits throughout this tough program. Also thanks are due to my brother Ahmad, sisters Dana and Lina and my brother-in-law Raed who always cheered me up when I needed it the most. Finally, thanks to future wife for being the hope that kept me going till the end.

لو أنني أوتـيت كل بلاغـــــة وأفنيت بحر النطق في النظم والنثر

لمـا كنت بعد القول إلا مقصرا ومعترفا بالعجز عن واجب الشكـر

Abstract

Concrete Filled Steel Tubes (CFSTs) were used in construction in the early 1900's. However, the research into CFSTs did not begin until the 1960s. From that time onwards, several studies were conducted on the CFSTs to fully understand their behavior with the aim of improving their performance. The proposed research presents an experimental study to investigate the effect of some the main influencing factors on the compressive behavior of circular CFST columns. The parameters of interest are mainly the concrete's compressive strength, the diameter-to-thickness ratio ($^{D}/_{t}$) and the loading rates. The testing program includes two concrete's compressive strengths of 44MPa and 60MPa, three ($^{D}/_{t}$) ratios of 54, 32, and 20, and two relatively low loading rates of 0.6 and 60 kN/sec. A nonlinear finite element (FE) numerical model using the commercial finite element software ABAQUS is also developed and verified using the proposed experimental results. It was found that the effect of ($^{D}/_{t}$) ratio on the compressive behavior of the CFST column is greater than the effect of the other factors. In addition, the CFST specimens' stiffness is greatly influenced by the ($^{D}/_{t}$) ratio as compared to the influence of the concrete infill compressive strength or the loading rate. The compressive behavior of Confined Concrete Filled Steel Tubes (CCFSTs) is also investigated in this research. A CCFST can be defined as a CFST column jacketed with FRP sheet such that its fibers are aligned long the column's hoop direction. The type of FRP-wraps used for jacketing in this study is glass based FRP material. CCFST samples with two different concrete infill compressive strengths of 44MPa and 60MPa and three ($^{D}/_{t}$) ratios of 54, 32, and 20 are tested under a loading rate of 60KN/sec. It was noticed that the dominant failure mode is the explosive rapture of the wraps in the mid-height region of the columns.

Search Terms: CFST; Confined concrete filled steel tube; CCFST; Axial load behavior; Ultimate capacity; Confinement effect; Loading rate; Nonlinear analysis; Strain rates; Composite column; Diameter-thickness ratio; Finite elements analysis

Table of contents

List of figures

List of tables

List of abbreviations

A_c : Area of the concrete infill in the CFST section (mm^2)

A_s : Area of the steel tube in the CFST section (mm^2)

D : CFST, CCFST or hollow steel section's outer diameter (mm)

D_u: Ultimate displacement of the tested specimen (mm)

D_y: Linear limit state displacement of the tested specimen (mm)

$(EI)_{eff\ k}$: Bending stiffness of the composite section about the buckling axis considered.

f_1 : Effective lateral confining stress on the concrete.

f_c' : Unconfined concrete cylinder compressive strength.

f_{cc}' : Confined concrete compressive strength.

γ_c : Concrete material partial safety factor, taken 1.3.

γ_{Ma} : Structural steel material partial safety factor, taken 1.

I_c : Moment of inertia of the concrete infill in the CFST section (mm^4)

I_s : Moment of inertia of the steel tube in the CFST section (mm^4)

K : Effective length factor and it is taken as 1 in this study.

K_e : Correction factor for cracking of concrete, which may be taken as 0.6

L : Laterally unbraced length of the member (mm)

L_{fl} : Buckling length of the column, taken as specimen height.

N_{cr} : Elastic critical load of a composite column and calculated using the usual Euler buckling equation.

$N_{pl.Rk}$: Value of the plastic resistance $N_{pl.Rd}$ calculated using material partial safety factors γ_{Ma} and γ_c set equal to 1.0.

P_e : Elastic critical buckling load (kN)

P_{no} : Nominal compressive strength of axially loaded composite member (kN)

t : Structural steel tube thickness (mm)

Chapter 1: Introduction

1.1 Significance of Research

At the present time, the concrete filled steel tube columns are widely used in construction. Actually, this type of structural elements is favored in practice because of its small cross sectional area to load carrying capacity ratio. Hence, mega concrete columns in tall buildings' lower floors can be substituted by smaller sections of CFST columns. Moreover, CFST elements can be used as piers for bridges at congested areas. Therefore, such structural elements should be thoroughly investigated before used in critical structures. Despite being a research topic for around 50 years, the behavior of the CFST columns under different loading conditions is not fully studied. Thus, intensive parametric studies should be performed in order to fully understand the CFST columns behavior. This study, addresses some parameters that affect the CFST column behavior which are the steel tube outer diameter to thickness ratio, the concrete infill compressive strength, the loading rate, and the GFRP jacketing.

1.2 Objectives

1. Conduct an experimental testing program to study the performance of concrete filled steel tubes considering several parameters such as:
    a. The compressive strength of the concrete infill.
    b. The steel tube outer diameter to thickness ratio.
    c. The loading rate.
    d. The GFRP jacketing.
2. Develop a finite element model using ABAQUS and verify it using the experimental results.
3. Compare test results to theory and some codes formulae to illustrate their accuracy, such as:
    a. Theoretical formulae.
    b. American Institute of Steel Construction code formulae (AISC).
    c. ACI 318 and AS codes formulae.
    d. Giakoumelis G. and Lam D. formulae.
    e. Mander et al. formulae.
    f. Eurocode 4 formulae.

1.3 Background

Steel-concrete composite columns were used for over a century. At the beginning it was used to provide fire protection to steel structures. Afterwards, the concrete encased columns' strength properties were also considered in the design. However, the research into concrete filled steel tubes (CFST) did not begin until the 1960s [1].

Nowadays, the composite structural elements are increasingly used in tall buildings, bridges and other types of structures. Because of its composite effects, the disadvantage of two materials can be compensated for and the advantages can be combined providing efficient structural system. The steel-concrete composites are considered as an advantageous system for carrying large axial load benefitting from the interaction between the concrete and the steel section. The steel section reinforces the concrete to resist any bending moments, tensile and shear forces. The concrete in a composite column reduces the potential for buckling of the steel section in addition to resisting compressive loading. There are two types of steel-concrete composite columns which are commonly used in buildings. Those with steel section in-filled with concrete and those with steel section encased with concrete as shown in Figure 1.

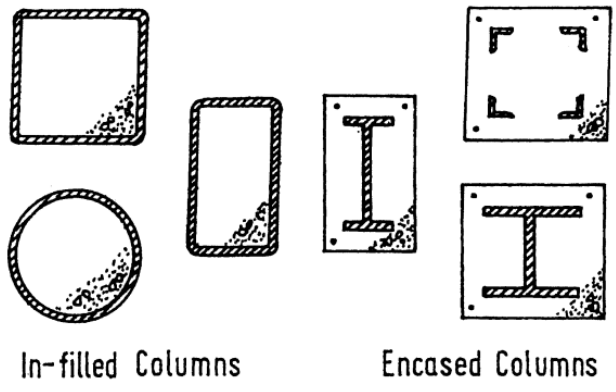

Figure 1: Types of composite column [2]

The use of composite columns, encased or in-filled, results in significant reduction of the column size when compared to regular reinforced concrete columns needed to carry the same load. Hence, considerable economic savings can be obtained. Also, the column size reduction is advantageous where floor space is at a premium, such as in office blocks and car parking's. In addition, closely spaced composite columns connected with spandrel beams can be used around the outsides of the high rise buildings for lateral loads resistance by the tabular concept [1].

Concrete encased steel composite sections are favored for many seismic resistant structures. When the concrete encasement cracks under severe flexural overloading, the stiffness of the section reduces but the steel core provides shear capacity and ductile resistance to subsequent cycles of overload. Additionally, the surface area of the enclosed steel sections is intact by the concrete cover, thus required no painting and fireproofing costs. Concrete filled steel tube (CFST) columns are favored for many earthquake resistant structures, columns in high rise buildings, bridge piers subject to high strain rate from traffic and railways decks. Concrete filled steel tubes necessitate supplementary fire resistant insulation if fire protection of the structure is crucial. The CFST structures have better constructability because the steel tubes can be used as the formwork and the shoring system for casting concrete in construction. Moreover, CFSTs provide high compressive and torsional resistance about all axes when compared with concrete encased steel composite sections.

1.3.1 Concrete filled steel tube

1.3.1.1 Behavior during loading:

In the initial concentric axial loading stages of the CFST column, both concrete infill and structural steel will deform longitudinally. Of course, it is assumed that the concentric loading is

applied uniformly across the CFST section. The Poisson's ratio of the concrete infill (ranges between 0.15-0.25) is smaller than that of structural steel (roughly 0.28) at these initial strains. Thus, the lateral expansion of the confining tube is larger than the confined concrete. As a result, localized separation between the two composite materials takes place along the column. Moreover, minimal interaction between the two materials occurs if any. The concrete and the steel bear their shares of the applied load independently during this phase.

At a certain strain, the expansion of the concrete infill laterally increases until it reaches the lateral expansion of the steel. Keep in mind that the structural steel expansion remains constant in this stage and micro-cracking in the concrete begins to take place. This acceleration in the concrete expansion results in an interactive contact between the two materials. Hence, bond stresses are developed and the concrete will be subjected to tri-axial stresses while the structural steel to biaxial stresses [3]. Longitudinal stress in the confining tube varies based on the transfer of force between the concrete and steel. The strain level at which confinement occurs is debated among researchers to range from 0.001 to 0.002. Some scientists such as Knowles and Park concluded that concrete confinement happens suddenly at a about $0.95\,f_c'$ (strain of 0.002) just as the concrete starts dilation [4]. While other researchers as Tsuji, et al. and Zhang, et al. proposed a steady increase in the concrete confinement starting right after the occurrence of micro-cracking in the concrete (strain of 0.001), till full confinement is met at a strain around 0.002 [5], [6].

In the second stage of loading where the confinement of the steel tube on the concrete is present, circumferential stresses are developed in the structural steel due to two factors:

1. Longitudinal stresses from loading.

2. Lateral pressure from concrete dilation.

Based on the steel utilized in the composite element, the steel could have reached its capacity prior to their yield in this stage. If tube yielding occurs before this biaxial state of stress, the tube would not be able to sustain the normal yield stress, resulting in a transfer of load from tube to the concrete core. Conversely, if the confining tube has not yet yielded, the extra axial capacity needed from the steel tube before yielding will be reduced [7]. Unlike the effect biaxial state of stress on the steel tube capacity, the concrete infill performance enhances when experiencing tri-axial state of stress. The presence of confinement on the concrete infill increases its axial capacity. Despite the decrease in its steel tube capacity, the circular CFST column's overall capacity increases because the increase in the concrete infill capacity due to confinement is far greater than the strength loss in the steel tube.

1.3.1.2 Failure modes:

There are various modes of failure for the CFST based on their material properties and geometric configuration. However, the most dominant failure mode is the local buckling of the steel tube. When compared with the empty steel tube, the local buckling in the CFST column is delayed due to the presence of concrete infill. The concrete prevents the steel tube from buckling inward; instead it forces the tube to buckle in an outward mode as shown in Figure 2.

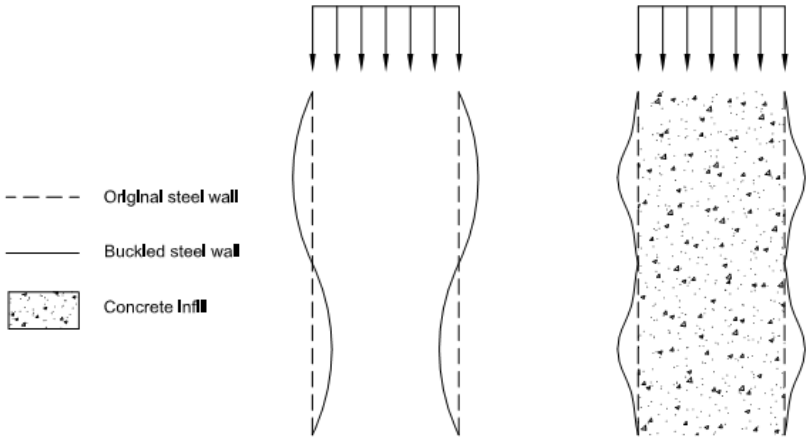

Figure 2: Changes in buckling mode with length due to the presence of infill [8]

The outward buckling mode of the steel tube has three advantages for the behavior of the CFST element:

1. The delay in tube buckling keeps the steel in the elastic range longer which often allows for the yield stress to develop before buckling.
2. The element modulus does not decrease rapidly during this type of failure because the distance between the cross section's edges increases.
3. The localized steel tube buckling is forced to spread over a larger region of the column height limiting the occurrence of strain concentrations.

1.3.1.3 Shapes of CFST elements:

There are several shapes for the concrete filled steel tubes based on the confining steel tube's shape, such as rectangular, elliptical, circular, square, L-shaped,…etc. Circular and square sections of CFSTs are the widely used ones in construction. The load carrying capacity of CFST column is considerably affected by the shape of its cross section, diameter-to-thickness and width-to-thickness ratios of the steel tube. When static load is applied, the deformation for circular CFST columns experience elastic-perfectly-plastic or strain-hardening behavior after

yielding. On the other hand, hollow structural steel columns exhibited a degrading type load deformation curve after yielding under the same loading.

1.3.1.4 Advantages and disadvantage of CFST columns:

A designer could think of using larger steel cross sections instead of composite section in order to avoid complexity of construction. Or even mega RC column in high rise buildings. However, the bare steel sections and RC columns have several drawbacks that can be addressed by using steel-concrete composite columns, such as:

1- Maintenance costs: when exposed to air and humidity, the steel structures are vulnerable to corrosion, thus they have to be painted periodically. This issue occurs in the case of CFST structures but not in the encased concrete composite element because the steel section is protected by the surrounding concrete.
2- Buckling failure: the steel sections are considered economical because of their low strength to weight ratio. However, with the increased slenderness of the steel column the carrying capacity decreases because of the buckling failure domination. In the composite columns the concrete delays the buckling when compressively loaded which enhances the capacity of the element. Also, thinner steel section would be required in the presence of concrete thus the cost is reduced.
3- Fireproofing costs: the steel sections has high load carrying capacity at normal range temperatures, but its strength reduces immensely when exposed to high temperatures, thus fireproofing is essential. This issue occurs in the case of CFST structures but not in the encased concrete composite element because the steel section is protected by the surrounding concrete.

4- Constructionability: the structural steel tube in the CFST performs as in-place framework. Of course, fixing the steel tube for casting concrete is much easier and less time consuming than fixing and removing frame work. Also, the presence of steel tube minimizes the need for rebar fixing which is one of the most tedious work packages in the RC construction.

5- Ecology: the reduction in wood consuming needed for the formwork is environmentally advantageous. Also, it is much easier to reuse the concrete and the steel of CFST elements compared to regular RC members.

6- Cost: due to the previously mentioned reasons the cost of using CFST member in construction is more attractive than many other alternatives. For instance the reduction in labor cost needed for reinforcement fixing or removable frameworks.

1.3.2 Confined Concrete Filled Steel Tubes

1.3.2.1 FRP jacketing technique:

Jacketing technique is one of the conventional methods used for strengthening and retrofitting existing and new columns and piers. This method is performed by strengthening targeted location along the column's height using steel, concrete or FRP materials. The use of FRP wraps as a jacket base for the column has many advantages over the other materials such as:

1. The FRP material -carbon or glass based- has a great corrosion resistance unlike the structural steel, as will be illustrated in detail later in this chapter.
2. Compared to both steel and concrete, the FRP has a very high strength to weight ratio and shape flexibility.

3. The usually used FRP wraps in jacketing are unidirectional unlike the steel and concrete, thus it does not get affected by axial stress and offer better hoop directional confinement.

1.3.2.2 FRP jacket applied on concrete filled steel tube:

The concrete infill in the CFST column forces the outward buckling of the steel tube to occur. If the FRP jacket is applied on the CFST element, the outward buckling of the tube will be delayed. As a result, the performance of the entire section will be further enhanced. The first to propose this FRP jacketing technique to the CFST columns was Xiao in 2005 and named it confined concrete filled steel tube (CCFST). In the same year and as extension of Xiao's concept, the effect of FRP-wrapping on the local buckling of the structural steel tubes was studied at The Hong Kong Polytechnic University by Teng and Hu [9]. Studies on similar concepts were later performed by different scholars such as Shaat, et al. in Canada [10] and Nishino, et al. in Japan [11] where hollow steel tubes were wrapped with FRP jackets. The researchers' interest in such concept resulted from the enhancement of its composite action behavior.

1.3.2.3 Fiber reinforced polymer (FRP):

FRP material in itself is a composite that consists of fibers, which are chosen from a wide range of materials such as carbon, aramid and glass, which reinforce the polymer matrix. Some of the materials used for the polymer matrix are polyester thermosetting plastic, epoxy and phenol formaldehyde resins [12]. The FRP material composes of mainly four elements. First, the reinforcing fibers are used to carry and withstand all the applied loads and stresses. Second, the resins are added to allow for load transformation among the fibers in addition to gluing these

fibers together and shielding environmental effects. Third, the modifiers are additives used in the FRP composition to enhance the polymers' performance and to increase its lifetime. Forth, the fillers not only replace the unneeded resin in the composition but also to control the final product's shrinkage as well as increase its cracking resistance.

With its components variety, the FRP is used in construction with different forms. For instance, they can be used as reinforcing bars, externally attached plates, wrapping sheets or a combination of these forms as shown in Figure 3. The FRP-wraps are manufactured unidirectional and multidirectional by aligning their fibers along one access or two accesses where the load will be resisted.

Figure 3: forms of FRP usage in construction [13], [14], [15]

Recently, the use of FRP material for retrofitting existing structure or for new structures has been favored by designers because of its properties. Listed below are some of the advantages of FRP wraps over commonly used materials in construction such as steel and concrete:

1. High strength-to-weight ratio: the FRP-wraps are almost two times stronger and twenty percent lighter [16].
2. Flexible fibers orientation: as mentioned previously, the FRP-wraps can be manufactured such that its fibers have a unidirectional orientation. Hence, the user can apply

these wraps to the structure flexibly to meet its requirements. In other words, if the flexural failure or the shear cracking is the dominant mode of failure, the FRP-wraps can be fixed such that its fibers are aligned along the anticipated cracking line resulting in enhanced resistance to the deformation of the fibers and an increase in the resisted load.

3. Corrosion resistance: generally, the FRP-wraps are considered good corrosion resistant. It should be noted that some FRP materials have better corrosion and chemical resistant than other based on their components such as the resin [17].
4. Low overall cost of FRP-wraps: when used in construction, the FRP-wraps main drawback is its high material price. Nevertheless, it should be noted that the prices of the material in the composite retrofit is relatively small to the overall cost and recently the price per weight of fibers has been dropping [16]. In addition, the FRP retrofit application is easier in construction than steel and it does not corrode as fast also as discussed previously. Hence, the installation and maintenance costs of FRP retrofitting are cheaper than other options.
5. Strong glass-FRP: compared with other types of FRP, the glass based FRP are the best for deformation resistance and considered to be the strongest when its fibers are fixed along the force line. On the other hand, if the fibers are fixed such that the force line is perpendicular to them, the glass-FRP would perform the poorest compared to the other types. Thus, its application should be carefully studied and designed.

It is shown in Table 1 the matrix martials used along some of the most commonly used fibers as reinforcements in FRP material. In addition, some of the major enhanced properties are presented.

Table 1: comparison between different types of FRP fibers [18]

Reinforcing Material	Most Common Matrix Materials	Properties Improved
Glass Fibers	UP, EP, PA, PC, POM, PP, PBT	Strength, Elasticity, Heat resistance
Wood Fibers	PE, PP, ABS, HDPE, PLA	Flexural strength, Tensile modulus, Tensile Strength
Carbon and Aramid Fibers	EP, UP, VE, PA	Elasticity, Tensile Strength, Compression strength, Electrical strength.
Inorganic Particulates	Semi-crystalline Thermoplastics, UP	Isotropic shrinkage, Abrasion, Compression strength

1.3.3 Loading rate effect

The deformation of materials when high strain rate loading is applied varies significantly from static or qui-static to dynamic loading conditions. It was observed that with the increase of the applied strain rate loading the ultimate strength of the material increases as shown in Figure 4. This phenomenon resulted from the fact that the type of microstructure has an influencing rule in controlling the movement during inelastic deformation in the material. The loading rate dependency dominates for high loading-rate deformations at which stress flow creates significant changes in the material.

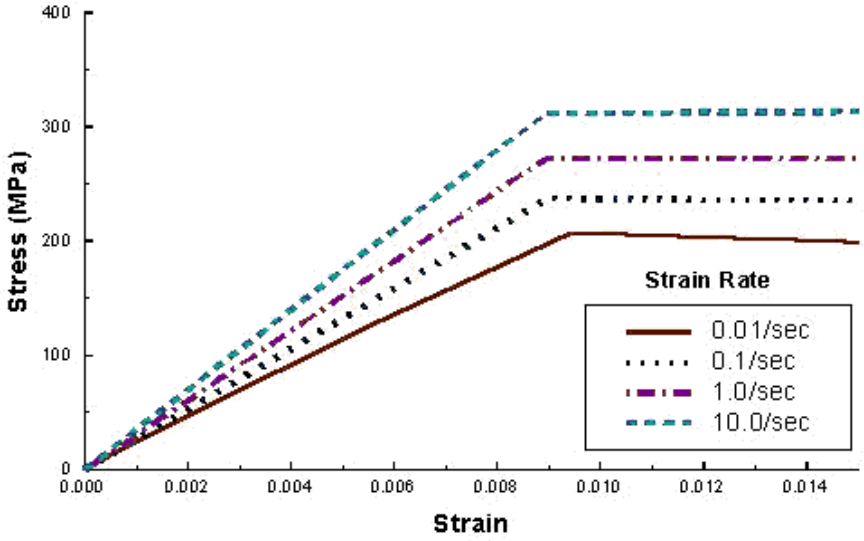

Figure 4: Rate dependence on the stress-strain curve for bone [19]

1.4 Literature Review

The first research attempt to study the structural behavior of concrete filled steel tube elements was made by Sewel [20] by conducting a test program on CFST, concrete and steel tube. Based on the test results, it was observed that the load bearing capacity of CFST columns is larger than the sum of steel and concrete capacities when individually tested. Additional studies on CFST columns were done by many researchers such as Klöppel and Goder [21], Salani and Sims [22], Neogi, et al. [23]. It was concluded that the increase in ultimate axial resistance of CFST columns results from the confining effect of steel tube on the concrete infill.

Prichard and Perry [24] tested 70 sleeved concrete filled cylinder tubes using a drop weight accelerated by gravity and described their response. The specimens were subjected to axial impact loading at different rates. Their analysis focused on the skin stresses, the deformational response and the contact forces of the tested cylinders. The concrete infill cylinders were 200mm high and approximately 100mm in diameter with strength capacity of $40N/mm^2$. These cylinders were confined with thin walled hollow tubes of PVC plastic, aluminum and steel. The plastic and the aluminum tubes thicknesses are 3.6mm and 3.25 respectively. For the steel tubes four thicknesses were considered 1.2 mm, 3 mm, 5 mm and 6.3 mm. Also, a set of unconfined concrete cylinders were impacted for comparative studies. Using the drop hammer test machine, the load is applied through the falling steel impactor under gravity onto the specimen placed below. The specimens were impacted at three contact velocities 3.2m/s, 4.4m/s and 6.3m/s corresponding to drop heights of O.5m, 1m and 2m respectively. To obtain the circumferential and longitudinal deformation profile of the specimens, around 26 strain gauges were attached horizontally and vertically around the outside surface of each

confining sleeve. It was concluded that providing additional lateral confinement to the minimum necessary to inhibit the dilation of the concrete will increase the maximum contact force. However, further increase to the thickness will not decrease the dilation by any significant degree. Also, the increase of contact forces among the confined specimens is associated with the increase of the stiffness of the confining materials. Nevertheless, the contact force and the confining materials' stiffness are not linearly proportioned.

O'Shea and Bridge [25] developed design methods which can be used to conservatively evaluate the strength of circular concrete filled steel tubes under several loading conditions. The loading conditions contained axial loading of the concrete only, axial loading of the steel only and concurrent loading of the concrete and steel axially along small eccentricities. The developed design methods have been calibrated and validated based on recent tests on circular concrete filled steel tubes. The infill concrete's nominal unconfined cylinder were of 50MPa, 80MPa, and 120MPa strengths. The test specimens were short with a diameter to thickness ratio ranging between 60 and 220 and a length to diameter ratio of 3.5. It was observed that the load carrying capacity of unfilled circular steel tubes is significantly affected by local buckling. Although the buckling strength of square tubes can be improved by providing internal lateral restraint, this was not observed in the examined circular steel tubes. Instead, the predominantly outward buckle remained unaffected by the internal concrete. Also, the loading condition greatly affects the degree of confinement provided by a thin walled circular steel tube to the concrete infill. The greatest confinement occurred when the CFST was axially loaded with only the concrete loaded while the steel tube acted as pure circumferential restraint. Moreover, local buckling of the confining steel tube does not happen if sufficient bond between the steel and concrete is present. Thus, the provisions of Eurocode 4 can be used without reduction for local buckling if concrete

infill strengths up to 80MPa. Eurocode 4 can be used without reducing the steel's strength from local buckling and biaxial effects and without enhancing the infill concrete for confinement. Finally, the authors pointed out that the current simplified methods can give very unconservative strength estimates if used outside their calibrated range. In addition, Eurocode 4 can use thin walled steel tubes filled with only very high strength concrete if the design equations are carefully formulated.

Hu, et al. [26] constructed a nonlinear finite element model for concrete filled steel tubes using ABAQUS and verified it against experimental data. The experimental data are extracted from previous researches by Schneider [27] and Huang, et al. [28]. The numerical analyses, the CSFT's are grouped based on the cross section into square sections, square sections stiffened by reinforcing ties and circular sections. The uniaxial behavior of CFT columns are studied and discussed based on the geometric properties of the columns and on the influence of the concrete confining pressure. The square sections were built by seam welding two U-shaped cold formed steel plates. For the stiffened square sections the tie bars were fillet welded to the U-shaped cold formed steel plates before making the seam complete penetration channel. The two testing programs contained six circular CFSTs, six squared CFSTs and twelve stiffened six squared CFSTs. The specimens' thicknesses varied from 2 mm to 7.5 mm. For the finite element model, only one eighth of the CFT column is modeled and analyzed because of symmetry in order to reduce the program's computational time. Based on the numerical analyses it was shown that the steel tubes can provide a good confining effect to the concrete infill in circular CFST columns particularly when the D/t ratio is small. The steel tubes for square CFST columns do not provide a large confining effect to the concrete infill particularly when the B/t ratio is large. And by the

use of reinforcing ties, the confining effect of stiffened square CFST columns is improved especially when the tie diameter is large and the tie spacing is small.

Shan, et al. [29] reported the impact behavior of CFT and CCFT stub columns. A confined concrete filled tube (CCFT) is a newly developed CFT system by Xiao [30]. Simply, it is CFT wrapped with one layer of carbon fiber sheet after saturating in epoxy. The impact responses of concrete filled steel tubes (CFT) and the confined concrete filled steel tubes (CCFT) were investigated using a high-speed gas gun. Also, a finite element model for the tested specimens was developed using ANSYS. The testing program contains two phases. In the first phase, CFT specimens were tested to provide benchmark data on impact behavior of Concrete Filled Tube columns. In the second phase, a study was done to compare CFT with CCFT stub columns. This comparison will help in observing the effectiveness of additional transverse confinement on improving the behavior of CFT columns. For a benchmark static data, static compression tests were also carried out for steel tube yield strength, concrete compressive strength and the static load capacity of CFT specimen. In each specimen, four sets of strain gages were fixed. The outer diameter of the confining steel tubes is 50mm with a thickness of 1mm. The measured impact velocities ranged from 186.5m/s to 49.1m/s. It is noticeable that under the same impact loading the CCFT strain is less than the CFT indicating the enhancement in resistance. Also, it was clear from the model that the impact wave was transferred as a unidirectional plane wave through the specimen. However, the predicted maximum strain using the model is less than that in the test results because the concrete damage is not considered in the material model.

Lama and Gardner [31] investigated the compressive behavior of concrete filled stainless steel columns with varying concrete infill strengths. They compared the compressive resistances

of these elements with the ones obtained from stainless steel hollow sections. Moreover, comparisons were made with existing design rules based on Eurocode 4 and ACI-318. Based on the Continuous Strength Method, New design expressions were developed to calculate the strength and contribution of the stainless steel. The testing program contained two cross-section types, square hollow sections (SHS) and circular hollow sections (CHS). The four different section sizes were SHS 100 × 100 × 5, SHS 100 × 100 × 2, CHS 114 × 6 and CHS 104 × 2. Four stub column tests were carried out for each size. Three out of the four were for concrete filled specimens with nominal concrete strengths of 30MPa, 60MPa and 100MPa. In addition, one test was for the empty stainless steel tube. Also, separate tests were performed to attain the constituent materials properties. A total of 16 stub column tests were executed - 8 SHS and 8 CHS - on specimens with 300mm height. Clamps were used at each end of the specimens in addition to a capping thin layer of plaster. Two vertically and one horizontally aligned strain gauges were attached to all stub columns at mid-height. Furthermore, two linear variable displacement transducers were placed either side of the stub columns for end shortening measurements. It was concluded that the current design guidance in the codes can be safely used for concrete filled stainless steel tubes despite being overly conservative especially for CHS. Additionally, the developed Continuous Strength Method provided accurate and consistent prediction of test capacity because of the assessment of the contribution of the stainless steel tube to the composite resistance.

Xiao, et al. [32] performed experimental studies on concrete filled steel tubes in addition to benchmark plain concrete cylinders for comparison under high strain rate loading using split Hopkinson pressure bar. The considered parameters in this paper are the ultimate strain, the dynamic compressive strength, the secant stiffness and residual strength. The dynamic increase

factor (DIF) of CFST was determined using logarithm linear fitting of the test results. The testing program contained thirteen specimens, nine concrete filled steel tubes and four plain concrete. The outer diameter of the confining steel tubes used for testing is 50mm with a thickness of 1mm. In order to obtain length to diameter ratio of 0.5, the height of the specimens was set to 25mm. Both surfaces of the tubes were carefully ground smoothly. Based on the materials property testing, the average yield strength of steel was found to be 337MPa and the concrete compressive cube strength to be 35MPa. Vertically and Horizontally aligned strain gauges were attached to all specimens. The applied strain rate during the impact test ranged from $81s^{-1}$ to $195s^{-1}$. To assure a controlled testing environment for the CFSTs, three sets of air pressure 0.5MPa, 0.8MPa, and 1.2MPa were chosen as control loading air pressures for propelling the striker bar. For the plain concrete samples only 0.5MPa and 0.8MPa were selected. It was found that CFST is appropriate for carrying impact loads because under the same impact loading the plain concrete specimens were entirely crushed while CFST specimens hold their shape with reduced physical damage. Also, the DIF of CFST specimens were smaller than that of a plain concrete specimen under the same strain rate impact. The significant amount of circumferential strain developed in the confining steel tube indicates the existence of an interaction mechanism between the concrete core and the steel tube.

Using a spilt Hopkinson pressure bar, Huo, et al. [33] impacted small sized micro concrete filled steel tubes under axial impact load at elevated temperatures up to $400^{o}C$ in their experimental study. The effect of elevated temperatures on the impact resistance of CFST and the failure patterns are analyzed. The stress and strain time history curves of the tested specimens were documented to investigate the impact behavior of CFST at high temperatures. The testing program contained sixteen concrete filled steel tube specimens. Out of these specimens, only one

was statically tested for comparative studies while the rest were axially impacted. The outer diameter of the confining steel tubes used for testing is 32mm with a thickness of 1mm. In order to obtain length to diameter ratio of 0.5, the height of the specimens was set to 16mm.The inner surface of the tubes were wire brushed to remove rust and loose debris. For materials property testing, three coupons were extracted from the steel tube and three 150 mm cubes were prepared. From these tests, the average yield strength of steel was found to be 313MPa and the concrete compressive cube strength to be 36MPa. A unique test setup was developed by fixing a specially designed electrical furnace to the SHPB bar to apply the impact load to the specimen after heating. The applied strain rate during the impact test ranged from $240s^{-1}$ to $288s^{-1}$. It was observed that there was no clear increase in load for the specimens at ambient temperature after the steel tube yielded, though the specimens at elevated temperatures displayed notable increase in load carrying capacity. Also, the strength of the CFST samples exposed to high temperature decreases to some degree, but the post yielding impact resistance would still increase under great axial deformation.

An experimental study on the behavior of circular CFST columns filled with self-compacting concrete and normal concrete concentrically loaded was presented by Yu, et al. [34]. The columns were concentrically loaded under compression up to failure. In their paper, they aimed to accomplish five main goals. First, explore the effect of three different measurement methods of the axial deformation of column samples. These measurement methods, which are adopted in literature, are: i) measurement of axial deformation of the column using electronic displacement transducers, ii) measurement of the steel tube external strains using strain gauges fixed at the mid height of the specimen, and iii) measurement of the axial deformation of steel tubes through electronic displacement transducers at the mid height of the sample. Second,

explore the effect of the concrete core strength on the CFST section's load capacity. Third, probe the influence of full perimeter notched slots and small notched holes of the confining tube on the element's load–deformation behavior, failure mode and ultimate capacity of CFST. Forth, compare the experimental results of the CFST elements with the calculated ultimate capacities using Eurocode 4. It should be noted that five different loading conditions were considered in this research to inspect different mechanical behaviors of CFST. The load was applied to: i) the entire section, ii) the concrete area firstly, then to the whole section after compressing the concrete infill, iii) the steel area firstly, then to the whole section after compressing the confining steel, iv) the concrete area only, v) the total sectional area while notched holes or slot were present in the mid height region of the confining tube. The testing program included a total of seventeen CFST samples. All test specimens had a height to diameter ratio of three to insure not only the minimization of the end effects but also the effects from slenderness. A 5 mm thick square steel plate was welded at the bottom of each specimen. All of the CFST samples were tested using a universal testing machine with a 5000 kN capacity. The loading rate ranged between 50 kN/min to 100 kN/min and each loading interval was maintained for 2–3 min. From the test results it was concluded that the confinement effects of the steel tube changed under varies loading conditions. The confinement effects took place earlier and were less in the third loading condition compared to the first loading condition. Also, the ultimate capacity for both conditions was nearly the same. On the other hand, during the second and forth loading conditions the confinement effects were enhanced but appeared later and the section's ultimate capacity increased a little bit. Throughout the first four loading conditions, the residual capacities of the CFST specimens were almost the same and hardly changed. Also, it was noted that a significant increase in the section's capacity was associated with the increase of the compressive

strength of concrete infill. However, the values of the residual capacity after failure were constant.

Liang, et al. [35] developed a nonlinear fiber element model of square CFST column elements. Their proposed model took the local buckling of the confining steel tube into account by embracing the effective width models. Also, the progressive local and post-local buckling was incorporated in the model through the redistribution of stresses within the confining steel tube gradually. For the material model of the concrete in the fiber model, Tomii's and Sakino's concept was adopted [36]. This concept states that the steel confinement effect increases the ductility of the concrete infill in CFST elements without affecting its strength. The material model proposed by Ramberg and Osgood was embraced in this nonlinear fiber element model for stresses calculations [37]. As known, post-local buckling is defined as the stress redistribution within the buckled steel plate when axial compression is applied. In this study, the principle of effective width was employed in order to account for the post local buckling. This concept is translated in the fiber element such that the effective steel fibers are stressed up to the yield strength, while the stresses of ineffective steel fibers are assumed to be zero. When comparing the fiber model output with the experimental data presented by Schneider [27], it was found that the mean predicted ultimate load for all specimens is 97% of the experimental results. Thus, the developed fiber model is capable of accurately predicting the load-strain relation of square CFST columns with local buckling effects.

Sakino, et al. [38] developed design formulae to evaluate the ultimate axial compressive capacities of the CFT columns. These formulae were based on the testing program of the 5 years research on CFST column that was performed as a part of the fifth phase of the U.S.-Japan Cooperative Earthquake Research Program. 114 CFT specimens were prepared and tested for

investigations on centrally loaded hollow and CFST short columns. Four main varying parameters were considered in this phase; the steel tube D/t ratio, steel tube tensile strength, steel tube shape and concrete infill strength. The average longitudinal strains were measured using four LVDTs that measured axial shortenings between the two load applying endplates. Also, a set of six strain gages were fixed on each sample, two at the mid height of the specimen and the others are at a distance D (diameter) far from the center. These strain gages were fixed to measure the longitudinal and the circumferential stains. Due to the wide range of specimens' sizes, it was essential to consider the scale effects on the axial compressive capacity of concrete. Thus, a scale reduction factor for the concrete compressive cylinder strength obtained from previous studies done by Blanks and McNamara was used in the formulae [39]. It should be noted that the scale factor is limited to circular columns. However, by considering square CFT columns as circular ones with similar sectional area, Blanks and McNamara's scale factor was applied to the square samples. It was concluded that the difference between the nominal squash load and the ultimate strength of circular CFST columns can be evaluated through a linear function of the tube yield strength. It should be noted that this difference is provided by steel confinement of the concrete infill.

Gupta, et al. [40] performed experimental and computational studies on the behavior of axially loaded circular concrete filled steel tubes columns. The experimental campaign consisted of eighty one specimens which were concentrically loaded till failure. Also, the computational analysis was performed using a Finite Element code ANSYS. The main objective of the developed nonlinear finite element model was to investigate the load carrying mechanism of CFSTs. The four main parameters investigated in this research are the diameter to thickness ratio (D/t), the grade of concrete, the volume of fly ash in concrete mix and the length to tube

diameter ratio ($^{L}/_{D}$). The $^{D}/_{t}$ ratio ranged from 25 to 39 where different outer diameter and steel thickness were used. In addition, design strength of 30MPa and 40MPa were used for the concrete infill of CFST specimens. Moreover, the fly ash volume percentage in the concrete mixes was 0% (control mix), 15%, 20% or 25%. It should be noted that a fixed loading rate of 5.3KN/s was applied on the samples. Besides, only vertical dial gages were placed around the specimens to measure axial deformation, while the lateral expansions are ignored in this paper. The experimental axial capacities of the specimens were compared to calculated ones using equations proposed by ACI and Mander, et al. [41]. It was noticed that Mander, et al equation provides more conservative design capacity than the one provided by ACI equation. Additionally, the CFST samples with 50mm diameter failed by Euler buckling while the specimens with 75mm and 100mm failed due to triggering of local buckling. It was observed that as the concrete strength increases the confinement effect of the concrete infill decreases. Also, the energy absorbing capacity at a given deformation decreases with the increase of fly ash up to 20%, but at 25% fly ash it increases again. Moreover, the slope of the load verses deformation curves of the experimental data is found to be less than that of the analytical model.

Ellobody, et al. [42] investigated the behavior and design of axially loaded circular CFST stub columns through extensive computational studies performed using a Nonlinear Finite Element code ABAQUS. The model's results were compared with the results of the tests conducted by Giakoumelis and Lam [43] and Sakino, et al. [38] in order to verify it. The main goal of this research is to perform a parametric studies on the circular CFST stub columns using the output data of the develop FE model. The data of the existing experimental studies used in this paper covered a wide range of concrete cube strengths ranging from 30MPa to 110MPa. Also, the column diameter to steel thickness ratio ($^{D}/_{t}$) ranged from 15 to 80. Due to symmetry,

only quarter of the column is modeled in ABAQUS given the boundary conditions. The material property of steel was simulated either by two multi-linear stress–strain curves or by tri-linear stress–strain curves depending on the steel tube thickness. In addition, the confined concrete compressive strength and the corresponding confined strain was simulated by the equations proposed by Mander, et al. [41]. It should be noted that the yielding segment in the confined stress–strain curve for concrete is modeled using the Drucker–Prager yield criterion model available in the ABAQUS material library. Moreover, the contact between the concrete and the steel tube is simulated by interface elements that consist of two matching contact faces while maintaining the friction between the two surfaces. The CFST column strengths predicted by the computational analysis were compared to the design strengths calculated using the European, Australian and American codes specifications. It was found out that for the axially loaded CFST circular columns, the Australian and the American Specifications are able to produce reliable limit state design when calibrated with the resistance factor $\varphi = 0.85$. Also, the parametric study showed that the design strengths given by the European Code are generally unconservative, while those of the Australian Standards and American Specifications are conservative.

Liang and Fragomeni [44] proposed an accurate generic fiber element model for normal and high strength concrete confined by either high strength or normal circular steel tubes. Recent experimental investigations on circular CFST columns conducted by Sakino, et al. [38], Hu, et al. [26] and Giakoumelis and Lam [43] were used to verify the model developed in this study. A new design formula is proposed for circular CFST columns that takes into consideration the concrete confinement effects. The authors found out that the confining pressure models for concrete in circular CFST columns proposed by Ellobody, et al. [42] might not be applicable to high strength circular CFST columns. Thus, an enhanced model for confining pressure is

proposed based on the research done by Tang, et al. [45] and Hu, et al. [26] as well as existing experimental results. In addition, the stress-strain curve for the steel is expressed by the equation proposed by Liang [46] which gives special consideration to high strength steels. The extensive parametric study performed in this paper examined the effect of concrete compressive strengths ranging from 25MPa to 90MPa, the column diameter to steel thickness ratio ($^{D}/_{t}$) ranging from 16 to 101 and the steel yield strengths that ranging from 260MPa to 840MPa. It was pointed out that existing confining pressure models which were developed based on normal strength materials overestimates the lateral confining pressures in high strength circular CFST columns. Furthermore, the axial load capacity and the performance of circular CFST columns significantly increase proportionally with increasing the steel yield strength. The design formula proposed in this study showed good estimation of the ultimate axial loads of circular CFST columns, thus it can be used in designing these sections.

Kuranovas, et al [47] presented a detailed analysis of existing experimental data of more than 1300 specimens of CFST. This huge number of specimens covered varies types of CFSTs such as solid and hollow concrete core with rectangular and circular cross sectional areas with concentric and eccentric axial loads applied with preloading and sustained load. The capacity of the tested CFST samples were calculated using the approach suggested by EC4 in order to find the accuracy of the predicted values compared with the actual ones. The authors recommended the Unified theory [48] as one of the methods for determining load bearing capacity of CFST column studs. This theory states that the CFST is considered as a unified body with a behavior that changes with the change of geometrical parameters of element, mechanical properties of materials, stresses states and types of cross sectional areas. Thus, a single design formula can be used for predicting the load bearing capacity of CFST members. It was concluded that the design

requirement of CFST suggested in EC4 is a safe approach for determining the strength for all types of circular CFST column studs given that the concrete infill strength is less than 100MPa. Also, the Unified theory proved to be useful as a new research method and design approach for CFST elements which requires extensive additional research.

Lan and Yiyan [49] studied the behavior of carbon-FRP and glass-FRP confined circular CFSTs through an analytical and experimental studies. The confining steel thickness, the concrete infill compressive strength, the type and the thickness of wrapping were the main parameters considered in their experimental program. The analytical part included the proposal of a set of equations that predict the axial capacity of a confined CFST with carbon wrapping. A total of eleven samples were prepared and tested in this study. The specimens were prepared such that the outer diameter was around 128mm and the height was 400mm. The steel thickness ranged from 3mm to 5mm. three concrete compressive strengths were used 40MPa, 50MPa and 60MPa. Moreover, single, double and triple layers of wraps were investigated in testing. The proposed equation considered the additional confining effects of the carbon-FRP on the concrete infill compressive strength. Also, the effects of wraps on delaying the outwards buckling of the steel tube were considered. Note that few assumption related to the section's behavior were made, for instance the carbon-FRP wrapping lacks the ability to resist axial load and its only limited to hoop stress. It was concluded that increasing the number of FRP wrapping layers around the CFST specimens not only improves their axial capacity but also enhances their ductility. In addition, it was found that the proposed set of equations provided a good estimate to the tested samples bearing capacity, thus its use for further prediction is feasible.

Hu, et al. [50] analyzed the behavior of glass-FRP confined circular CFT through an experimental study. Two main parameters were considered in the experimental program which;

the diameter-to-thickness ratio of steel tube and the hoop stiffness of the glass-FRP wrap. This research was part of a larger study undertaken at the Hong Kong Polytechnic University to fully grasp the structural behavior of such composite elements. A total of twelve samples were prepared and tested in this study. All the specimens were prepared such that the outer diameter was around 200mm and the height was 400mm. hence the variation of D/t ratio resulted from the change in the steel tube thickness which ranged from 1mm to 2mm. the thickness of the used glass-FRP wrap is 0.17mm. The stiffness of the wrapping was increased via increasing the number of wrapping layers. It should be mentioned that the steel tube was prepared by welding a thin steel plate and the glass-FRP wrapping was prepared using the wet lay-up method while fibers were only in the hoop direction. The results were analyzed and a simplified equation was proposed to calculate the confining effect of the glass-FRP wrapping on the concrete in addition to the steel's. This confining pressure could be used to calculate the axial capacity of the CCFST element. It was observed that the local buckling of the steel tube in a CFST element can be delayed using the glass-FRP wrapping. Also, as the steel thickness reduces in the CCFST, the enhancement effects due to wrapping increases. In addition, the dominant failure mode in the axially loaded CCFST was the explosive rupture of FRP in the mid height region.

Chapter 2: Experimental program

2.1 Test specimen preparation

A total of one hundred and three specimens were tested throughout this research. The tested samples were concrete cubes, concrete cylinders, hollow circular steel tubes, standard steel coupons, concrete filled steel tubes (CFST) and confined concrete filled steel tubes (CCFST). Figure 5 shows a chart of this study's specimens which are classified based on the parameters loading rate (R), concrete infill compressive strength f'_c and the Diameter-to-thickness ratio (D/t).

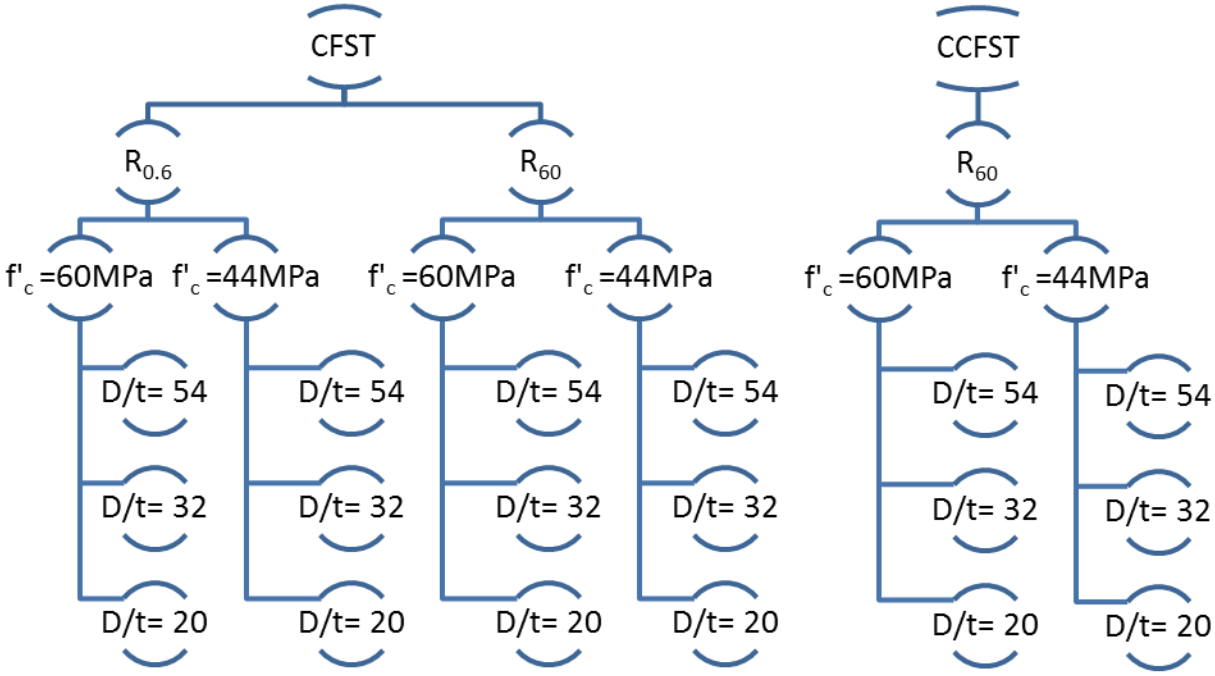

Figure 5: testing program matrix

2.1.1 Hollow steel tubes

Three long steel tubes of six meter long each were purchased and moved to the university lab. Then, hollow steel tubes samples were prepared using the manufacturing machine to insure the consistency of the samples lengths and to maintain the orthogonality between the circular surface and cylinder access. Table 2 shows the properties of the hollow steel tube specimens.

Table 2: Geometric properties of hollow steel tube test specimens

No.	Specimen	D x t x L (mm)	A_s (mm^2)	loading rate (kN/s)
1	tube $t_{3.1}$ R_{60} -1	167 x 3.1 x 175	805.7	60
2	tube $t_{5.6}$ R_{60} -1	114 x 5.6 x 250	978.2	60
3	tube $t_{5.6}$ R_{60} -2	114 x 5.6 x 250	978.2	60
4	tube $t_{3.6}$ R_{60} -1	114 x 3.6 x 250	634.5	60
5	tube $t_{3.6}$ R_{60} -2	114 x 3.6 x 250	634.5	60
6	tube $t_{3.1}$ $R_{0.6}$ -1	167 x 3.1 x 175	805.7	0.6
7	tube $t_{5.6}$ $R_{0.6}$ -1	114 x 5.6 x 250	978.2	0.6
8	tube $t_{5.6}$ $R_{0.6}$ -2	114 x 5.6 x 250	978.2	0.6
9	tube $t_{3.6}$ $R_{0.6}$ -1	114 x 3.6 x 250	634.5	0.6
10	tube $t_{3.6}$ $R_{0.6}$ -2	114 x 3.6 x 250	634.5	0.6

For each of the hollow steel tubes, two unidirectional strain gages were used to capture the strains in the mid height region of the sample. The two strain gages were glued on the outer side of the tube. One of the strains a gage is fixed horizontally and the other was mounted vertically with a small gap between the gages. Figure 6 show a sketch of the geometry of the hollow steel tube and the location of the strain gages with their orientation as well as a photo of a sample.

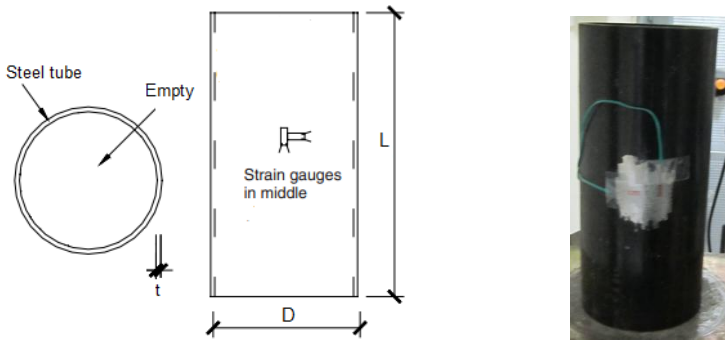

Figure 6: hollow steel tube sample

It should be noted that the type of tubes used in this study are welded steel, not seamless tubes. In other words, the steel was cast as a plate then bent and welded into a tube rather than being cast in a circular tube mold.

2.1.2 Concrete filled steel tubes

Thirty three concrete filled steel tube specimens with different sizes were tested in this study. The prepared hollow steel tubes mentioned in the previous section were used to make the CFST samples. The inner surfaces of the empty tubes were roughened slightly with a grinder in order to increase the bond between the concrete and the steel. Then, the hollow tubes were transported to the concrete supplier's quality control lab -DAFCO- to be filled with concrete. Sixteen samples were filled with normal strength concrete and the remaining seventeen were filled with high strength concrete. Table 3 shows the properties of the CFST specimens.

The inner surfaces of the hollow tubes were moistured to prevent the steel surface from reducing the concrete mix's water content. As shown in Figure 7 the concrete was filled in three or four layers depending on the sample's size. Afterwards, the concrete layers were compacted

Table 3: Properties of concrete filled steel tube test specimens

ID	D x t x L (mm)	A_s (mm^2)	A_c (mm^2)	f'_c (MPa)	D/t	loading rate (kN/s)
$R_{60}\,f_{60}\,D_{167}\,t_{3.1}$ - 1	167 x 3.1 x 350	806	20308	60	54	60
$R_{60}\,f_{60}\,D_{167}\,t_{3.1}$ - 2	167 x 3.1 x 350	806	20308	60	54	60
$R_{60}\,f_{60}\,D_{167}\,t_{3.1}$ - 3	167 x 3.1 x 350	806	20308	60	54	60
$R_{60}\,f_{60}\,D_{114}\,t_{5.6}$ - 1	114 x 5.6 x 250	978	8300	60	20	60
$R_{60}\,f_{60}\,D_{114}\,t_{5.6}$ - 2	114 x 5.6 x 250	978	8300	60	20	60
$R_{60}\,f_{60}\,D_{114}\,t_{5.6}$ - 3	114 x 5.6 x 250	978	8300	60	20	60
$R_{60}\,f_{44}\,D_{114}\,t_{5.6}$ - 1	114 x 5.6 x 250	978	8300	44	20	60
$R_{60}\,f_{44}\,D_{114}\,t_{5.6}$ - 2	114 x 5.6 x 250	978	8300	44	20	60
$R_{60}\,f_{44}\,D_{114}\,t_{5.6}$ - 3	114 x 5.6 x 250	978	8300	44	20	60
$R_{60}\,f_{44}\,D_{167}\,t_{3.1}$ - 1	167 x 3.1 x 350	806	20308	44	54	60
$R_{60}\,f_{44}\,D_{167}\,t_{3.1}$ - 2	167 x 3.1 x 350	806	20308	44	54	60
$R_{60}\,f_{60}\,D_{114}\,t_{3.6}$ - 1	114 x 3.6 x 250	635	8958	60	32	60
$R_{60}\,f_{60}\,D_{114}\,t_{3.6}$ - 2	114 x 3.6 x 250	635	8958	60	32	60
$R_{60}\,f_{60}\,D_{114}\,t_{3.6}$ - 3	114 x 3.6 x 250	635	8958	60	32	60
$R_{60}\,f_{44}\,D_{114}\,t_{3.6}$ - 1	114 x 3.6 x 250	635	8958	44	32	60
$R_{60}\,f_{44}\,D_{114}\,t_{3.6}$ - 2	114 x 3.6 x 250	635	8958	44	32	60
$R_{60}\,f_{44}\,D_{114}\,t_{3.6}$ - 3	114 x 3.6 x 250	635	8958	44	32	60
$R_{0.6}\,f_{60}\,D_{167}\,t_{3.1}$ - 4	167 x 3.1 x 350	806	20308	60	54	0.6
$R_{0.6}\,f_{60}\,D_{167}\,t_{3.1}$ - 5	167 x 3.1 x 350	806	20308	60	54	0.6
$R_{0.6}\,f_{60}\,D_{114}\,t_{5.6}$- 4	114 x 5.6 x 250	978	8300	60	20	0.6
$R_{0.6}\,f_{60}\,D_{114}\,t_{5.6}$- 5	114 x 5.6 x 250	978	8300	60	20	0.6
$R_{0.6}\,f_{60}\,D_{114}\,t_{5.6}$- 6	114 x 5.6 x 250	978	8300	60	20	0.6
$R_{0.6}\,f_{44}\,D_{114}\,t_{5.6}$- 4	114 x 5.6 x 250	978	8300	44	20	0.6
$R_{0.6}\,f_{44}\,D_{114}\,t_{5.6}$- 5	114 x 5.6 x 250	978	8300	44	20	0.6
$R_{0.6}\,f_{44}\,D_{114}\,t_{5.6}$- 6	114 x 5.6 x 250	978	8300	44	20	0.6
$R_{0.6}\,f_{44}\,D_{167}\,t_{3.1}$ - 4	167 x 3.1 x 350	806	20308	44	54	0.6
$R_{0.6}\,f_{44}\,D_{167}\,t_{3.1}$ - 5	167 x 3.1 x 350	806	20308	44	54	0.6
$R_{0.6}\,f_{60}\,D_{114}\,t_{3.6}$ - 4	114 x 3.6 x 250	635	8958	60	32	0.6
$R_{0.6}\,f_{60}\,D_{114}\,t_{3.6}$ - 5	114 x 3.6 x 250	635	8958	60	32	0.6
$R_{0.6}\,f_{60}\,D_{114}\,t_{3.6}$ - 6	114 x 3.6 x 250	635	8958	60	32	0.6
$R_{0.6}\,f_{44}\,D_{114}\,t_{3.6}$ - 4	114 x 3.6 x 250	635	8958	44	32	0.6
$R_{0.6}\,f_{44}\,D_{114}\,t_{3.6}$ - 5	114 x 3.6 x 250	635	8958	44	32	0.6
$R_{0.6}\,f_{44}\,D_{114}\,t_{3.6}$ - 6	114 x 3.6 x 250	635	8958	44	32	0.6

manually with a tamping rod. Each concrete layer was prepared with at least twenty five strokes. Then the upper surface was leveled and covered with plastic sheets for 24hours. Then, the samples were brought back to the university lab to be further cured in the water tank for 28 days. The same process was repeated for the second batch of high strength concrete the next day. The proportions of the concrete mixes utilized in this study are presented in Table 4.

Figure 7: the casting of CFST

Table 4: Concrete mix proportions

Concrete type	$\frac{Water}{Cement}$	Mix proportions (divided by weight of cement)				
		Cement	Coarse Aggregates	Fine Aggregates	Water	Plasticizer
Normal strength concrete	0.62	1	3.4	2.9	0.62	-
High strength concrete	0.41	1	3.2	2	0.41	1.1%

After being soaked in the water tank for 28 days for curing, the specimens were taken out to be dried at the room temperature for one day. Due to the inevitable water loss of concrete mix, drying shrinkage took place. Hence, the concrete top and bottom surfaces were less than the steels'. Thus, the steel was grinded and leveled with the concrete surface. Note that the height of

steel layer to be grinded did not exceed 4mm where the maximum shrinkage took place. Also, the CFST with diameter of 167mm experienced larger shrinkage than the smaller sized CFST due to the difference in concrete volume.

Just like the empty steel tubes, two unidirectional strain gages were used to capture the strains in the mid height region of the CFST sample. The properties of the used strain gages are discussed later in this chapter. Similar to the hollow steel tube samples, one of the strain gages is fixed horizontally and the other was mounted vertically with a small gap between the gages. Figure 8 shows a sketch of the geometrical properties of the CFST and the location of the strain gages with their orientation, with comparison to a real one.

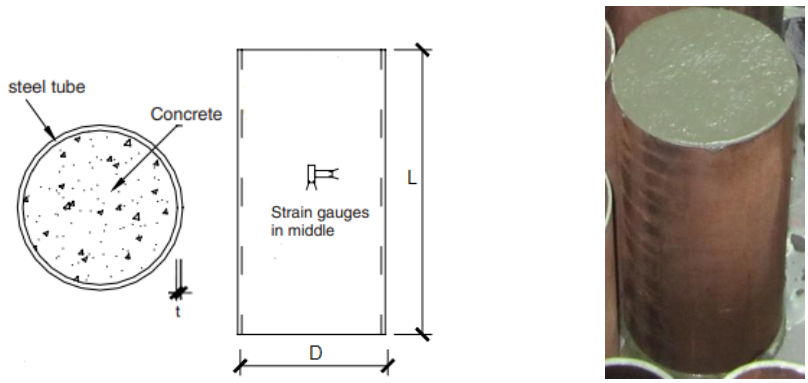

Figure 8: Concrete filled steel tube sample

2.1.3 Confined concrete filled steel tubes

Eighteen confined concrete filled steel tube specimens with different geometric properties were tested in this study. The CCFST samples were cast and cured with the CFST elements mentioned previously. In other words, the CCFST and the CFST specimens experienced the same surrounding conditions in order to minimize the variations due to preparation on the behavior of both elements for future comparisons. Nine samples were filled with normal strength

concrete and the other nine filled with high strength concrete. Only high loading rate was applied on the CCFST specimens. Table 5 shows the properties of the CCFST specimens. The GFRP wraps covered the specimens' entire height.

Table 5: Properties of confined concrete filled steel tube test specimens

ID	D x t x L (mm)	A_s (mm^2)	A_c (mm^2)	f_c' (MPa)	D/t	loading rate (kN/s)
$C_g\,R_{60}\,f_{60}\,D_{167}\,t_{3.1}$ - 1	167 x 3.1 x 350	806	20308	60	54	60
$C_g\,R_{60}\,f_{60}\,D_{167}\,t_{3.1}$ - 2	167 x 3.1 x 350	806	20308	60	54	60
$C_g\,R_{60}\,f_{60}\,D_{167}\,t_{3.1}$ - 3	167 x 3.1 x 350	806	20308	60	54	60
$C_g\,R_{60}\,f_{60}\,D_{114}\,t_{5.6}$ - 1	114 x 5.6 x 250	978	8300	60	20	60
$C_g\,R_{60}\,f_{60}\,D_{114}\,t_{5.6}$ - 2	114 x 5.6 x 250	978	8300	60	20	60
$C_g\,R_{60}\,f_{60}\,D_{114}\,t_{5.6}$ - 3	114 x 5.6 x 250	978	8300	60	20	60
$C_g\,R_{60}\,f_{44}\,D_{114}\,t_{5.6}$ - 1	114 x 5.6 x 250	978	8300	44	20	60
$C_g\,R_{60}\,f_{44}\,D_{114}\,t_{5.6}$ - 2	114 x 5.6 x 250	978	8300	44	20	60
$C_g\,R_{60}\,f_{44}\,D_{114}\,t_{5.6}$ - 3	114 x 5.6 x 250	978	8300	44	20	60
$C_g\,R_{60}\,f_{44}\,D_{167}\,t_{3.1}$ - 1	167 x 3.1 x 350	806	20308	44	54	60
$C_g\,R_{60}\,f_{44}\,D_{167}\,t_{3.1}$ - 2	167 x 3.1 x 350	806	20308	44	54	60
$C_g\,R_{60}\,f_{44}\,D_{167}\,t_{3.1}$ - 3	167 x 3.1 x 350	806	20308	44	54	60
$C_g\,R_{60}\,f_{60}\,D_{114}\,t_{3.6}$ - 1	114 x 3.6 x 250	635	8958	60	32	60
$C_g\,R_{60}\,f_{60}\,D_{114}\,t_{3.6}$ - 2	114 x 3.6 x 250	635	8958	60	32	60
$C_g\,R_{60}\,f_{60}\,D_{114}\,t_{3.6}$ - 3	114 x 3.6 x 250	635	8958	60	32	60
$C_g\,R_{60}\,f_{44}\,D_{114}\,t_{3.6}$ - 1	114 x 3.6 x 250	635	8958	44	32	60
$C_g\,R_{60}\,f_{44}\,D_{114}\,t_{3.6}$ - 2	114 x 3.6 x 250	635	8958	44	32	60
$C_g\,R_{60}\,f_{44}\,D_{114}\,t_{3.6}$ - 3	114 x 3.6 x 250	635	8958	44	32	60

In order to enhance the bond between the specimens and the glass-FRP wraps a layer of saturant is applied on the curved sides of the samples. The saturant is prepared by mixing its two compounds. 24 hours is the required time for the applied saturant to get dried.

The wrapping sheets used for additional confinement of the specimens are made of glass-FRP. The geometric and physical properties of this sheet are provided in Table 6. There are two

methods for applying the wrapping sheets to the specimens, the dry application and the submerged one. The dry application is the one used in this study since the sheets need to be applied along the samples circumference. In the dry method, the epoxy is applied on the surface of the specimen and on the side of the wrapping sheet that will be in contact with. After attaching the glass-FRP sheet on the specimen, thin layer of epoxy is coated on the other side of the sheet. In other words, the wrapping sheet should be sandwiched between two layers of epoxy, one of these layers is between the glass-FRP and the steel tube, and the other will be just on the outer surface of the CCFST specimen.

Table 6: glass-FRP wraps properties

Property	Grade
Type of fiber	E-Glass 90/10
Fiber weight (g/m^2)	980
Fiber density (g/m^2)	2.78
Design thickness (fiber weight/density) (mm)	0.352
Tensile strength – fiber (MPa)	3400
Elastic modulus (GPa)	> 72
Elongation at rupture (%)	> 4

The used glass wrapping sheets are unidirectional, thus its fibers are arranged such that they resist the loads in one direction only. In order to observe the confinement effect on the strength of the specimens, the fibers of the glass-FRP sheets should be aligned along their circumference. The fabricated glass-FRP sheets are arranged such that any attempt to cut it along its fiber line will cause the disintegration of the contained fibers. As a result, the full width of the wrapping sheet should be used in the application stage as shown in Figure 9. After the hardening of the epoxy, the excess wrapping sheet is grinded out.

Figure 9: Additional wrapping for CCFST samples

Just like the saturant, the epoxy is prepared by mixing its two compounds. It should be noted that the viscosity of the saturant is very low compared to the epoxys, thus its application via painting brush is feasible. However, the epoxy is too thick and had to be applied by hand while wearing heavy duty latex gloves.

Similar to the CFST samples, a horizontal and vertical unidirectional strain gages were mounted on the outer surface of the steel tube in the CCFST specimen. Then, a hater proof tape was used to isolate the strain gages from the liquid epoxy layer. Figure 10 shows a sketch of the geometry of the CCFST and the location of the strain gages with their orientation.

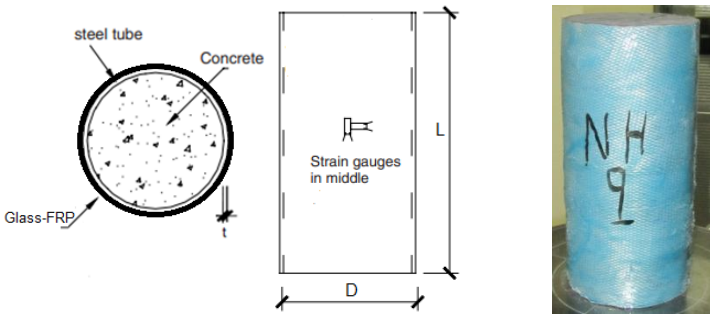

Figure 10: Confined concrete filled steel tube sample

2.2 Control specimen preparation

It is well known that these types of tests are performed to obtain the basic materials' characteristics affecting the behavior of the tested samples. In this research, the main materials are steel and concrete.

2.2.1 Steel coupon test

Coupon samples from each of the three purchased steel tubes are essential for two main reasons. Firstly, obtaining the steel properties such as the yield and fracture strengths for further analysis and calculation. Secondly, confirming that the three steel tubes have similar properties, otherwise new parameters should be considered in the comparison among the specimens.

The required dimensions of the coupon specimens depend on many factors such as the available testing equipment. One of the proposed measurements for a steel coupon sample is shown in Figure 11. The specimens for this test are prepared from the leftover of the steel tubes. The tubes were grinded, opened and flattened to return being a steel plate. Then the samples were extracted from this plate in the manufacturing lab.

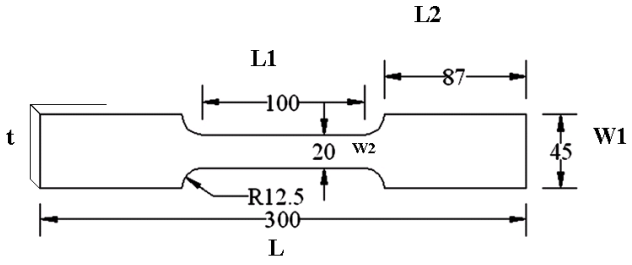

Figure 11: standard measurements of the coupon samples

The samples were grouped and tested at three different loading rates. It should be noted that the samples' ends were slightly larger than the gripping heads of the test machine. However,

slippage of the specimens was prevented as monitored during the loading periods. The actual dimensions of the coupon samples were manually measured using a vernier and are listed in Table 7.

Table 7: dimensions of the steel coupon test specimens

Specimen	W_2 (mm)	W_1 (mm)	t (mm)	L_1 (mm)	L_2 (mm)
$t_{3.6}$ -1	20.11	44.87	3.58	100.67	87.12
$t_{3.6}$ -2	20.21	45.12	3.46	100.61	86.82
$t_{3.6}$ -3	20.24	45.31	3.6	100.53	87.08
$t_{3.6}$ -4	20.43	45.05	3.61	101.02	87.63
$t_{3.6}$ -5	20.2	45.83	3.6	100.86	86.94
$t_{3.6}$ -6	20.34	45.66	3.6	100.44	86.88
$t_{5.6}$ -1	20.3	44.92	5.57	101.03	87.44
$t_{5.6}$ -2	20.25	45.33	5.64	100.14	87.34
$t_{5.6}$ -3	20.38	45.00	5.64	100.11	86.58
$t_{5.6}$ -4	20.25	45.31	5.62	100.84	87.18
$t_{5.6}$ -5	20.17	44.78	5.62	101.81	87.63
$t_{5.6}$ -6	20.45	45.45	5.62	101.73	87.15
$t_{3.1}$ -1	20.21	45.22	3.08	100.75	86.83
$t_{3.1}$ -2	20.26	45.13	2.98	100.57	87.34
$t_{3.1}$ -3	20.27	44.90	3.00	100.14	87.08
$t_{3.1}$ -4	20.35	45.36	3.07	100.24	87.11
$t_{3.1}$ -5	20.19	45.24	3.13	101.28	87.27
$t_{3.1}$ -6	20.39	45.04	3.07	100.55	86.94
$t_{3.1}$ -7	20.25	45.21	3.07	100.87	86.88
$t_{3.1}$ -8	20.20	44.97	3.09	100.51	87.44

2.2.2 Concrete compressive strength

Concrete cubes were prepared from the same batches of concrete that the steel tubes were filled from. Of course, the specimens were cured via submergence in water tank. Two standard sizes of concrete specimens were prepared and tested, the 100mm cubes and the 150mm cubes.

The four cubes were tested statically after seven days to confirm that the ordered concrete strengths are met. The ten large concrete cubes were tested statically after 28 days of curing. The characteristics of the tested cubes are presented in Table 8.

Table 8: concrete cubes properties

Sample	Dimensions (mm)	Mass of Specimen (kg)
cube-H1	150 x150 x 150	8.30
cube-H2	150 x150 x 150	8.30
cube-H3	150 x150 x 150	8.30
cube-H4	150 x150 x 150	8.18
cube-H5	150 x150 x 150	8.50
cube-L1	150 x150 x 150	8.45
cube-L2	150 x150 x 150	8.30
cube-L3	150 x150 x 150	8.30
cube-L4	150 x150 x 150	8.30
cube-L5	150 x150 x 150	8.34

Likewise, the concrete cylinders were not only cast from the same two batches of concrete as the CFST samples but also were submerged in water for the same duration. The concrete cylinders were cast using standard mold size of a 100mm diameter and 200mm height. They were subjected to the same loading rates as CFST and CCFST specimens as presented in Table 9. Additionally, one from each of the four concrete cylinders groups were selected to measure its deformation via strain gages. Each sample had two unidirectional strain gages fixed on its mid height region of the outer surface. Grinding was performed instead of using capping to eliminate the irregularities of the upper surface of the cylinder.

Table 9: Concrete cylinders properties

Sample	Dimensions (mm)	Mass of Specimen (kg)	Loading rate kN/s
$R_{60}\,f_{60}$ - 1	100 x 200	3.86	60
$R_{60}\,f_{60}$ - 2	100 x 200	3.96	60
$R_{60}\,f_{60}$ - 3	100 x 200	3.80	60
$R_{60}\,f_{44}$ - 1	100 x 200	3.86	60
$R_{60}\,f_{44}$ - 2	100 x 200	3.86	60
$R_{60}\,f_{44}$ - 3	100 x 200	3.93	60
$R_{0.6}\,f_{60}$ - 1	100 x 200	3.86	0.6
$R_{0.6}\,f_{60}$ - 2	100 x 200	3.86	0.6
$R_{0.6}\,f_{60}$ - 3	100 x 200	3.78	0.6
$R_{0.6}\,f_{44}$ - 1	100 x 200	3.88	0.6
$R_{0.6}\,f_{44}$ - 2	100 x 200	3.86	0.6
$R_{0.6}\,f_{44}$ - 3	100 x 200	3.81	0.6

2.3 Testing machines and measuring devices

Two universal testing machines were used throughout the testing program. One of them is used for the testing of the CFST, CCFST, hollow steel tubes and concrete specimens, while the other is used for the coupon steel tests. For the measurements, the universal machine's built in gages and the externally attached strain gages were used.

2.3.1 Universal testing machines

The MTS Servo Hydraulic Compression Model YAW4306 is the universal testing machine that was used in the proposed compression tests for all the specimens except the coupon steel samples. The samples sizes and capacities were designed such that none of the testing machines' limitations are exceeded, namely the specimen height and the compression capacity.

Note that the data used for plotting the load-deformation graphs shown in later chapters are obtained from the machines' built-in gages.

For the steel coupon test, the INSTRON Floor Standing 5582 universal testing machine was used. The specimens' measurements were prepared according to the standards based on the machines' capacities. The specimens' ends were somewhat larger than the gripping heads of the test machine. However, no slippage of the samples occurred during any of the tests. Just like the YAW4306, the INSTRON 5582 provided the data for the stress-strain diagrams based on the specimens' measurements. Figure 12 shows the experimental set up of the two universal testing machines.

Figure 12: The used universal machines: YAW4306 (Left) [51] and INSTRON 5582 (Right) [52]

Table 10 displays some of the mechanical characteristics and testing limitations of the two universal machines used.

Table 10: Universal machines specifications

Model	Load capacity	Max. Speed	Min. Speed	Frame dimensions (L x W x H) (mm)	Max. specimen height (mm)
YAW4306	3000 (kN)	60 (kN/s)	0.6 (kN/s)	720 x 720 x 1790	405
INSTRON 5582	100 (kN)	500 (mm/min)	0.001 (mm/min)	1300 x 756 x 2092	575

2.3.2 Strain gages

Unidirectional strain gages are used for measurements during the testing. Two unidirectional types of gages were utilized: the 5mm and the 10mm. the first one was used to measure the strains of steel surfaces such as the CFST, steel tube and CCFST, while the second was used to measure the strains of concrete surfaces mainly the concrete cylinders. The characteristics of these two types are presented in Table 11.

Table 11: strain gages data

Strain Gage Pattern	Type	Nominal Resistance (Ω)	Approximate Gage Factor	Dimension (mm)			
				Grid		Base	
				Length	Width	Length	Width
	N11-FA-5-120-11	120	2.1	5	1.8	9.5	3.5
	N11-FA-10-120-11	120	2.1	10	2.2	15	5

For the concrete specimens, the strain gages were simply glued to the targeted surface via super glue only. However, in the rest of the specimens the exposed parts of the gage's wire needed to be isolated from the conducting surface of steel. This was done using a masking tape which was placed under and above that exposed part of the wire. Note that in the case of the

CCFST the strain gage was fixed on the steel surface then the glass FRP sheet was wrapped above it. Thus, a water proofing tape was used to prevent the moisture of the epoxy from reaching the gages. The strain gages were always fixed in the mid height region of the samples and each sample had two gages, horizontally and vertically. Figure 13 shows some photos of the strain gauges used in the proposed experimental testing.

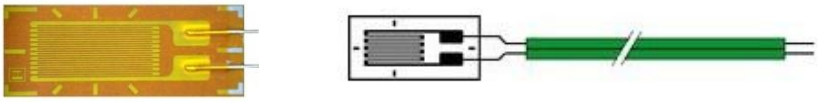

Figure 13: Unidirectional strain gage [53]

Chapter 3: Results and discussion

3.1 Concrete material tests:

3.1.1 Cube test:

Concrete cubes were cast from the same batches used to fill the CFST steel tubes. After 28 days of curing in water, ten standard size concrete cubes (150mm x 150mm x 150mm) were subjected to standard compressive test to determine the two concrete batches' compressive strengths, as shown in Table 12.

Table 12: concrete cubes compressive strengths after 28 days

f_c'	Sample Code	Mass of Specimen	Load	Stress	Avg. Mass (kg)	Avg. Peak Load (kN)	Avg. Max Stress (MPa)
		kg	kN	MPa			
High strength concrete cubes	cube-H1	8.3	4677	21	8.32	1568	70
	cube-H2	8.3	1571	70			
	cube-H3	8.3	1573	70			
	cube-H4	8.18	1536	68			
	cube-H5	8.5	1591	71			
Normal strength concrete cubes	cube-L1	8.45	1253	56	8.34	1197	53
	cube-L2	8.3	1179	52			
	cube-L3	8.3	1195	53			
	cube-L4	8.3	1073	48			
	cube-L5	8.34	1283	57			

As shown, the cubes are divided into two sets, one from high strength batch and the other is from the normal strength batch. It can be noted that the test results for specimen cube-H1 varies from the others. This variation was a result of the stress concentration that took place while testing because of the unleveled cube sides that was used by mistake.

Figure 14 shows the failure mode of one of the concrete cubes when tested after 28 days. The double coned failure was the dominant failure mode among all the cubes. This failure mode indicated a good distribution of particles and ingredients in the concrete mix. In addition, it shows an adequate bond between the cement paste and the aggregate. Also, it points out that the applied load is almost pure axial loading with minimal eccentricity if any.

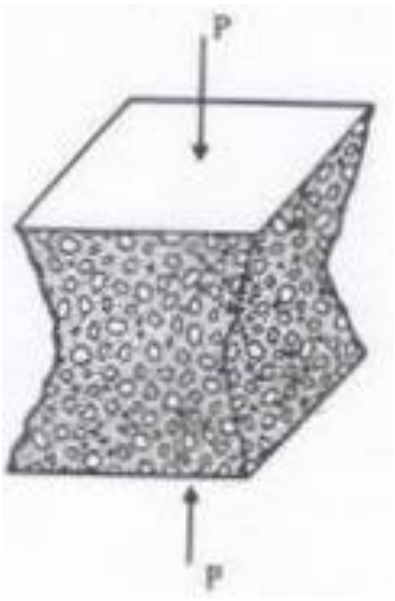

(a) Double cone failure [54] (b) Tested cube

Figure 14: failure mode of concrete cube

3.1.2 Cylinder test:

Just like the concrete cubes, the 12 concrete cylinders were cast from the same batches used to fill the CFST steel tubes, 6 form each batch. The concrete cylinders and the CFSTs were tested at the same time. The cylinders were subjected to high and normal loading rates similar to the ones applied to the CFSTs. Table 13 shows the summary of the results, where R_{60} and $R_{0.6}$ refers to the loading rate of 60kN/s and 0.6kN/s, respectively. Also, f_{60} and f_{44} refers to the concrete's compressive strength of 60 MPa and 44 MPa, respectively.

Table 13: concrete cylinders compressive strengths

ID	Ultimate Load	Ultimate Stress	AVG. Ultimate Load	AVG. Ultimate Stress
$R_{60}\,f_{60}$ - 1	512	65	504	64
$R_{60}\,f_{60}$ - 2	506	64		
$R_{60}\,f_{60}$ - 3	493	63		
$R_{60}\,f_{44}$ - 1	364	46	365	46
$R_{60}\,f_{44}$ - 2	370	47		
$R_{60}\,f_{44}$ - 3	359	46		
$R_{0.6}\,f_{60}$ - 1	479	61	475	60
$R_{0.6}\,f_{60}$ - 2	452	58		
$R_{0.6}\,f_{60}$ - 3	493	63		
$R_{0.6}\,f_{44}$ - 1	338	43	344	44
$R_{0.6}\,f_{44}$ - 2	341	44		
$R_{0.6}\,f_{44}$ - 3	352	45		

The concrete cylinders subjected to high loading rate exhibited explosive failure regardless of their compressive strength. However, the specimens subjected to low rate of loading experienced shear failure unlike the concrete cube as shown in Figure 15.

(a) Tested concrete cylinder (b) Shear failure

Figure 15: failure mode of concrete cylinder under loading rate of 0.6kN/s

Figure 16 shows the load-displacement diagrams of concrete cylinder with compressive strengths of 60MPa and 44MPa and subjected to loading rate of 60kN/s. Clearly, the stiffness of high compressive strength concrete is greater than the normal compressive strength concrete. It is

noted that the absence of the nonlinear region in the two curves is due to the brittle nature of concrete in addition to the high loading rate.

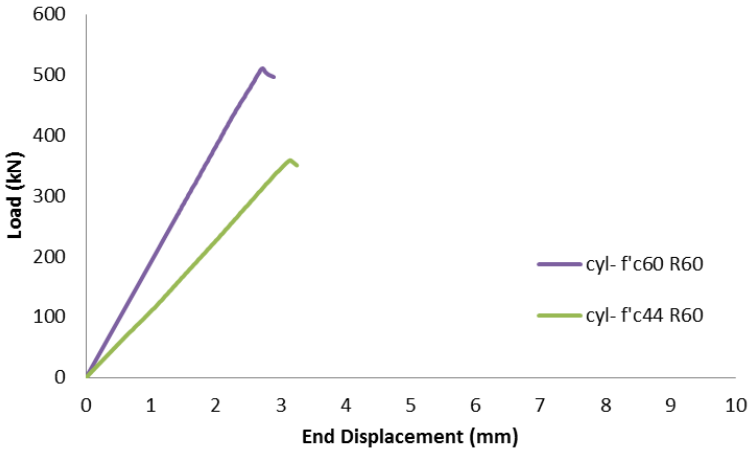

Figure 16: Load-End shorting diagram of concrete cylinder under loading rate of 60kN/s

Figure 17 shows the load-displacement diagrams of concrete cylinder with compressive strengths of 60MPa and 44MPa and subjected to loading rate of 0.6kN/s. Unlike the high loading rate case the stiffness of high compressive strength concrete is slightly larger than the normal compressive strength concrete. Moreover, the nonlinear region in the two curves is very small due to the brittle nature of concrete, but it is greater than the high loading rate's nonlinear region.

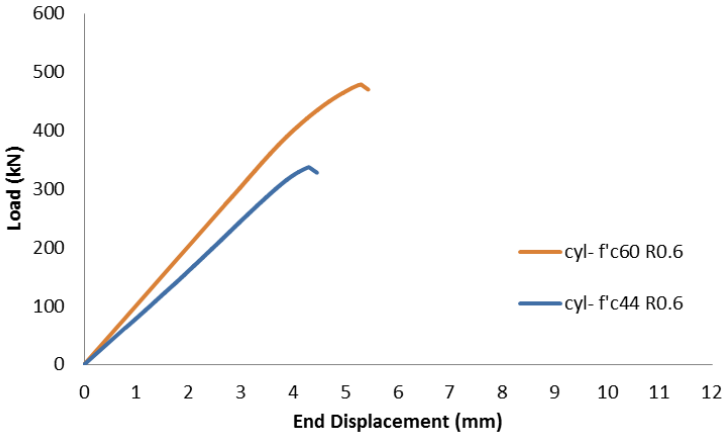

Figure 17: Load-End displacement diagram of concrete cylinder under loading rate of 0.6kN/s

The stress-end shortening diagrams of all the tested specimens can be found in Appendix B. Each graph contains the results of three specimens tested under similar conditions.

The cube compressive strength for concrete is typically greater than those obtained from cylinders. This is due to size effect and can be in the order of 5-25%. As the compressive strength of concrete increases, the percentage difference is decreasing as provided by British Standards Institute Draft for Development [55] in Table 14. Using linear interpolation, the normal compressive strength is 43.8MPa, and the high compressive strength is 60.4MPa.

Table 14: the strength difference between cylinder and cube compressive strengths [55]

Cylinder Strength		Cube Strength	
MPa	Psi	MPa	Psi
12	1740	15	2175
16	2320	20	2900
20	2900	25	3625
25	3625	30	4350
30	4350	37	5365
35	5075	45	6525
50	7250	60	8700

3.2 Steel material tests:

3.2.1 Coupon test:

Standard sized samples were prepared from each of the three steel tubes used to confine the concrete. The tested samples were loaded under three loading rates which are 2mm/min, 50mm/min, 500mm/min. using the measured dimensions of each sample and the data provided

by the machine, the engineering stress and engineering strain values were calculated and presented in Table 15.

Table 15: coupon test results

Rate	ID	yield strain	yield stress (MPa)	Ultimate Strain	Ultimate Stress (MPa)	AVR. yield strain	AVR. yield stress (MPa)	AVR. Ultimate Strain	AVR. Ultimate Stress (MPa)
Normal rate 2 (mm/min)	$t_{3.1}$ R_2 -1	0.0124	352	0.2357	442	0.01329	352	0.2414	444
	$t_{3.1}$ R_2 -2	0.0142	351	0.2472	446				
	$t_{5.6}$ R_2 -1	0.0086	245	0.1454	316	0.00955	273	0.1430	332
	$t_{5.6}$ R_2 -2	0.0105	301	0.1405	349				
	$t_{3.6}$ R_2 -1	0.0139	335	0.2808	406	0.01370	350	0.2504	421
	$t_{3.6}$ R_2 -2	0.0135	365	0.2199	436				
Intermediate rate 50 (mm/min)	$t_{3.1}$ R_{50} -1	0.0137	318	0.1515	456	0.01425	334	0.1415	456
	$t_{3.1}$ R_{50} -2	0.0144	351	0.1261	460				
	$t_{3.1}$ R_{50} -3	0.0147	331	0.1470	451				
	$t_{5.6}$ R_{50} -1	0.0229	346	0.0818	409	0.02330	356	0.0765	416
	$t_{5.6}$ R_{50} -2	0.0237	367	0.0712	424				
	$t_{3.6}$ R_{50} -1	0.0145	337	0.1224	423	0.01551	339	0.1133	423
	$t_{3.6}$ R_{50} -2	0.0165	340	0.1042	423				
High rate 500 (mm/min)	$t_{3.1}$ R_{500} -1	0.0186	352	0.2547	462	0.02107	369	0.2483	466
	$t_{3.1}$ R_{500} -2	0.0211	382	0.2399	471				
	$t_{3.1}$ R_{500} -3	0.0235	373	0.2503	466				
	$t_{5.6}$ R_{500} -1	0.0307	372	0.1935	422	0.03359	379	0.2070	430
	$t_{5.6}$ R_{500} -2	0.0364	386	0.2205	437				
	$t_{3.6}$ R_{500} -1	0.0251	373	0.2790	440	0.02472	370	0.2530	440
	$t_{3.6}$ R_{500} -2	0.0243	367	0.2269	440				

It should be noted that $t_{3.1}$, $t_{5.6}$ and $t_{3.6}$ refer to the different steel tube thickness of 3.1mm, 3.6mm and 5.6mm, respectively. Similarly, R_2, R_{50} and R_{500} refer to the different stain rates of 2mm/min, 50mm/min and 500mm/min, respectively. Since the properties of the steel samples are almost identical for the same strain rate, it is safe to assume that the material properties of the

three steel tubes are similar. Note that the yield stress and the ultimate stress of the sample increase as the loading rate increases.

Figure 18 shows one of the coupon samples tested under low strain rate. As expected, the failure of all samples took place in gage length segment of the specimen due to the reduction in the cross sectional area. In addition, all the samples displayed an acceptable amount of necking just before rapture as displayed in Figure 18. It should be mentioned that only one of the samples ($t_{5.6}$ R_2 -2) slipped from the machines grips during the test and it was redone again. The slipping occurred because the grip areas of the specimens were manufactured based on the standard sizes, but the available grips of the testing machine were found to be slightly smaller.

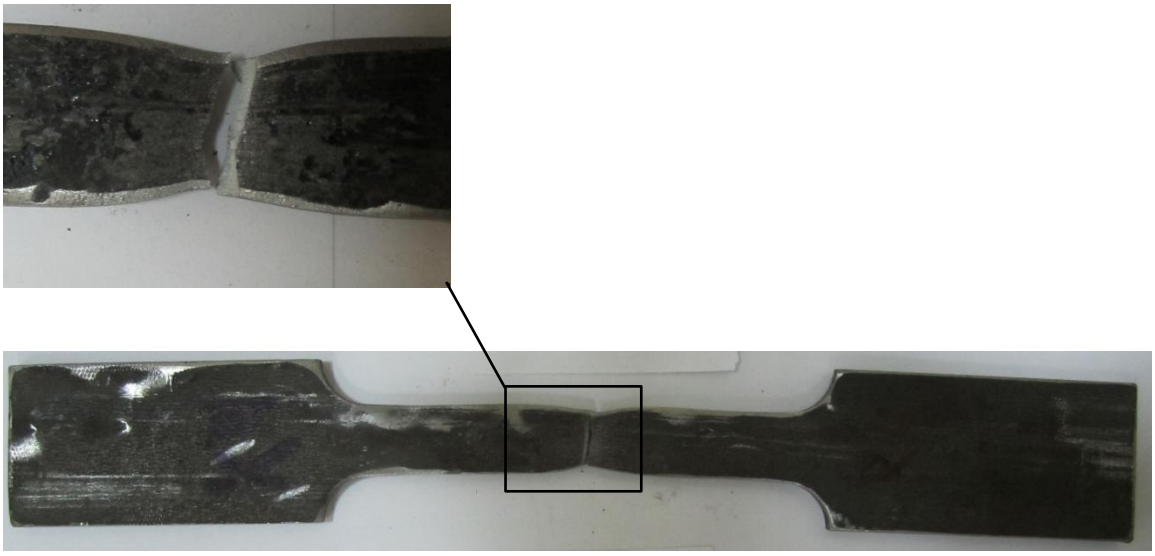

Figure 18: tested steel coupon specimen

3.2.2 Steel tube test:

A total of ten hollow steel tube specimens were loaded till failure. These samples were divided among the two loading rates, five for each. Table 16 shows the summary of the results,

where R_{60} and $R_{0.6}$ refers to the loading rate of 60kN/s and 0.6kN/s, respectively. Also, $t_{3.1}$, $t_{5.6}$ and $t_{3.6}$ refer to the steel tube thickness of 3.1mm, 3.6mm, and 5.6mm, respectively.

Table 16: empty steel tubes compressive test results

ID	Ultimate Load	Ultimate Stress	AVR. Ultimate Load	AVR. Ultimate Stress
tube $t_{3.1}$ R_{60} -1	563	677	-	-
tube $t_{5.6}$ R_{60} -1	789	807	789	807
tube $t_{5.6}$ R_{60} -2	789	807		
tube $t_{3.6}$ R_{60} -1	480	757	481	758
tube $t_{3.6}$ R_{60} -2	482	759		
tube $t_{3.1}$ $R_{0.6}$ -1	556	668	-	-
tube $t_{5.6}$ $R_{0.6}$ -1	766	784	767	784
tube $t_{5.6}$ $R_{0.6}$ -2	767	784		
tube $t_{3.6}$ $R_{0.6}$ -1	464	731	467	736
tube $t_{3.6}$ $R_{0.6}$ -2	471	742		

For all applied loading rates, the dominant failure mode was local buckling. Note that the $L/D = 2$ is small enough to prevent the occurrence of Euler buckling. The local buckling in all of the specimens was localized near only one of the loading ends as shown in Figure 19.

Figure 19: failure mode of empty steel tube

Figure 20 shows the stress-displacement diagrams of hollow steel tubes with a thickness of 5.6mm and an outer diameter of 114mm. the graph shows the effect of different loading rates R60 and R0.6 which corresponds to 60kN/s and 0.6kN/s, respectively. Apparently, the stiffness of the empty steel tubes is not affected by the change in the loading rate. On the other hand, the yield and the ultimate stresses have marginally increased with the increase of the loading rate due to the effects of the high loading rates on the behavior of the material as illustrated in the introduction chapter. In addition, the ductility of the section is not influenced by the loading rate.

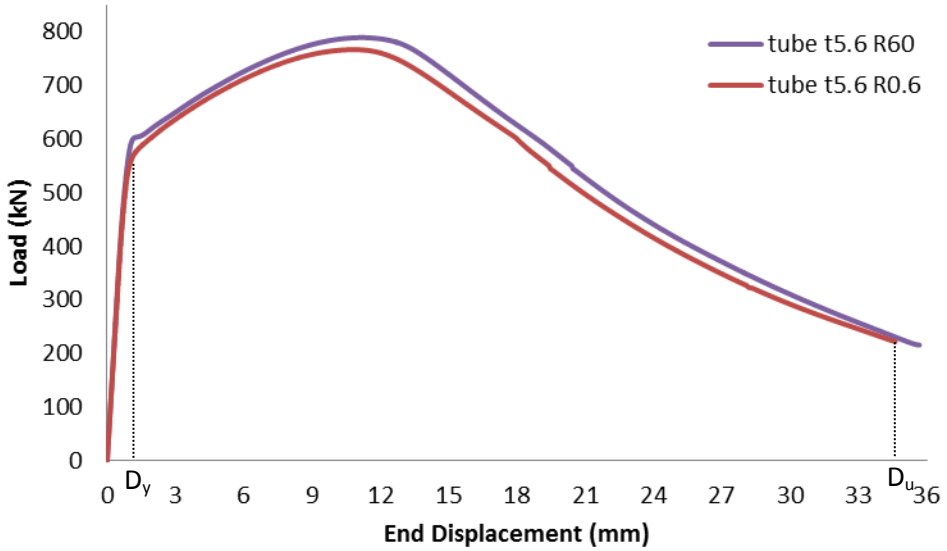

Figure 20: Stress-End displacement diagram of empty steel tube under different loading rates

Figure 21 shows the stress-displacement curves of hollow steel tubes with two thicknesses of 5.6mm and 3.6mm, denoted by $t_{5.6}$ and $t_{3.6}$, with an outer diameter of 114mm. The graph shows the effect of different steel tube thicknesses given that the applied loading rate is fixed for both which is 60kN/s. Note that, the stiffness of the empty steel tubes is hardly affected by the change in the tube thickness. However, the ultimate stress, the toughness and the ductility have increased with the increase in the tube thickness. The $\boldsymbol{D_u/D_y}$ ratio is used in this study to

indicate the specimen's ductility, where $\boldsymbol{D_u}$ is the ultimate displacement and $\boldsymbol{D_y}$ is the linear limit state displacement as shown in Figure 20. The ductility of tube $t_{5.6}$ $R_{0.6}$ can be calculated as $\mathbf{34.6/0.9 = 38.4}$ which is less than that of tube $t_{5.6}$ R_{60} = 35.8. This improvement resulted from the increase in the structural steel contact area per circumferential unit length near the loading ends which allows for more strain hardening in the element. Nevertheless, the limit stress of elasticity decreases with the increase of tube thickness.

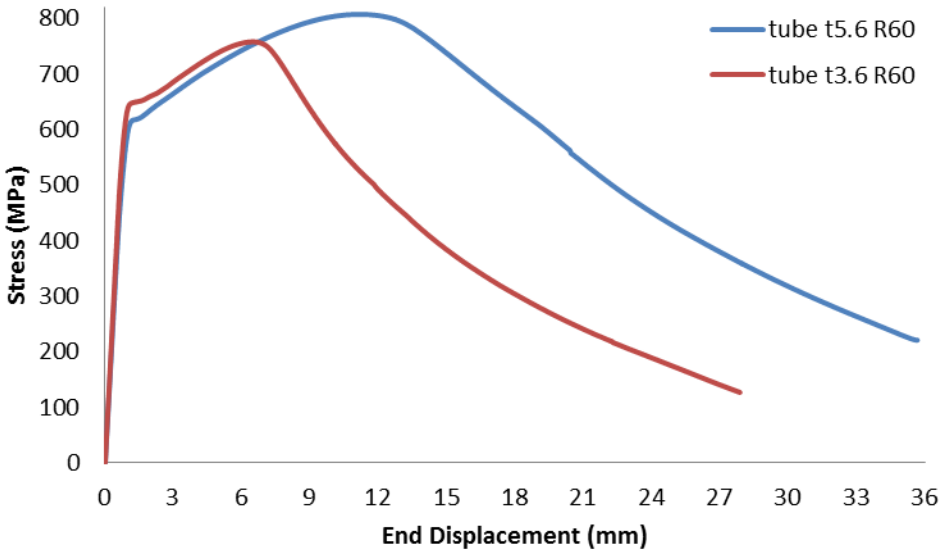

Figure 21: Stress-End displacement diagram of empty steel tube with different thicknesses

Figure 22 shows the stress-displacement diagrams of two empty steel tubes $t_{3.6}$ R_{60} and $t_{3.2}$ R_{60} with two different outer diameters of 114mm and 167mm, respectively. This graph is intended to show the effect of different steel tube's outer diameter when similar loading rate of 60kN/s is applied. Just like the effect of tube thickness, the change in outer diameter barely influenced the stiffness of the empty steel tube. In addition, the strain hardening region shortened greatly with the increase of the tube's diameter. This resulted from the decrease in the structural steel contact area per circumferential unit length near the loading ends which allows for less

strain hardening in the element. Note that the ultimate stress, toughness and the ductility have increased (from 27.9 to 35.8) with the increase of the tube's outer diameter which resulted from the increase in the strain hardening region of the element. However, the limit stress of elasticity slightly decreases with the increase of tube's diameter.

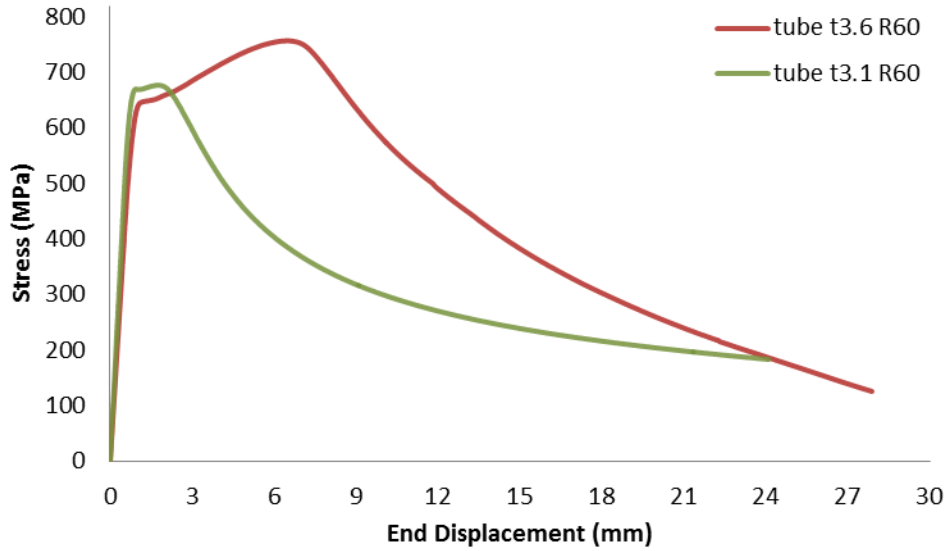

Figure 22: Stress-End displacement diagram of empty steel tube with different outer diameters

Figure 23 shows the stress-displacement diagrams of three empty steel tubes with different outer diameters and tube thicknesses, while the loading rate is similar 60kN/s. For comparison purposes, the diameter-to-thickness ratio ($^{D}/_{t}$) will be used, which is used originally for CFST and CCFST elements. Note that part (a) of Figure 23 is just an enlargement of the elastic range of the three specimens in part (b) of the graph. As the $^{D}/_{t}$ ratio decreases the ultimate stress, the ductility (from 26.1 to 27.9), the toughness and the strain hardening region increase because of the increase in the structural steel contact area per circumferential unit length near the loading ends that allows for additional strain hardening in the element. Note that the

steel tube with $^{D}/_{t}$=54 further away from the other two tubes because of the huge jump in the section's moment of inertia. It can be observed that the limit stress of elasticity is directly proportional to the $^{D}/_{t}$ ratio.

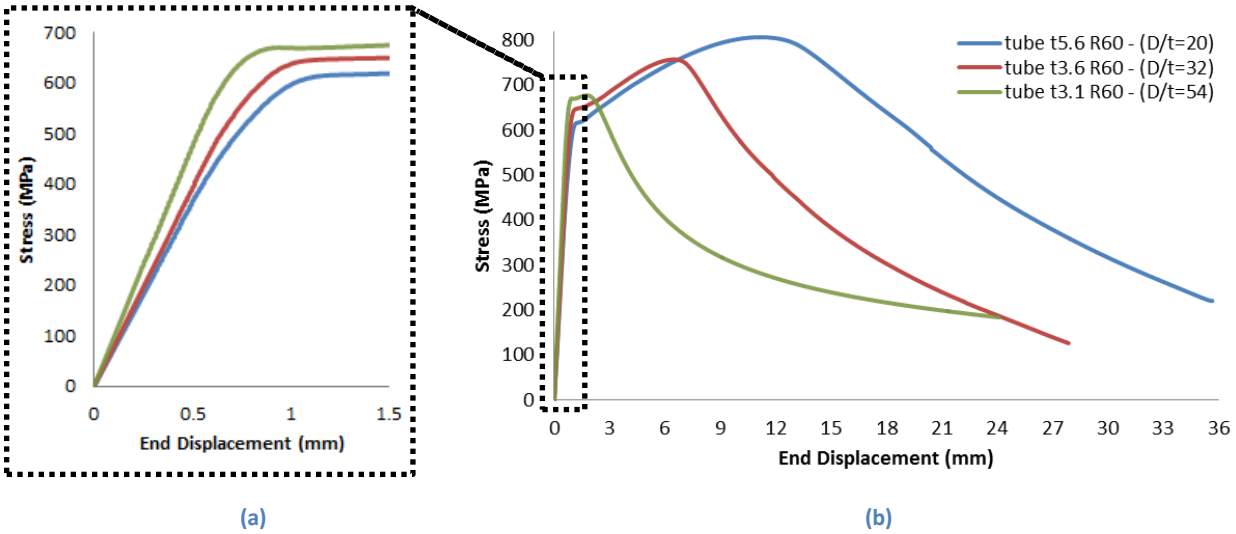

Figure 23: Stress-End displacement diagram of empty steel tube with different $^{D}/_{t}$ ratios

The stress-end shortening diagrams of the remaining specimens are displayed in Appendix A. all the graphs exhibited similar behavior.

3.3 CFST test results:

The results of thirty three tested CFST specimens are summarized in

Table **17**, where R_{60} and $R_{0.6}$ refers to the applied loading rate of 60kN/s and 0.6 kN/s, f_{60} and f_{44} refers to a concrete infill compressive strength of 60MPa and 44MPa,, and $D_{167}t_{3.1}$, $D_{114}t_{3.6}$ and $D_{114}t_{5.6}$ relates to a $\mathbf{^{D}/_{t}}$ of 54, 32 and 20, respectively. The CFST ultimate stress ($\boldsymbol{\sigma_{exp}}$) in

Table **17** is calculated by dividing the ultimate load carrying capacity ($\mathbf{N_{exp}}$) by the total area of the CFST element ($\mathbf{A = \frac{\pi}{4} D^2}$).

Table 17: test results of concrete filled steel tubes

ID	N_{exp} (kN)	σ_{exp} (MPa)	$avr.\ N_{exp}$ (kN)	$avr.\ \sigma_{exp}$ (MPa)
$R_{60}\,f_{60}\,D_{167}\,t_{3.1}$ - 1	1946	889	1952	89
$R_{60}\,f_{60}\,D_{167}\,t_{3.1}$ - 2	1954	89		
$R_{60}\,f_{60}\,D_{167}\,t_{3.1}$ - 3	1955	89		
$R_{60}\,f_{60}\,D_{114}\,t_{5.6}$ - 1	1369	134	1395	137
$R_{60}\,f_{60}\,D_{114}\,t_{5.6}$ - 2	1407	138		
$R_{60}\,f_{60}\,D_{114}\,t_{5.6}$ - 3	1408	138		
$R_{60}\,f_{44}\,D_{114}\,t_{5.6}$ - 1	1334	131	1309	128
$R_{60}\,f_{44}\,D_{114}\,t_{5.6}$ - 2	1315	129		
$R_{60}\,f_{44}\,D_{114}\,t_{5.6}$ - 3	1278	125		
$R_{60}\,f_{44}\,D_{167}\,t_{3.1}$ - 1	1735	79	1720	79
$R_{60}\,f_{44}\,D_{167}\,t_{3.1}$ - 2	1705	78		
$R_{60}\,f_{60}\,D_{114}\,t_{3.6}$ - 1	1110	109	1109	109
$R_{60}\,f_{60}\,D_{114}\,t_{3.6}$ - 2	1120	110		
$R_{60}\,f_{60}\,D_{114}\,t_{3.6}$ - 3	1097	108		
$R_{60}\,f_{44}\,D_{114}\,t_{3.6}$ - 1	1074	105	1038	102
$R_{60}\,f_{44}\,D_{114}\,t_{3.6}$ - 2	1010	99		
$R_{60}\,f_{44}\,D_{114}\,t_{3.6}$ - 3	1029	101		
$R_{0.6}\,f_{60}\,D_{167}\,t_{3.1}$ - 4	1869	85	1873	86
$R_{0.6}\,f_{60}\,D_{167}\,t_{3.1}$ - 5	1876	86		
$R_{0.6}\,f_{60}\,D_{114}\,t_{5.6}$- 4	1359	133	1365	134
$R_{0.6}\,f_{60}\,D_{114}\,t_{5.6}$- 5	1360	133		
$R_{0.6}\,f_{60}\,D_{114}\,t_{5.6}$- 6	1376	135		
$R_{0.6}\,f_{44}\,D_{114}\,t_{5.6}$- 4	1332	131	1314	129
$R_{0.6}\,f_{44}\,D_{114}\,t_{5.6}$- 5	1301	128		
$R_{0.6}\,f_{44}\,D_{114}\,t_{5.6}$- 6	1309	128		
$R_{0.6}\,f_{44}\,D_{167}\,t_{3.1}$ - 4	1758	80	1710	78
$R_{0.6}\,f_{44}\,D_{167}\,t_{3.1}$ - 5	1661	76		
$R_{0.6}\,f_{60}\,D_{114}\,t_{3.6}$ - 4	1097	107	1095	107
$R_{0.6}\,f_{60}\,D_{114}\,t_{3.6}$ - 5	1087	107		
$R_{0.6}\,f_{60}\,D_{114}\,t_{3.6}$ - 6	1100	108		
$R_{0.6}\,f_{44}\,D_{114}\,t_{3.6}$ - 4	1055	103	1042	102
$R_{0.6}\,f_{44}\,D_{114}\,t_{3.6}$ - 5	1045	102		
$R_{0.6}\,f_{44}\,D_{114}\,t_{3.6}$ - 6	1028	101		

For a given common loading condition and section properties, a set of two or three specimens are tested. Afterwards, the average data of each set is used for further analysis. An example of these sets is provided in Figure 24, while the rest are presented in Appendix A.

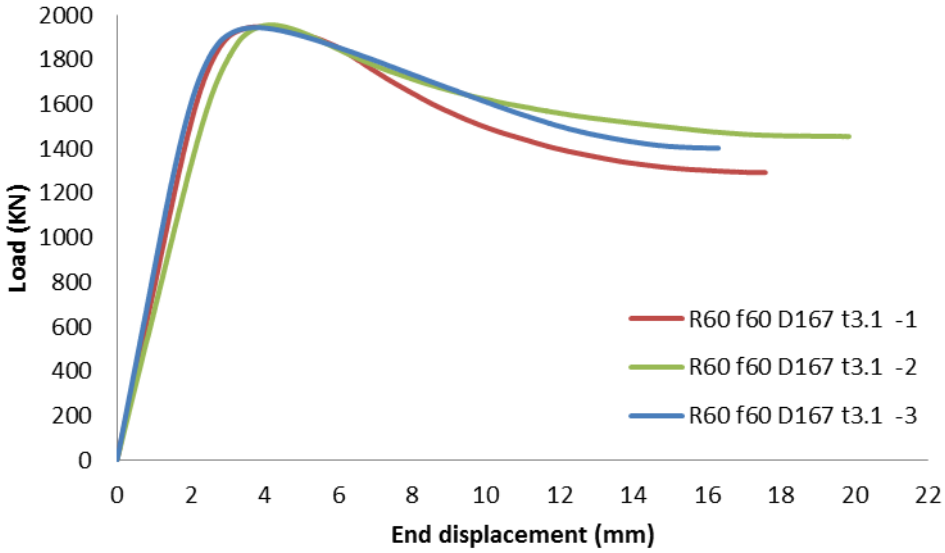

Figure 24: Load-End displacement diagram of three CFST elements with D/t= 54, f'_c =60MPa and loading rate=60kN/s

Figure 24 shows the load-deformation diagram of three CFST samples with identical properties and similar testing conditions. The average ultimate axial capacity of the three samples is 1948kN, such that the percentage difference of any of the samples and the average does not exceed 0.4%. In addition, the post ultimate load decreases with a decreasing rate resulting in reduction of the section's ability to dissipate energy. On the other hand, the stiffness of the $R_{60}f_{60}D_{167}t_{3.1}$-1 and $R_{60}f_{60}D_{167}t_{3.1}$-3 is almost the same while $R_{60}f_{60}D_{167}t_{3.1}$-2 is a little bit different. As a result, $R_{60}f_{60}D_{167}t_{3.1}$-1 or $R_{60}f_{60}D_{167}t_{3.1}$-3 can be used for further analysis and comparisons.

3.3.1 f'_c effect:

Two different concrete compressive strengths are studied in this research. The compressive strengths conducted by the cylinder tests were 44MPa and 60MPa representing normal strength and high strength, respectively.

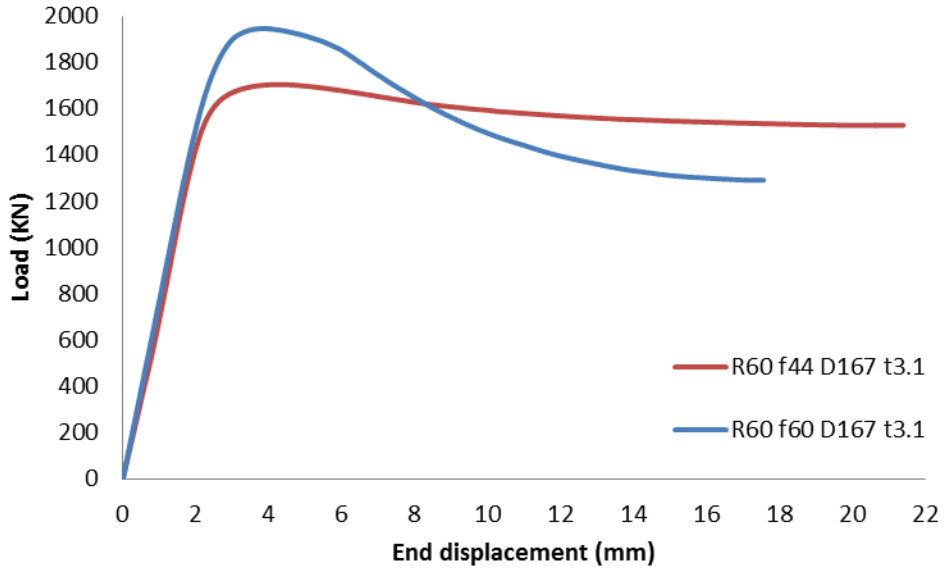

Figure 25: Load-End displacement diagram of CFST element with $^{D}/_{t}$= 54 and different f'_c

Figure 25 shows the load-deformation diagram of two CFST samples with $^{D}/_{t}$ ratio of 54, loading rate of 60kN/s and two different concrete infill compressive strengths. The ultimate axial capacity of the CFST specimen increased by 14.2% when the concrete infill compressive strength increased by 36.4%. It is noticeable that the stiffness of both samples is almost identical and is not affected by the change in the compressive strength of the concrete infill. In addition, the post peak degradation rate of the $R_{60}f_{60}D_{167}t_{3.1}$ is much higher than $R_{60}f_{44}D_{167}t_{3.1}$ because the amount of confinement present on the high strength concrete from the steel tube is relatively small compared to its f'_c. On the other hand, when f'_c is small as the case of $R_{60}f_{44}D_{167}t_{3.1}$, the confining pressure is sufficient to enhance the specimen's post peak behavior.

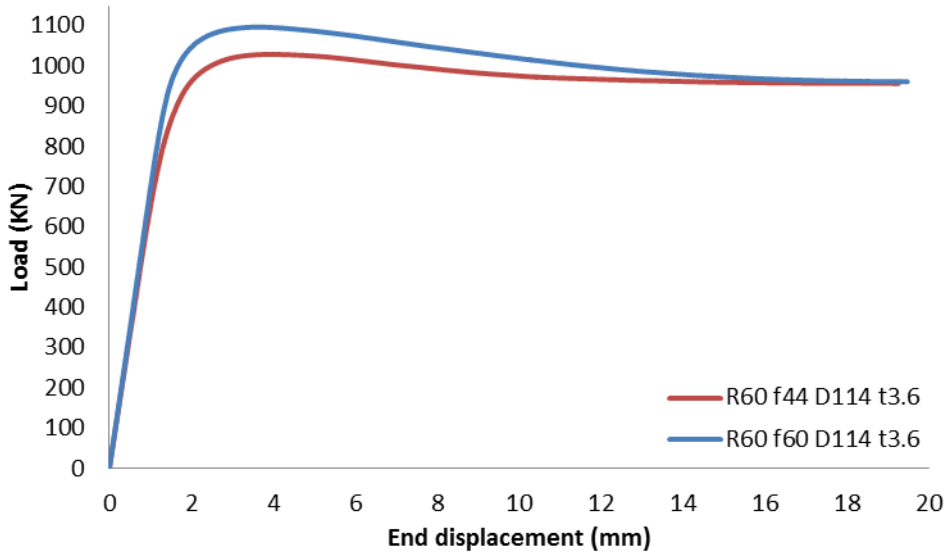

Figure 26: Load-End displacement diagram of CFST element with $^{D}/_{t}$= 32 and different f_c'

Figure 26 shows the load-deformation diagram of two CFST samples with $^{D}/_{t}$ ratio of 32, loading rate of 60kN/s and two different concrete infill compressive strengths. The ultimate axial capacity of the CFST specimen increased by 6.6% when the concrete infill compressive strength increased by 36.4%. Furthermore, the post peak degradation rate of the $R_{60}f_{60}D_{114}t_{3.6}$ is slightly higher than $R_{60}f_{44}D_{114}t_{3.6}$ because the confining pressure (f_1) in $R_{60}f_{60}D_{114}t_{3.6}$ is somewhat small compared to the f_c' of concrete core, unlike $R_{60}f_{44}D_{114}t_{3.6}$ which have smallerf_c'. Also, the stiffness of both samples is almost identical and is not affected by the change in the compressive strength of the concrete infill.

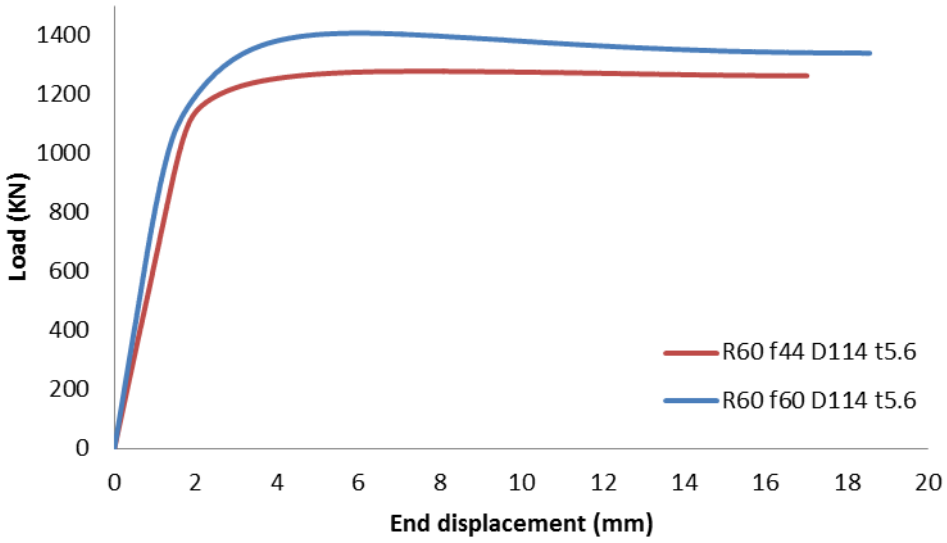

Figure 27: Load-End displacement diagram of CFST element with $^{D}/_{t}$= 20 and different f_c'

Figure 27 shows the load-deformation diagram of two CFST samples with $^{D}/_{t}$ ratio of 20, loading rate of 60kN/s and two different concrete infill compressive strengths. In this case, the ultimate axial capacity of the CFST specimen increased only by 10.1% when the concrete infill compressive strength increased by 36.4%. However, the post peak degradation rate of the $R_{60}f_{60}D_{114}t_{3.6}$ is almost the same as $R_{60}f_{44}D_{114}t_{3.6}$. The same comparison was performed on the CFST specimens under low loading rate of 0.6kN/s the load-deformation diagrams of these tests are shown in Appendix B. The increase in the ultimate strength that is associated with the decrease in toughness of $R_{60}f_{60}D_{167}t_{3.1}$ when compared to $R_{60}f_{44}D_{167}t_{3.1}$, is the same for $R_{0.6}f_{60}D_{167}t_{3.1}$when compared to $R_{0.6}f_{44}D_{167}t_{3.1}$.

Figure 25, Figure 26 and Figure 27 present the effects of concrete compressive strength on the behavior of CFST elements at different $^{D}/_{t}$ ratios. As expected, the ultimate axial capacity of the CFST increases as the f_c' increases for all the tested cases. Nevertheless, the CFST stiffness is apparently not affected by the concrete infill compressive strength as its $^{D}/_{t}$

ratio increases. In the graphs of higher ($^{D}/_{t}$) ratios the stiffness is identical for both samples. Moreover, the post peak degradation of the high strength concrete specimens is improved as the confining pressure (f_1) increases while the samples with normal strength concrete core are the same. This phenomenon resulted from the fact that the concrete core degradation behavior improves only if sufficient f_1 is provided. As the f_c' increases the required confining pressure increases. Also, any further increase in the confinement beyond the neededf_1, will result in very minor improvement of the post peak degradation behavior and that is why the normal strength concrete specimens behavior did not change in these cases.

3.3.2 Effect of D/t ratio:

The effect of diameter-to-steel-tube-thickness ratio ($^{D}/_{t}$) on the CFST element behavior is recognized even in design code equations. In this study three $^{D}/_{t}$ ratios are used for analysis 54, 32 and 20. These ratios are obtained either by changing the section's outer diameter from 114mm to 167mm or by changing the tube thickness from 3.1mm to 5.6mm.

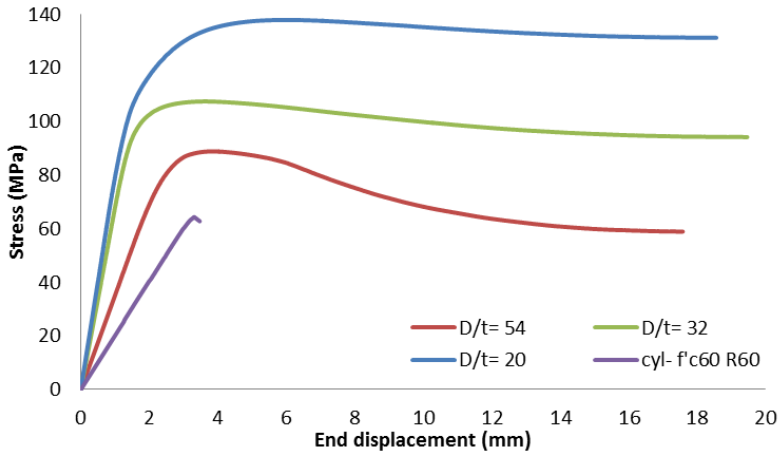

Figure 28: Stress-End displacement diagram of CFST element with loading rates= 60kN/s, f_c'= 60MPa and different $^{D}/_{t}$

Figure 28 shows the stress-deformation diagram of three CFST samples with similar concrete infill compressive strength of 60MPa, loading rate of 60kN/s and three different $^{D}/_{t}$ ratios. The engineering stress is expressed as the applied load divided by the total cross sectional area of the CFST. Evidently, the strength and stiffness of bare concrete cylinder is considerably increased when confined with steel tube because of the enhancement of the concrete core behavior due to the confinement from the steel tube. Also, the stiffness of CFST rises as the $^{D}/_{t}$ ratio drops from 54 to 32 because smaller $^{D}/_{t}$ ratios result in higher confining pressure f_1 which will increase the f_c'. Hence, the modulus of elasticity of the concrete infill will increase because of their proportional correlation. However, the increase of the element's stiffness when the $^{D}/_{t}$ ratio drops from 32 to 20 is very small compared to the drop from 54 to 32. As expected, the ultimate load carrying capacity increases as the $^{D}/_{t}$ ratio increases. Note that, the post peak region of the curve in the case of bare concrete cylinder is minimal which is why the concrete has very brittle failure modes and limited ability to dissipate energy. As the $^{D}/_{t}$ ratio increases, the toughness of the CFST section is significantly increased.

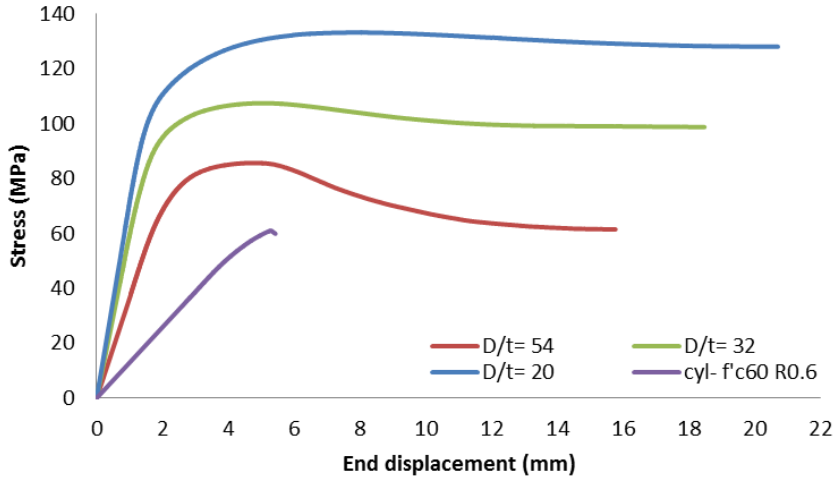

Figure 29: Stress-End displacement diagram of CFST element with loading rates= 0.6kN/s, f_c'= 60MPa and different $^{D}/_{t}$

Figure 29 shows the stress-deformation diagram of three CFST samples with similar concrete infill compressive strengths of 60MPa, loading rate of 0.6kN/s and three different D/t ratios. The stress is a measure of the applied load divided by the total cross sectional area of the CFST. Similar to the high loading rate case, the ultimate load carrying capacity increases as the D/t ratio decreases due to the increase in the concrete infill compressive strength. Also, the post peak region of the curve in the case of bare concrete cylinders is significantly lesser than that of CFST specimen because the concrete is a very brittle material by nature and the presence of the ductile steel in the CFST element is responsible for the added ductility and toughness. As the D/t ratio is increased, the toughness of the CFST specimens notably increases. The effect of confinement on the specimen's stiffness in this case is almost the same as that of high loading rate. Thus, the stiffness increase due to confinement effects by the steel tube is not affected by the loading rate.

Similar analysis was performed on normal compressive strength concrete infill and the stress-deformation diagrams of these tests are shown in Appendix B. The effect of (D/t) on the behavior of the CFST elements for normal strength concrete is similar to the one with high strength concrete infill.

Figure 30 associates the ultimate compressive strength of a CFST element with its D/t ratio. The CFST elements are divided into four different groups based on the loading rate and the f_c' of the concrete infill. As expected, the CFST's axial capacity decreases as the D/t increases due to the reduction in confinement associated with it. Note that the reduction rate of ultimate stress is affected by the concrete infill compressive strength and the loading rate which can be observed when comparing the results of CFST elements with $f_{c\,60}'$ R_{60} and those with $f_{c\,44}'$ $R_{0.6}$.

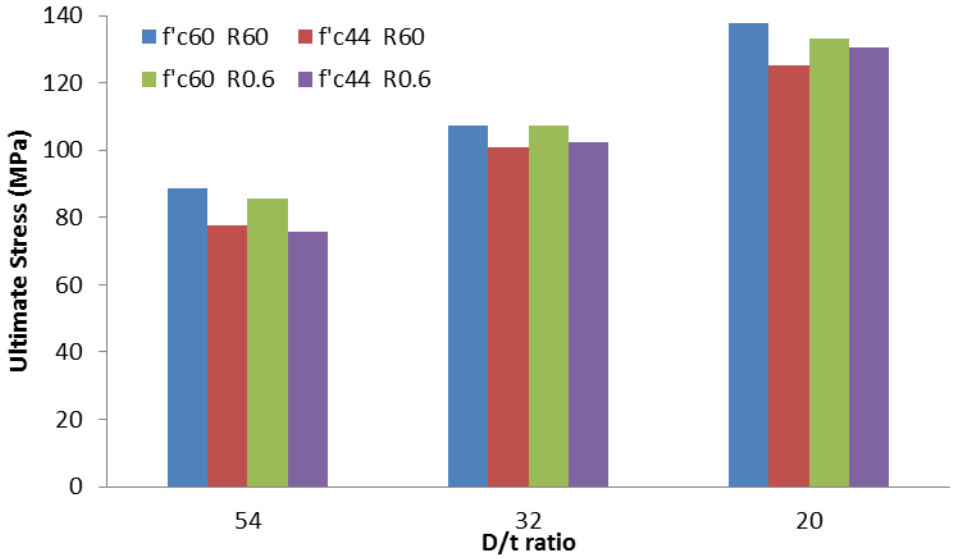

Figure 30: $^{D}/_{t}$ vs. ultimate stress chart of CFST element

3.3.3 Effect of loading rate:

The effect of different loading rates on the behavior of CFST elements is discussed in this section. Due to the limitation of the available testing machine, only two loading rates were used to test the samples, a low rate of 0.6kN/s and a relatively high rate of 60kN/s.

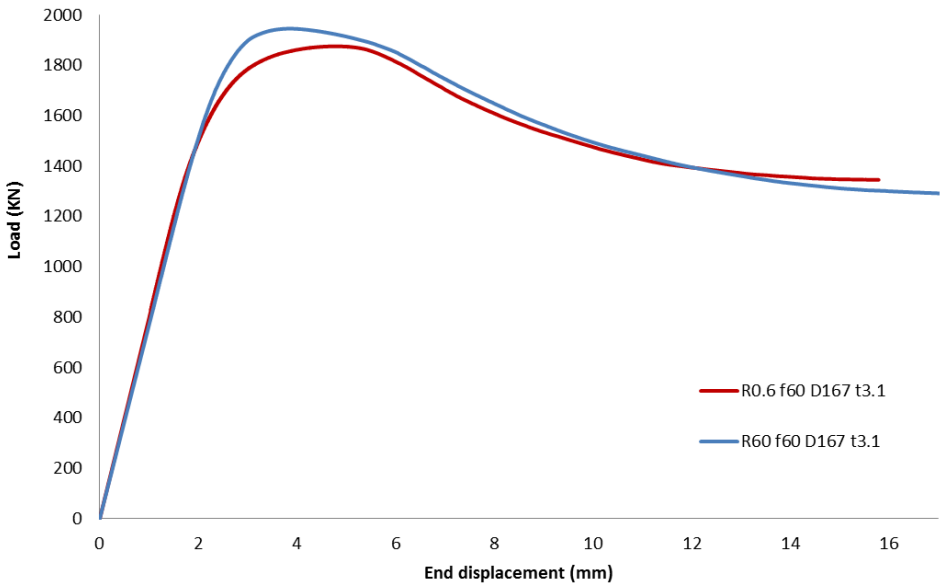

Figure 31: Load-End displacement diagram of CFST element with $^{D}/_{t}$= 54 and different loading rates

Figure 31 shows the load-deformation diagram of two CFST samples with similar D/t of 54, concrete infill compressive strengths of 60MPa and two different loading rates. The ultimate axial capacity of the CFST specimen increased by 3.7% when the loading rate increased by hundred times. It is noticeable that the stiffness of both samples is identical and is not affected by the change in the applied loading rate. In addition, the post peak degradation rate of the $R_{0.6}f_{60}D_{167}t_{3.1}$ is very similar to $R_{60}f_{60}D_{167}t_{3.1}$. i.e.: the loading rate has minimal influence on the behavior.

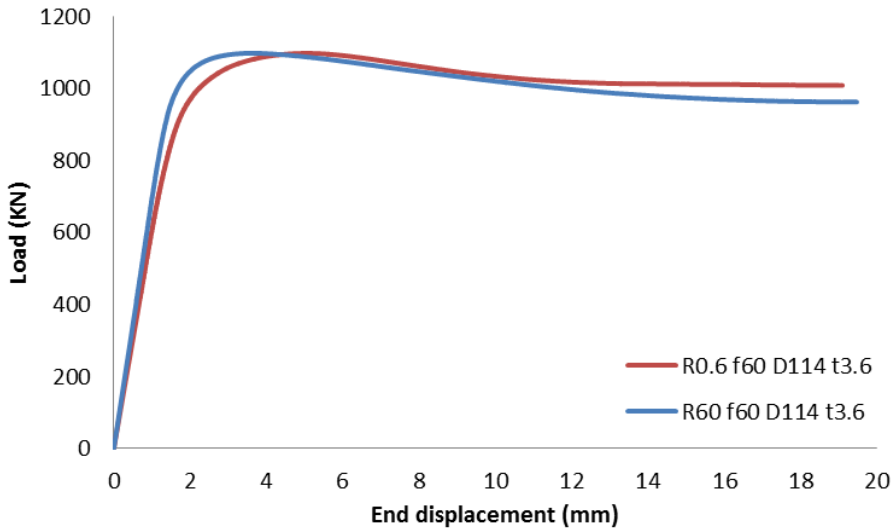

Figure 32: Load-End displacement diagram of CFST element with D/t= 32 and different loading rates

Figure 32 shows the load-deformation diagram of two CFST samples with similar D/t of 32, concrete infill compressive strengths of 60MPa and two different loading rates. In this case, the ultimate axial capacity of the CFST specimen increased only by 0.04% when the loading rate increased by hundred times. However, the post peak degradation rate of the $R_{0.6}f_{60}D_{114}t_{3.6}$ is slightly higher than $R_{60}f_{60}D_{114}t_{3.6}$. i.e.: the loading rate has minimal influence on the behavior.

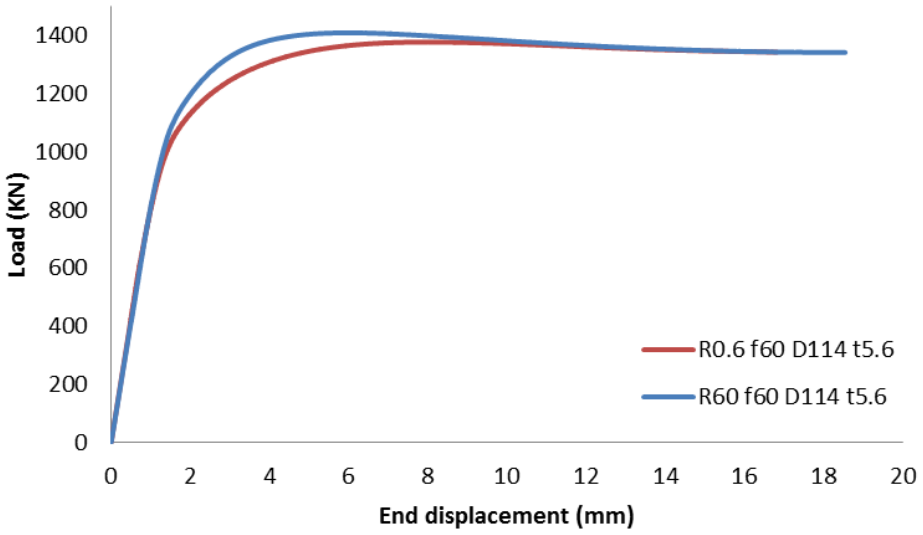

Figure 33: Load-End displacement diagram of CFST element with $^{D}/_{t}$= 20 and different loading rates

Figure 33 shows the load-deformation diagram of two CFST samples with similar $^{D}/_{t}$ of 20, concrete infill compressive strengths of 60MPa and two different loading rates. The ultimate axial capacity of the CFST specimen increased by 2.3% when the loading rate increased by hundred times. Furthermore, the post peak degradation rate of both specimens is insignificant. Also, the stiffness of both samples is identical and is not affected by the change in loading rate.

The same comparison was made on the CFST samples filled with normal compressive strength concrete f_c'= 44MPa. The load-deformation diagrams of these tests are shown in Appendix B. Note that the effect of loading rate on the CFST specimens was not affected by the change in concrete infill compressive strength. In other words, the increase in the ultimate strength of $R_{60}f_{60}D_{167}t_{3.1}$ when compared to $R_{0.6}f_{60}D_{167}t_{3.1}$, is the same for $R_{60}f_{44}D_{167}t_{3.1}$ when compared to $R_{0.6}f_{44}D_{167}t_{3.1}$.

3.4 CCFST test results:

In this section, the results of eighteen tested CCFST specimens are presented and discussed. Each tested set of specimens have similar loading conditions and section properties. Similar to CFSTs, the average data of each set is used for further analysis. Figure 34 displays the results of one of these tested CCFST sets, while the rest of them are provided in Appendix B.

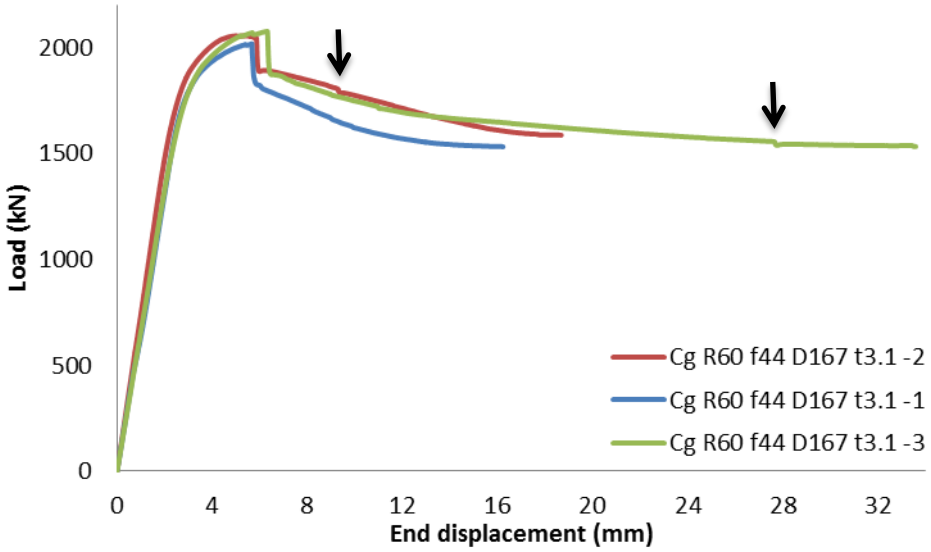

Figure 34: Load-End displacement diagram of three CCFST elements with D/t= 54, f'_c=60MPa and loading rate=60kN/s

Figure 34 shows the load-deformation diagram of three CCFST samples with identical properties and similar testing conditions. The average ultimate axial capacity of the three samples is 2048kN, such that the percentage difference of any of the samples and the average does not exceed 1.54%. In each of these curves a sudden drop at the ultimate load is apparent due to the explosive rapture of GFRP wraps near the mid-section region of the samples. However, if the GFRP rapture took place near the edges of the specimen a lesser drop of the exhibited axial load occurs as pointed out by the arrow in C_g R_{60} f_{44} D_{167} $t_{3.1}$ -3. This smaller drop is attributed to the fact that the mid-section wrapping continues to provide confinement to the specimen.

(a) Rapture in the mid-height (b) Rapture near loading end

Figure 35: Failure mode of a CCFST specimen

As displayed in (a) Rapture in the mid-height (b) Rapture near loading end Figure 35, the explosive rapture failure first take place near the sample's middle region. Then minor ruptures occur near the specimens loaded edges. The stiffness of the C_g R_{60} f_{44} D_{167} $t_{3.1}$ -1 and C_g R_{60} f_{44} D_{167} $t_{3.1}$ -3 is almost the same while C_g R_{60} f_{44} D_{167} $t_{3.1}$ -2 is a little bit different. Note that the post rapture region of C_g R_{60} f_{44} D_{167} $t_{3.1}$ -3 is larger than the others. As a result, C_g R_{60} f_{44} D_{167} $t_{3.1}$ -2 is preferred for usage in further analysis and comparisons.

Table 18 summarizes the ultimate carrying capacities of the CCFST elements. Note that the values of each set are within the range of one standard deviation away from their mean.

Figure 36 shows the load-displacement diagrams of a CCFST specimen and its CFST benchmark counterpart (the same specimen without GFRP wrapping). The loading rate of 60kN/s, the concrete infill strength and the D/t ratio of 32 are all similar. This graph shows the

improvement on the CFST's behavior when wrapped with GFRP sheets. As expected, the axial capacity of the CFST considerably improved with the application of wraps because of additional

Table 18: Summary of the CCFST testing results

ID	Ultimate Load (kN)	Ultimate Stress (MPa)	AVG. Ultimate Load (kN)	AVG. Ultimate Stress (MPa)
$C_g\,R_{60}\,f_{60}\,D_{167}\,t_{3.1}$ - 1	2055	94	2085	95
$C_g\,R_{60}\,f_{60}\,D_{167}\,t_{3.1}$ - 2	2075	95		
$C_g\,R_{60}\,f_{60}\,D_{167}\,t_{3.1}$ - 3	2124	97		
$C_g\,R_{60}\,f_{60}\,D_{114}\,t_{5.6}$ - 1	1584	155	1575	154
$C_g\,R_{60}\,f_{60}\,D_{114}\,t_{5.6}$ - 2	1567	154		
$C_g\,R_{60}\,f_{60}\,D_{114}\,t_{5.6}$ - 3	1574	154		
$C_g\,R_{60}\,f_{44}\,D_{114}\,t_{5.6}$ - 1	1533	150	1538	151
$C_g\,R_{60}\,f_{44}\,D_{114}\,t_{5.6}$ - 2	1533	150		
$C_g\,R_{60}\,f_{44}\,D_{114}\,t_{5.6}$ - 3	1547	152		
$C_g\,R_{60}\,f_{44}\,D_{167}\,t_{3.1}$ - 1	2017	92	2048	94
$C_g\,R_{60}\,f_{44}\,D_{167}\,t_{3.1}$ - 2	2053	94		
$C_g\,R_{60}\,f_{44}\,D_{167}\,t_{3.1}$ - 3	2075	95		
$C_g\,R_{60}\,f_{60}\,D_{114}\,t_{3.6}$ - 1	1337	131	1326	130
$C_g\,R_{60}\,f_{60}\,D_{114}\,t_{3.6}$ - 2	1319	129		
$C_g\,R_{60}\,f_{60}\,D_{114}\,t_{3.6}$ - 3	1323	130		
$C_g\,R_{60}\,f_{44}\,D_{114}\,t_{3.6}$ - 1	1241	122	1268	124
$C_g\,R_{60}\,f_{44}\,D_{114}\,t_{3.6}$ - 2	1287	126		
$C_g\,R_{60}\,f_{44}\,D_{114}\,t_{3.6}$ - 3	1275	125		

confinement present due to wrapping. However, the stiffness of both elements is the same, thus the confining effect of the FRP wrapping did not affect the element's stiffness. The strain hardening region is as apparent in the CCFST specimen as its CFST benchmark, but in the CCFST it looks like the section's capacity is still to reach the ultimate when suddenly the drop takes place. In other words, the enhanced behavior of the specimen seems to be interrupted by

the sudden load drop resulted from the explosive rupture of the wraps. Moreover, the CFST's limit stress of elasticity increases after the application of GFRP wraps because the outward buckling of the steel is delayed due to the wrapping. Two observations are to be noted concerning the post rapture region in the CCFST graph. First, the load-end displacement beyond the load drop seems fluctuating due to the multiple consecutive localized ruptures of the wrapping at different locations along the specimen's length. Second, the ductility and the load carrying capacity of the CCFST element is still higher than the CFST's even after the load drop because of the little damage to steel tube prior to FRP rapture.

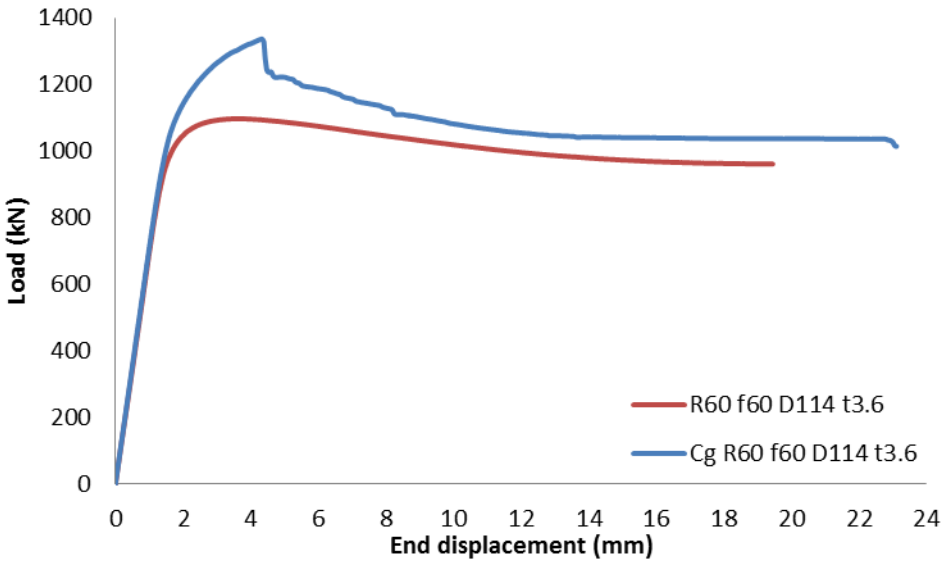

Figure 36: load-displacement diagram of a CCFST specimen and its CFST base

To quantify the strengthening effects of the confining GFRP wraps, a comparison between the CFST and its benchmark counterpart CCFST is shown in Table 19. It can be noted that the increase in the axial capacity of CFST elements with normal strength concrete infill is always greater than that with higher concrete infill compressive strength. Also, when the outer diameter is kept constant (D=114mm), the increase in the capacity is inversely proportional to the steel tube thickness which agrees with the Prichard and Perry's [24] findings that beyond

certain tube thickness, additional confinement will not result in significant increase in the CFST section's capacity. Moreover, when the tube thicknesses are almost similar (t=3.1mm and t=3.6mm), the increase in the resisted axial load decreases as the outer diameter increases because of the section's steel tendency to buckle.

Table 19: comparison between CFST and CCFST

Specimen	N_{CCFST}	N_{CFST}	$\frac{N_{CCFST}}{N_{CFST}}$
$R_{60}\, f_{60}\, D_{167}\, t_{3.1}$	2085	1952	1.07
$R_{60}\, f_{44}\, D_{167}\, t_{3.1}$	2048	1720	1.19
$R_{60}\, f_{60}\, D_{114}\, t_{3.6}$	1326	1109	1.20
$R_{60}\, f_{44}\, D_{114}\, t_{3.6}$	1268	1038	1.22
$R_{60}\, f_{60}\, D_{114}\, t_{5.6}$	1575	1395	1.13
$R_{60}\, f_{44}\, D_{114}\, t_{5.6}$	1538	1309	1.17

Figure 37 shows the load-deformation diagram of two CCFST samples with D/t ratio of 20, loading rate of 60kN/s and two different concrete infill compressive strengths. The ultimate axial capacity of the CCFST specimen increased by 2.4% when the concrete infill compressive strength increased by 36.4%. On the other hand, the strain hardening segment of the curve shortened with the increase of the concrete's f_c'. Also, Figure 37 shows no increase in the section's ductility or toughness. While in other specimens such as the ones with D/t= 32, the improvement to the ductility is noticeable (see Figure 75, Appendix B)

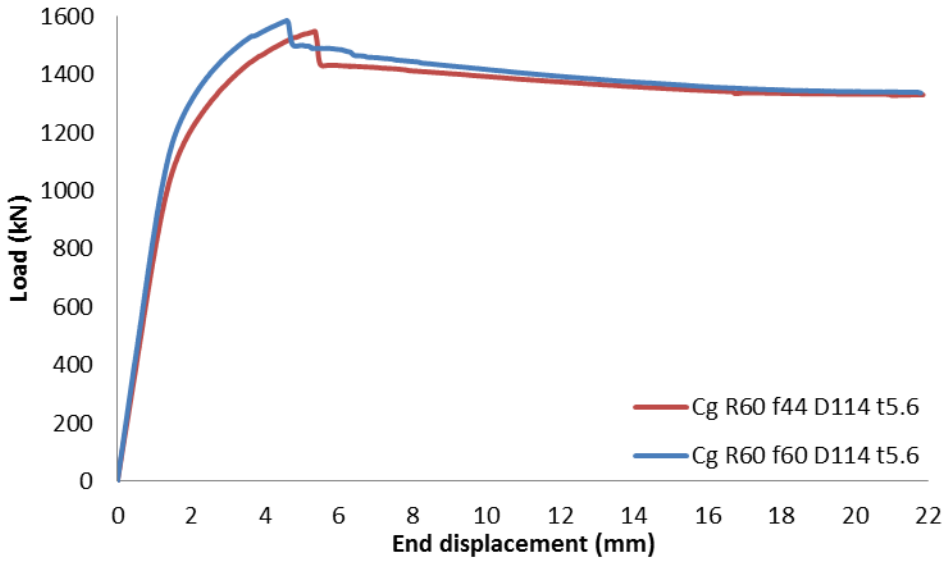

Figure 37: Load-End displacement diagram of CCFST element with D/t= 20 and different f'_c

Figure 38 shows the load-deformation diagram of three CCFST samples with loading rate of 60kN/s, concrete infill compressive strength of 60MPa and different D/t ratios. The engineering stress is expressed as of the applied load divided by the total cross sectional area of the CCFST. The ultimate axial capacity of the CCFST specimen is increasing as the D/t ratio decreases because the increase in the confining pressure as explained earlier in the CFST section. It is observed that there is a substantial improvement in the specimen's stiffness when D/t ratio is increased from 32 to 54. Meanwhile, such significant increase in the stiffness is not present when the ratio changes from 32 to 20. On the other hand, the strain-hardening segment of the curve increases as the ratio reduces. It is noticed that the strain hardening segment (measured from the end of the linear section to the load drop) in the D/t=54 curve is slightly shorter than the other specimens. The same discussion that explains the effect on the specimen's stiffness is also applicable to explain the effects on its ductility.

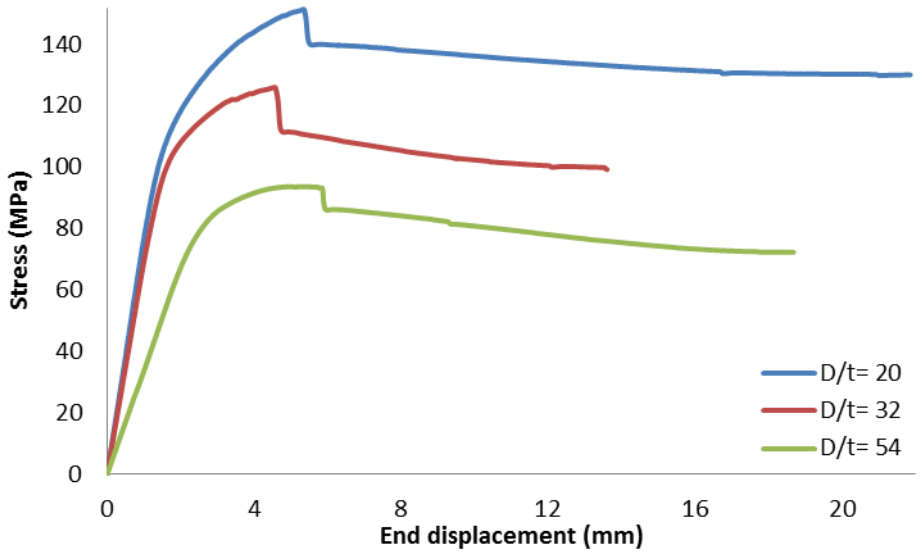

Figure 38: Load-End displacement diagram of CCFST element with different D/t ratios

Keep in mind that the change in D/t ratio from 54 to 32 is achieved by reduction of the section's outer diameter, while the change from 32 to 20 is acquired by the increase in the confining tube thickness.

In this chapter, results regarding CCFST elements with high concrete compressive strength and D/t= 54 are not reported or even used in the performed analyses. These specimens exhibited an odd behavior compared to the others. C_g R_{60} f_{60} D_{167} $t_{3.1}$ – 1 and C_g R_{60} f_{60} D_{167} $t_{3.1}$ – 3 did not fail in explosive wraps rapture or even steel tube buckling, instead the loading of the machine indicated a steady decrease in loading after reaching the maximum capacity. These two specimens are still intact subsequent to the tests; no concrete crushing at the ends or bulging of the confining steel tube. However, C_g R_{60} f_{60} D_{167} $t_{3.1}$ – 2 failed by explosive rapture near the middle segment of the samples height just as expected. Nevertheless, Figure 39 shows a very small load drop unlike the previous graphs. Note that this tiny drop occurred after the peek value while in the previous charts the drop took place in the strain hardening region of the curve.

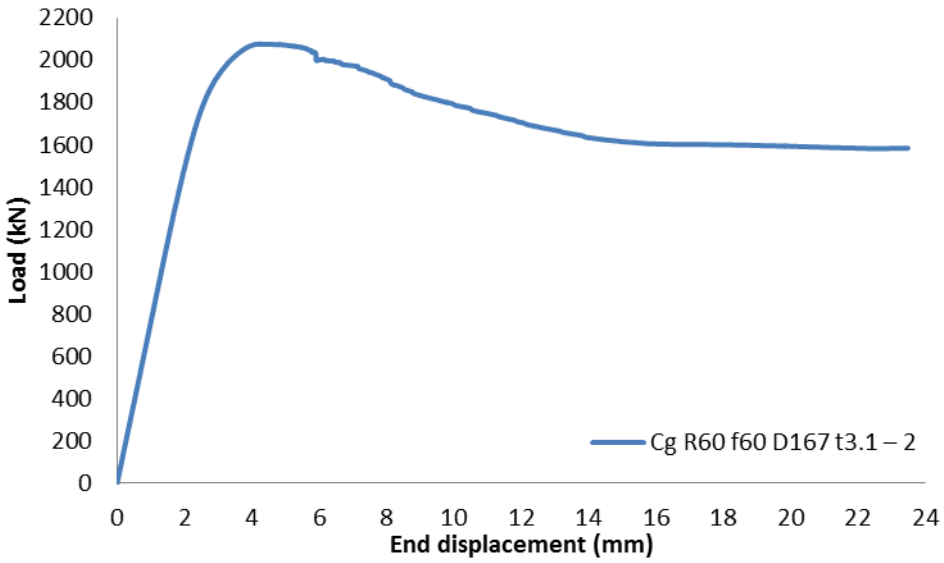

Figure 39: Load-End displacement diagram of CCFST element with $^{D}/_{t}$= 54 and f'_c=60 MPa

Chapter 4: Comparison to theory and code formulae:

Different formulae were proposed over the years to calculate the axial capacity of the CFST columns. For instance, some of them accounted for the increase in the in filled concrete strength while other just ignored it. Conceptually, the American Concrete Institute (ACI-318-11) and Australian Standard (AS 3600-2009) use the concept of reinforced concrete design in their formulation without any consideration to the concrete confinement effects [56], [57]. The American Institute of Steel Construction (AISC) formula is based on the structural steel. While the exclusively used for composite elements design, Eurocode 4 (BS EN 1994-1-2:2005) combine both these approaches [58]. This chapter illustrates the formulae proposed by some of the codes and the some well-established researches. Sample calculation for R_{60} f_{60} D_{167} $t_{3.2}$ using the each formula is presented in Appendix A.

Equations (1- 4) are used in calculating the parameters needed to predict the axial capacity of the circular CFST columns:

$$A_s = \frac{\pi}{4}\left[D^2 - (D - 2 \times t)^2\right] \quad \text{eq. (1)}$$

$$A_c = \frac{\pi}{4}(D - 2 \times t)^2 \quad \text{eq. (2)}$$

$$I_c = \frac{\pi}{64}(D - 2 \times t)^4 \quad \text{eq. (3)}$$

$$I_s = \frac{\pi}{64}\left[D^4 - (D - 2 \times t)^4\right] \quad \text{eq. (4)}$$

Where

D = the CFST section's outer diameter (mm)

t = the structural steel tube thickness (mm)

$A_s =$ area of the steel tube in the CFST section (mm^2)

$A_c =$ area of the concrete infill in the CFST section (mm^2)

$I_c =$ moment of inertia of the concrete infill in the CFST section (mm^4)

$I_s =$ moment of inertia of the steel tube in the CFST section (mm^4)

4.1 Theoretical formulae:

The theoretical formula simply combines the concrete infill capacity to the confining steel tube capacity as shown:

$$N_{the} = f_c' A_c + f_y A_s \quad \text{eq. (5)}$$

Equation (5) ignores the fact that the concrete's compression capacity increases when subjected to try-axial loading patterns. The assumption made when using this approach is that the steel tube yields at the same time at which concrete infill fails. For this research, the predicted capacities of the tested elements using the theoretical formula are shown in Table 20.

Table 20: Theoretical formula's results

f_c'	D/t	$N_{the}\ (kN)$	$N_{exp-R_{0.6}}\ (kN)$	Error (%)
60 MPa	20	1166	1365	15%
	32	975	1095	11%
	54	1777	1872	5%
44 MPa	20	1033	1314	21%
	32	831	1042	20%
	54	1452	1709	15%

4.2 American Institute of Steel Construction code formulae (AISC):

In order to determine the composite sections' nominal strength the plastic stress distribution method shall be adopted. However, for special cases such as when the cross-sectional area changes the strain compatibility method would be the better choice. Of course, local buckling should be considered for filled composite members when using this method. The AISC [8] specifies that for the plastic stress distribution method, the steel tube reaches yield f_y and the concrete infill strength is $0.95f_c'$.

AISC imposes few material limitations on the structural steel and concrete infill. These limitations shall be met, unless justified by testing or analysis:

1. For normal weight concrete, the f_c' should not be less than 21MPa and not be more than 70MPa. In this study, these limits are met since 21MPa < f_c'=44MPa, 60MPa < 70MPa.
2. The yield stress of the used structural steel in the composite member should not be more than 525MPa. This condition is satisfied in this research because f_y = 350MPa < 525MPa.

Local buckling of the CFST should be accounted for through classification of these composite members into compact, non-compact or slender. The element is considered to be compact if its D/t ratio is less than λ_p, and to be non-compact if its D/t ratio is more than λ_p but less than λ_r. Moreover, if the section's D/t ratio exceeds λ_r, then it is classified as slender. The maximum allowed D/t ratio specified in the Table 21 should not be exceeded in order for the AISC's formulae to be applicable. Table 21 shows the limits of D/t ratios for CFST members

subject to axial compression and their calculation for local buckling classification. Based on these limits, all the tested sections in this study are compact since the entire diameter to thickness ratios are less than 88.6.

Table 21: Limits of D/t ratios for CFST members for local buckling classifications

Limits	λ_p compact/non-compact	λ_r non-compact/slender	Maximum permitted
Code's expression	$\frac{0.15\,E}{f_y}$	$\frac{0.19\,E}{f_y}$	$\frac{0.31\,E}{f_y}$
Calculated values	$\frac{0.15 \times 206733}{350} = 88.6$	$\frac{0.19 \times 206733}{350} = 112$	$\frac{0.31 \times 206733}{350} = 183$

The compressive capacity of axially loaded circular concrete filled steel tubes can be determined for the limit state of flexural buckling with the following equations for compact sections:

$$P_{no} = C_2\, f_c'\, A_c + f_y\, A_s \qquad \text{eq. (6)}$$

Where

C_2 = 0.85 for rectangular sections and 0.95 for round sections

The effective stiffness of the CFST section $(EI)_{eff}$ can be calculated for all sections using this formula, (I2-12):

$$(EI)_{eff} = E_s\, I_s + C_3\, E_c\, I_c \qquad \text{eq. (7)}$$

Where

C_3 = coefficient for calculation of effective rigidity of filled composite compression member, (I2-13).

$$= 0.6 + 2\left[\frac{A_s}{A_c+A_s}\right] \leq 0.9$$

The elastic critical buckling load P_e can be calculated using Euler's formula in accordance with Chapter C or Appendix 7 of the AISC code as shown in eq. (8):

$$P_e = \frac{\pi^2 (EI)_{eff}}{(KL)^2} \qquad \text{eq. (8)}$$

Where

K = effective length factor and it is taken as 1 in this study.

L = laterally unbraced length of the member (mm)

For the axially loaded CFST columns, the design compressive strength $\Phi_c N_{AISC}$ can be calculated for the flexural buckling limit state of based on member slenderness as follows:

When $\frac{P_{no}}{P_e} \leq 2.25$

$$N_{AISC} = P_{no}\left[0.658^{\frac{P_{no}}{P_e}}\right] \qquad \text{AISC (I2-2)}$$

When $\frac{P_{no}}{P_e} > 2.25$

$$N_{AISC} = 0.877\, P_e \qquad \text{AISC (I2-3)}$$

Where:

P_{no} = Nominal compressive strength of axially loaded composite member (kN)

P_e = Elastic critical buckling load (kN)

The predicted capacities of the tested elements using the AISC formulae are shown in Table 22.

Table 22: AISC code calculation results

f_c'	D/t	L (mm)	P_{no}	C_3	I_c (mm^4)	I_s (mm^4)	$(EI)_{eff}$	P_e	N_{AISC} (kN)	$N_{exp-R_{0.6}}$ (kN)	Error (%)
60 MPa	20	250	1141	0.900	519	119	43708620	6902	1064	1365	22%
	32	250	948	0.845	560	78	35447698	5598	883	1095	19%
	54	350	1716	0.746	1269	100	59281828	4776	1477	1872	21%
44 MPa	20	250	1014	0.900	519	119	40969515	6470	950	1314	28%
	32	250	812	0.845	560	78	32673093	5160	760	1042	27%
	54	350	1408	0.746	1269	100	53728630	4329	1228	1709	28%

4.3 ACI and AS codes formulae:

Both American Concrete Institute (ACI) [56] and Australian Standards (AS) [57] adopted the same approach for predicting the composite section's squash load. Just like the theoretical approach, neither the AS code nor the ACI code considers increase in the confined concrete's axial capacity as shown:

$$N_{ACI/AS} = 0.85\, f_c'\, A_c + f_y\, A_s \qquad \text{eq. (11)}$$

however, 15% of the concrete segment is reduced to account for its uncertainties. In other words, the compression composite members are considered as regular reinforced concrete in these two codes. To account for local buckling of the structural steel tube, a limiting thickness is specified and, not to be exceeded. The magnitude of this thickness is based on the achievement of yield stress in the empty steel tube when subjected to axial monotonic loading. Moreover, this formula does not differentiate between different cross-sectional shapes. The calculated capacities of the tested elements using the ACI and AS formulae are shown in Table 23.

Table 23: ACI and AS codes calculation results

f_c'	D/t	$N_{ACI/AS}$ (kN)	$N_{exp-R_{0.6}}$ (kN)	Error (%)
60 MPa	20	1091	1365	20%
	32	894	1095	18%
	54	1594	1872	15%
44 MPa	20	978	1314	26%
	32	772	1042	26%
	54	1318	1709	23%

4.4 Giakoumelis and Lam formulae:

In their experimental study, Giakoumelis and Lam tested CFST's with different parameters [43]. Then, their results were compared with the predicted values using different codes such as the ACI and the Euro Codes. The axial capacity of all the non-greased CFST members were roughly 35% higher than that calculated from the AS and ACI codes. The differences between calculated capacities from the codes and that from the tests for high-strength concrete infill ranged from 20% to 30%. However, the deviation of the predicted from the experimental values was even higher for normal-strength concrete infill (~ 39%). Thus, it was concluded that the ACI and AS are very conservative in their estimation of axial load capacity of composite sections. Hence, the shown formula was proposed:

$$N_{Geo} = 1.3\, f_c'\, A_c + f_y\, A_s \qquad \text{eq. (12)}$$

The 0.85 coefficient is replaced by another which equals 1.3 for the ACI/AS equation to take into consideration the concrete confinement effects on enhancing the axial compressive strength of CFST. Note that this formula is derived from regression of the tested samples and it does not

consider the type of the composite section. The predicted capacities calculated using the modified ACI and AS equation are shown in Table 24.

Table 24: Giakoumelis G. and Lam D. calculation results

f_c'	D/t	N_{Geo} (kN)	$N_{exp-R_{0.6}}$ (kN)	Error (%)
60 MPa	20	1314.9	1365	4%
	32	1135.8	1095	4%
	54	2142.7	1872	14%
44 MPa	20	1142.2	1314	13%
	32	949.4	1042	9%
	54	1720.3	1709	1%

4.5 Mander, et al. formulae:

In this formulation [41], the confined concrete compressive strength f'_{cc} can be determined using a constitutive model that contains a unique ultimate strength surface for multi-axial compressive stresses. Because of its great agreement with tri-axial test data, the five-parameter failure surface described by William and Warnke (1975) is used [60]. Also, the predicted ultimate strength surface established on the tri-axial tests of Schickert and Winkler (1977) is implemented in this formula [61]. The shown formula is a variant of eq. (5) with the adjustment to account for the confinement:

$$N_{Man} = f'_{cc} A_c + f_y A_s \qquad \text{eq. (13)}$$

In the concrete filled steel tubes, the confining steel tube imposes a tri-axial compression on the concrete core with equal effective lateral confining stresses from circular hoops. The confined compressive strength is given by:

$$f'_{cc} = f'_c(-1.254 + 2.254\sqrt{1 + \frac{7.94\, f_1}{f'_c}} - 2\frac{f_1}{f'_c})$$ eq. (14)

Where

f_1 = the effective lateral confining stress on the concrete.

$$f_1 = \frac{2\ \sigma_\theta\ t}{D}$$

and $\sigma_\theta = 0.1\ f_y$

f'_c = the unconfined concrete cylinder compressive strength.

f'_{cc} = the confined concrete compressive strength.

these proposed set of formulae are applicable only to circular concrete filled steel tubes because of the hoop stress created by the confining steel. The values of the sections capacities proposed by the Mander, et al. formulation were calculated and presented in Table 25 for the specimens tested in this research.

Table 25: Mander, et al. calculation results

f'_c	D/t	$f_1\ (MPa)$	$f'_{cc}\ (MPa)$	$N_{Man}\ (kN)$	$N_{exp-R_{0.6}}\ (kN)$	Error (%)
60 MPa	20	3.4	81	1340	1365	2%
	32	2.2	74	1101	1095	1%
	54	1.3	69	1951	1872	4%
44 MPa	20	3.4	64	1200	1314	9%
	32	2.2	58	954	1042	8%
	54	1.3	52	1623	1709	5%

4.6 Eurocode 4 formulae:

There are two approaches adopted by the Eurocode 4 [58] for calculating the axial capacity of concrete filled steel tube columns, the general method and the simplified method. In the general method, the second order effects and imperfections of the compression members are taken into consideration explicitly. This method may be used for members with symmetrical sections, but they are also applicable to non-prismatic axial members. Consequently, appropriate software for numerical computation is essential for the application of the general method. In the simplified method, the European buckling curves for steel columns are utilized. The element's imperfections are implicitly taken into account. Unlike the general method, the simplified one is limited to prismatic composite axial members with symmetrical sections. Both methods are based on the following assumptions:

a) Flat sections stay flat while the column is deforming due to loading.
b) Till failure, the existence of full interaction between the concrete and steel surfaces is maintained.

In this research, only the simplified method is applied due to its applicability to the tested specimens and the calculation simplicity.

In order to account for the local buckling of the structural steel tube in the CFST columns, the slenderness of the steel section in the member must meet the following condition:

$$\frac{D}{t} \leq 90\ \varepsilon^2$$

Where

$$\varepsilon = \sqrt{\frac{235}{f_y}}, \qquad f_y \; in \; MPa$$

Also, the simplified method is subject to the following limitations:

a) For CFST columns $\bar{\lambda} \leq 2.0$, where $\bar{\lambda}$ is the relative slenderness.

b) The relative contribution of the steel section to the capacity of CFST member must be between 0.2 and 0.9; it can be calculated as follow:

$$\delta = \frac{f_y A_s}{\gamma_s} \Big/ N_{pl.Rd} \qquad \text{eq. (15)}$$

Where:

$N_{pl.Rd}$ = is the plastic resistance $= \frac{f_c'}{\gamma_c} A_c + \frac{f_y}{\gamma_{Ma}} A_s$

c) The CFST must be with ratio of cross-sectional dimensions in the range

$5.0 > \frac{h_c}{b_c} > 2.0$.

The axial capacity of the CFST a column is the aggregate of the plastic compression resistances of each of its constituent elements and can be calculated as follows:

$$N_{Euro} = \eta_a A_s \frac{f_y}{\gamma_{Ma}} + A_c \frac{f_c'}{\gamma_c} \left[1 + \eta_c \frac{t}{D} \frac{f_y}{f_c'}\right] \qquad \text{eq. (16)}$$

γ_{Ma} and γ_c are the structural steel and concrete material partial safety factors, which can be taken 1 and 1.3, respectively.

The coefficients η_a and η_c are replaced with η_{a0} and η_{c0}because of the absence of effective eccentricity of the axial compressive force $= M_{max.Sd}/N_{Sd}$, and they are calculated by:

$$\eta_{a0} = 0.25\left(3 + 2\bar{\lambda}\right) \qquad \leq 1 \qquad \text{eq. (17)}$$

$$\eta_{c0} = 4.9 - 18.5\,\bar{\lambda} + 17\,\bar{\lambda}^2 \qquad \geq 0 \qquad \text{eq. (18)}$$

Keep in mind that the imposed limits on the values of η_{a0} and η_{c0}, show the effects of eccentricity and slenderness on the CFST's capacity.

The relative slenderness $\bar{\lambda}$ of the CFST column in the plane of bending considered is given:

$$\bar{\lambda} = \sqrt{\frac{N_{pl.Rk}}{N_{cr}}} \qquad \text{eq. (19)}$$

Where:

$N_{pl.Rk}$ = is the value of the plastic resistance $N_{pl.Rd}$ calculated using material partial safety factors γ_{Ma} and γ_c set equal to 1.0

$$= f_c'\,A_c + f_y\,A_s$$

N_{cr} = is the elastic critical load of a composite column and calculated using the conventional Euler buckling equation

$$= \frac{\pi^2\,(EI)_{eff\ k}}{L_{fl}^2}$$

L_{fl} = is the buckling length of the column, taken as specimen height.

$(EI)_{eff\ k}$ = is the bending stiffness of the composite section about the buckling axis considered

$$= E_s\,I_s + K_e\,E_c\,I_c$$

K_e = a correction factor for cracking of concrete, which may be taken as 0.6

All the tested specimens in this study met the required limits by Eurocode 4. The predicted capacities calculated using the Eurocode 4 equation are shown in Table 26.

Table 26: Eurocode 4 calculation results

f_c'	D/t	L (mm)	I_c (mm^4)	I_s (mm^4)	N_{cr}	$N_{pl.Rk}$	$\bar{\lambda}$	η_{a0}	η_{c0}	N_{Euro}	$N_{exp-R_{0.6}}$ (kN)	Error (%)
60 MPa	20	250	519	119	5899	1165	0.44	0.97	0.04	1036	1365	24%
	32	250	560	78	4714	975	0.45	0.98	0.00	841	1095	23%
	54	350	1269	100	4168	1777	0.65	1.00	0.07	1503	1872	20%
44 MPa	20	250	519	119	5610	1033	0.43	0.96	0.09	935	1314	29%
	32	250	560	78	4403	831	0.43	0.97	0.07	731	1042	30%
	54	350	1269	100	3808	1452	0.62	1.00	0.00	1246	1709	27%

4.7 Comparison of calculated to experimental results:

In the previous sections of this chapter several methods for calculating the CFST axial capacity were introduced. To evaluate their predicted capacities' effectiveness, a comparison with the experimental output was performed and summarized in Figure 40 and Figure 41. The comparison shown in Figure 40 is for the specimens subjected to high loading rates during the test.

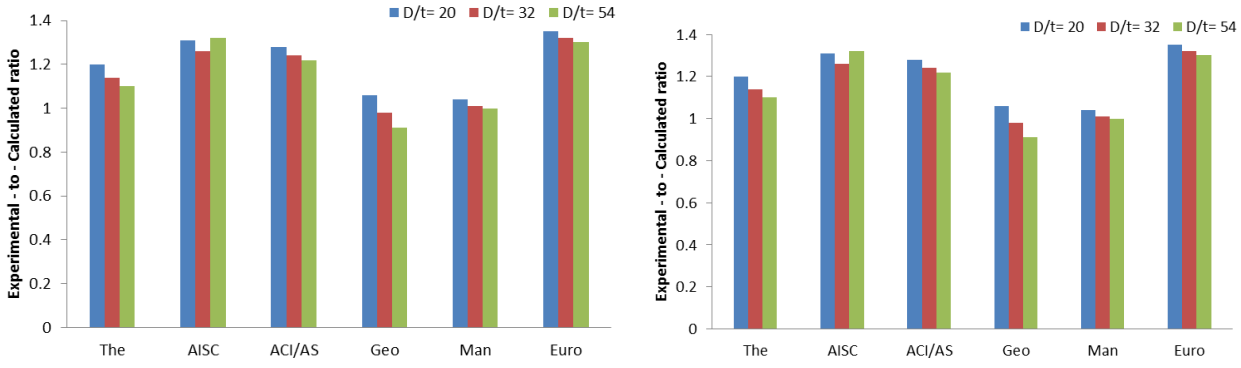

(a) $f_c' = 60$ MPa (b) $f_c' = 44$ MPa

Figure 40: Comparison of load carrying capacity of CFSTs under high loading rate with the calculated

It can be noted that the Eurocode 4, ACI, AS and the AISC codes have under estimated the axial carrying capacity of CFST columns since the factors ranges from 1.26 to 1.42. In other words, 26% to 42% of the CFST column's capacity is not used in the design of these composite columns. Also, the theoretical formula under estimated the CFST capacity but not as large as the other four codes since the ratios range from 1.10 to 1.27. On the other hand, the method proposed by Giakoumelis and Lam [43] overestimates the section's capacity in some cases and its use may result in unconservative design. The estimated compression capacity of the CFST elements using Mander, et al. formulae agreed very well with the ones obtained from this study's tested specimens.

Other than the AISC code in Figure 40, the difference between calculated capacities using the other formulae and the ones obtained from testing reduces as the $^{D}/_{t}$ ratio increases. Moreover, all the predicted values for high strength concrete are closer to the actual capacities than the normal strength ones.

The comparison shown in Figure 41 is for the specimens subjected to low loading rates during the test.

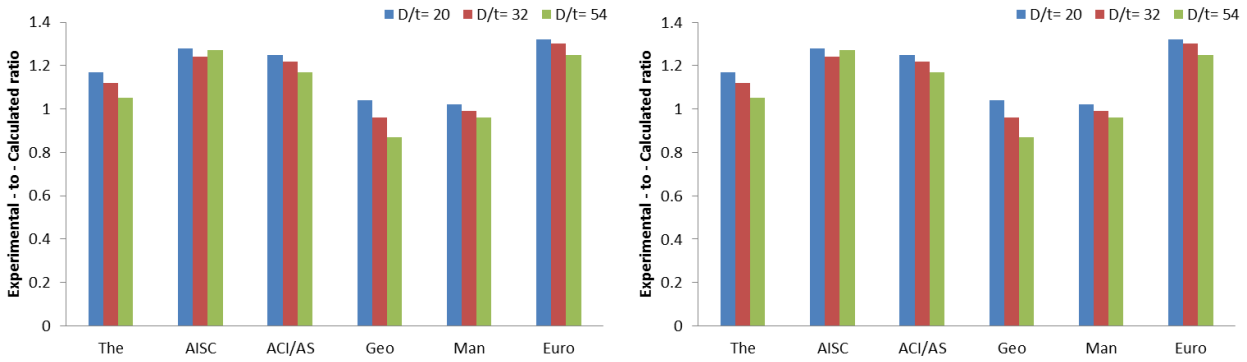

(a) $f'_c = 60$ MPa (b) $f'_c = 44$ MPa

Figure 41: Comparison of load carrying capacity of CFSTs under low loading rate with the calculated

The Eurocode 4, ACI, AS and the AISC codes have under estimated the compression capacity of CFST columns since the factors ranges from 1.17 to 1.43. Through the same logic explained earlier these codes are considered fairly conservative. Also, the theoretical formula under estimated the CFST capacity but not as large as the other four codes since the ratios range from 1.05 to 1.27. On the other hand, the method proposed by Mander, et al. and the ones by Giakoumelis and Lam overestimates the section's capacity in some cases and its use may result in unconservative designs.

Just like the high loading rate, the difference between calculated capacities using the other formulae and the ones obtained from testing reduces as the $D/_t$ ratio increases. This is true for all the methods but the AISC code. Furthermore, all the predicted values for high strength concrete are closer to the actual capacities than the normal strength ones. It can be seen that there are no big difference between the two loading rates in terms of the comparison factors.

Chapter 5: Finite Element Analysis

Finite element analysis has been used frequently in previous research to predict the behavior of CFST using available commercial finite element software like for example ANSYS [62] and ABAQUS [42]. FE modeling is usually verified with experimental results then extended to perform parametric studies to investigate the effect of several other parameters that are usually costly or not possible experimentally. In this study, a finite element model is developed to simulate the nonlinear behavior of CFST using the ABAQUS FE software. A nonlinear FE model is created to simulate the axial capacity and failure mode of one of the CFST samples used in the proposed experiments. The studied sample is CFST $R_{0.6}$ f_{60} D_{114} $t_{5.6}$ where the concrete strength is 60MPa, steel tube thickness is 5.6mm and its outer diameter is 114mm. It should be mentioned that only model verification is conducted in this study.

5.1 FE Modeling Details

5.1.1 Materials

Two main types of materials are considered in the proposed FE modeling; a nonlinear compression and tension concrete infill and elasto-plastic confining steel tube. The concrete infill is modeled using solid elements whereas the steel tube is modeled using shell elements. The loading and supporting rigid plates at the top and bottom of the sample are modeled using rigid elements. In this section the details of these definitions, their assignment and their derivations are presented.

5.1.1.1 Confined Concrete

In order to define the concrete behavior in the FE model, a stress-strain diagram for the confined concrete should be established first. The equivalent stress–strain diagram for confined concrete under compressive loading as shown in Figure 42 is used in the proposed FE model. This approach is similar to the one adopted by Ellobody and Young [42].

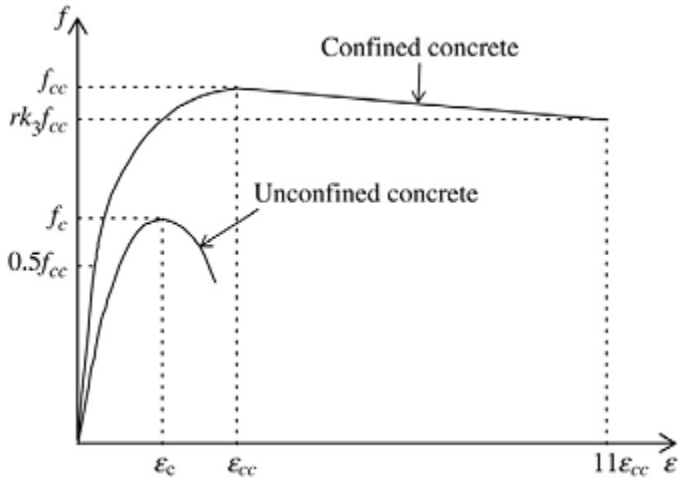

Figure 42: Equivalent compressive stress–strain diagram for unconfined and confined concrete uniaxially loaded

The material parameters shown in Figure 42 and used in defining the nonlinear compressive behavior of the concrete fill are defined as follows:

- f_c' = the unconfined concrete cylinder compressive strength.

  = 60MPa
- ε_c = 0.003, as recommended by the ACI Specification [56].
- f_{cc}' = the confined concrete compressive strength.

  = $f_c' + k_1 f_1$, as proposed by Mander, et al. [41].
- ε_{cc} = corresponding confined strain to f_{cc}'

$= \varepsilon_c \left(1 + k_2 \frac{f_1}{f_c'}\right)$, as proposed by Mander, et al. [41].

- f_1 = the lateral confining pressure from the steel tube section

  $= \frac{2\ \sigma_\theta\ t}{D}$, as proposed by Mander, et al. [41].

- $\sigma_\theta = 0.1\ f_y$, as proposed by Mander, et al. [41].

- $k_1 = 4.1$ and $k_2 = 20.5$, as proposed by Richard, et al. [24].

- $k_3 = \begin{cases} 1, & 21.7 \leq \frac{D}{t} \leq 40 \\ 0.00003391 \left(\frac{D}{t}\right)^2 - 0.010085 \left(\frac{D}{t}\right) + 1.3491, & 40 \leq \frac{D}{t} \leq 150 \end{cases}$

  as proposed by Hu, et al [26].

- $\mathrm{r} = \begin{cases} 1, & f_c' \leq 30MPa \\ \frac{(f_c' - 30)(0.5-1)}{(100-30)} + 1, & 30 < f_c' < 100\ MPa \\ 0.5, & 100 \leq f_c' MPa \end{cases}$ as proposed by Ellobody and young [42]

As shown in Figure 42, the confined concrete goes through three phases when axially loaded such that:

- First stage: $\left(0 \leq \varepsilon \leq 0.5 \frac{f_{cc}'}{\varepsilon_{cc}}\right)$

  In this phase, the confined concrete is assumed to behave linearly till it reaches the proportionality limit which is $0.5\ f_{cc}'$ as given by Hu, et al. [26]. Actually, the Young's modulus of confined concrete (E_{cc}) can be calculated using the ACI code [56] equation: $\mathrm{E_{cc}} = 4700\sqrt{\mathrm{f_{cc}'}}$ MPa. Also, the confined concrete's Poisson's ratio $(\vartheta_{cc}) = 0.2$ as proposed by Ellobody, et al. [42].

- Second stage: $\left(0.5 \frac{f_{cc}'}{\varepsilon_{cc}} \leq \varepsilon \leq \varepsilon_{cc}\right)$

This is the nonlinear phase of the curve that starts from the proportionality limit ($0.5\,f'_{cc}$) till the confined concrete strength f'_{cc}. This portion of the curve can be described by eq. (20) proposed by Desayi and Krishnan [63], where the uniaxial stress (f) and the corresponding strain (ε) are the unknowns of this equation. Actually, the equivalent uniaxial stress-strain values obtained from this equation are representations of the multidimensional stress values.

$$f = \frac{E_{cc}\,\varepsilon}{1+\left[(R+R_E-2)\left(\frac{\varepsilon}{\varepsilon_{cc}}\right)\right]-\left[(2R-1)\left(\frac{\varepsilon}{\varepsilon_{cc}}\right)^2\right]+\left[R\left(\frac{\varepsilon}{\varepsilon_{cc}}\right)^3\right]} \qquad \text{eq. (20)}$$

Where

- $R_E = \frac{\varepsilon_{cc}\,E_{cc}}{f'_{cc}}$
- $R = \frac{R_E(R_\sigma-1)}{(R_\varepsilon-1)^2} - \frac{1}{R_\varepsilon}$
- $R_\varepsilon = R_\sigma = 4,$ as proposed by Hu and Schnobrich [64].

➢ Third stage: ($\varepsilon_{cc} \le \varepsilon \le 11\varepsilon_{cc}$)

This is the descending phase of the curve that starts from the confined concrete strength f'_{cc} till the lower stress value $rk_3f'_{cc}$.

The tensile behavior of the confined concrete is assumed to be linear throughout its increasing and decreasing stages as given by the stress strain diagram shown in Figure 43. Montoya et al. [65] proposed an equation to calculate f_{ct} for unconfined concrete that can be used for confined concrete as per eq. (20).

$$f_{ct} = 0.65\,{f'_c}^{0.33} \qquad \text{eq. (21)}$$

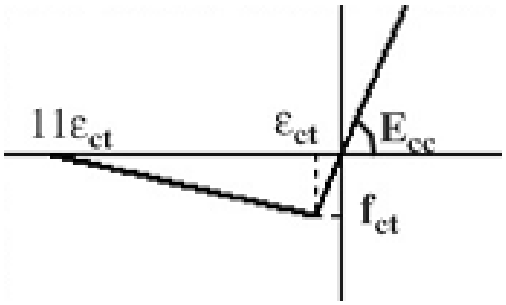

Figure 43: Equivalent tensile stress–strain diagram for confined concrete uniaxially loaded

After establishing the uniaxial stress-strain diagram for confined concrete in both compression and tension, the concrete material behavior can then be defined in ABAQUS by defining the following three main sections:

- General: In this section the concrete density is required to be defined. From the tested concrete cubes the average density of concrete was $2.45x10^{-6}\frac{Kg}{mm^3}$. Note that this section is not needed if the standard analysis is used, but for our explicit model it is essential.
- Elastic: the linear segment of the confined concrete's stress-strain curve is defined in this section. The Young's modulus of confined concrete $(E_{cc} = 42{,}304.2\ MPa)$ and the confined concrete's Poisson's ratio $(\vartheta_{cc} = 0.2)$ are defined in this part.
- Plastic: There are several material definition algorithms provided by ABAQUS for the nonlinear behavior of concrete materials. The damage Plasticity model is utilized in this study. The parameters defined in this section are shown in Table 27. A detailed description of the function of each of these parameters is defined in ABAQUS help as:

Table 27: Concrete Damage Plasticity - parameters

Dilation angle	Eccentricity	$\frac{\sigma_{b0}}{\sigma_{c0}}$	K_c	Viscosity parameter
38	1	1.12	0	0

- Dilation angle (φ): in the p–q plane. Give the value in degrees.
- Flow potential eccentricity (ϵ): The eccentricity is a small positive number that defines the rate at which the hyperbolic flow potential approaches its asymptote. If this field is left blank or a value of 0.0 is entered, the default of $\epsilon = 0.1$ is used.
- $\frac{\sigma_{b0}}{\sigma_{c0}}$: The ratio of initial equi-biaxial compressive yield stress to initial uniaxial compressive yield stress. If this field is left blank or a value of 0.0 is entered, the default of 1.16 is used.
- K_c: The ratio of the second stress invariant on the tensile meridian $(q_{(TM)})$ to that on the compressive meridian $(q_{(CM)})$ at initial yield for any given value of the pressure invariant p such that the maximum principal stress is negative, $(\hat{\sigma}_{max} < 0)$. It must satisfy the condition $0.5 < K_c \leq 1.0$. If this field is left blank or a value of 0.0 is entered, the default of $\frac{2}{3}$ is used.
- Viscosity parameter (μ): used for the visco-plastic regularization of the concrete constitutive equations in ABAQUS/Standard analyses. This parameter is ignored in ABAQUS /Explicit. The default value is 0.0.

Once the above parameters are defined, the previously calculated compressive and tensile behavior of the confined concrete is assigned. Moreover, damage parameters are also defined for the compressive and tensile strains as shown in Table 28, where the tension recovery and the compression recovery equal to 0.0 and 1.0, respectively:

Table 28: Concrete Damage Plasticity - Damage

Compression Damage		Tension Damage	
Damage	Inelastic strain	Damage	Inelastic strain
0.0000	0.0000	0.00	0.0000
0.1299	0.0004	0.31	0.0001
0.2429	0.0008	0.55	0.0003
0.3412	0.0012	0.73	0.0004
0.4267	0.0016	0.84	0.0005
0.5012	0.0020	0.91	0.0008
0.5661	0.0024	0.93	0.0010
0.7142	0.0036	0.95	0.0020
0.8243	0.0050	0.97	0.0030
0.9691	0.0100	0.99	0.0050

5.1.1.2 Steel Tube

The elasto-plastic stress-strain diagram for the steel tube is utilized to define the steel in ABAQUS. It is mandatory to define three main segments for the ABAQUS to model the steel behavior which are:

- General: In this section the steel density is necessary to be defined. From the

tested tubes the average density of steel was $7.85x10^{-6}\frac{Kg}{mm^3}$. Note that this section is not needed if the standard analysis is used, but for our explicit model it is essential.

- ❖ Elastic: The linear segment of the steel's stress-strain curve is defined in this section. The Young's modulus of steel ($E = 200{,}000\ MPa$) and its Poisson's ratio ($\vartheta = 0.3$) are defined in this part.
- ❖ Plastic: The nonlinear part of the stress-strain curve is defined in this section. Figure 44 shows the plastic part of the tested coupon steel samples where

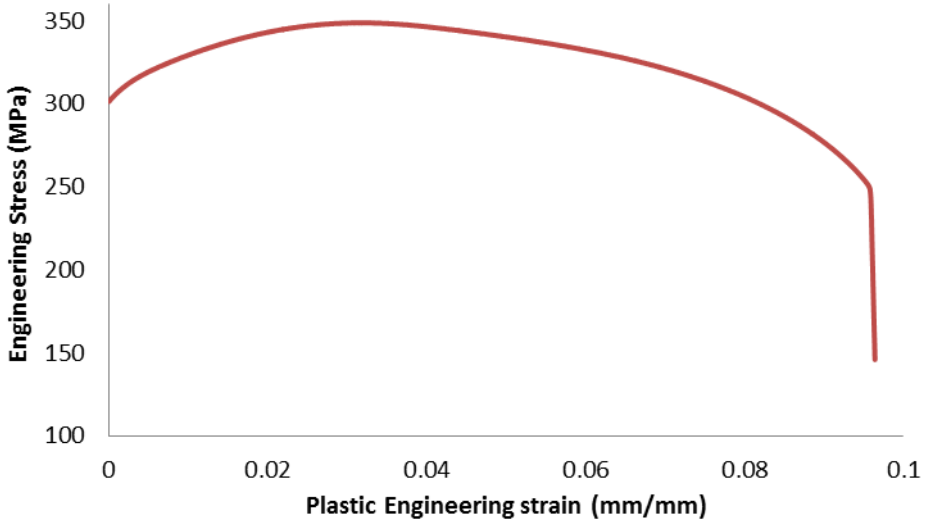

Figure 44: Engineering Stress-Plastic engineering strain of steel

the plastic engineering strain can be obtained through $\varepsilon_{pl} = \varepsilon_{total} - {}^{\sigma}/_{E}$, where the values of the stress taken after the yield point of the steel. The true stress can be calculated using: $\sigma_{true} = \sigma_{Eng}\left(1 + \varepsilon_{pl_{Eng}}\right)$, while the true plastic strain can be calculated using: $\varepsilon_{pl_{true}} = ln\left(1 + \varepsilon_{pl_{Eng}}\right)$. Keep in mind that the ABAQUS does not accept any decreasing set of

data, thus the definition of these curves end around the ultimate stress limit state. Thus, the data post ultimate true stress is discarded.

5.1.1.3 Rigid Plates

The base and loading plates are defined as rigid plates. A discrete rigid element was assigned.

5.1.2 Parts

The proposed FE model consists of four main parts; loading plate, steel tube, concrete infill and base plate. Each part is meshed separately after assigning the corresponding section in which the concrete and the two plates are solid sections while the steel is a shell-based element. Note that the mesh of the slave surface is preferred to be finer than the master one as shown in Figure 45.

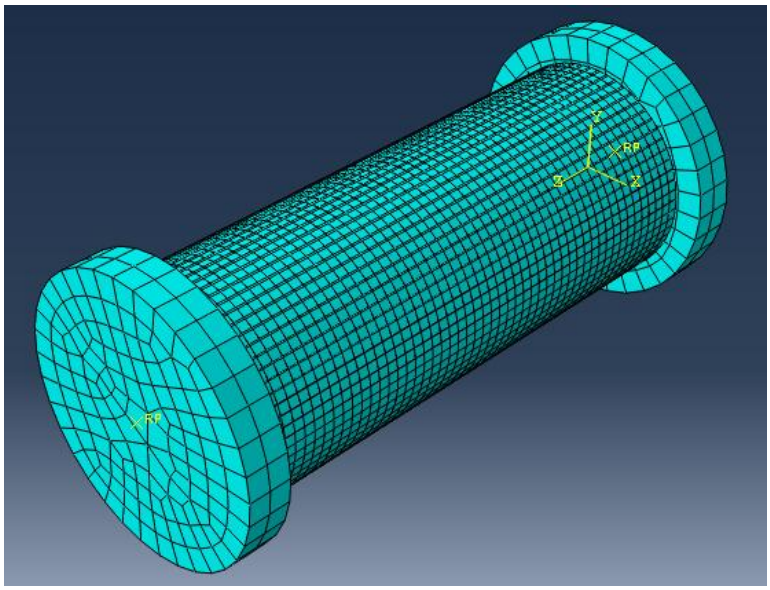

Figure 45: assembled and meshed CFST column modeled in ABAQUS

Actually, the location of each part was properly set after the assembly of all the four instances. Finally, to ease the process of any later assignment certain surfaces and set of nodes were defined in each part along with the two reference points in the loading and base plates as shown in Figure 45.

5.1.3 Interaction

Two interaction properties were defined in this model: column-plate and concrete-steel. The first is used between the concrete solid (or the steel tube) and the plates, while the second is between the concrete and the steel. Both of these properties have a tangential and normal behavior. The tangential behavior is defined as penalty with a friction coeff. =0.3 for both. Even though both properties have hard contact in their normal behavior, the separation in column-plate property is not allowed unlike the concrete-steel.

5.1.4 Boundary conditions and Loadings

A pinned-pinned supports is assumed in the proposed FE modeling using ABAQUS/Explicit time step. The specimen is loaded by applying an axial velocity of 30mm/sec at one end and over a total time step of 2 seconds to allow for a total displacement of 60mm at the specimen's ends.

5.2 FE Model Results and Verification

The results obtained from the previously described testing program are used to verify the finite elements model of this study. Three main aspects of the model's results is considered in the comparisons with the experimental results; the failure mode, axial load-shortening results, and the stress-strain diagram at the mid-height of the column.

Similar to the failure modes observed in the tested specimens, the dominant failure mode in the FE analysis of the concrete filled steel tube column is local buckling of the structural steel accompanied with crushing of concrete infill. The steel tube bulged outwards locally near the loading ends and in the mid-height of the sample as shown in Figure 46 (a). The buckling at the mid-height of the column took place at the early stage of the Dynamic/Explicit time step followed by a localized buckling near the ends of the element. A similar failure mode was observed during the actual test of the same CFST specimen as shown in Figure 46 (b).

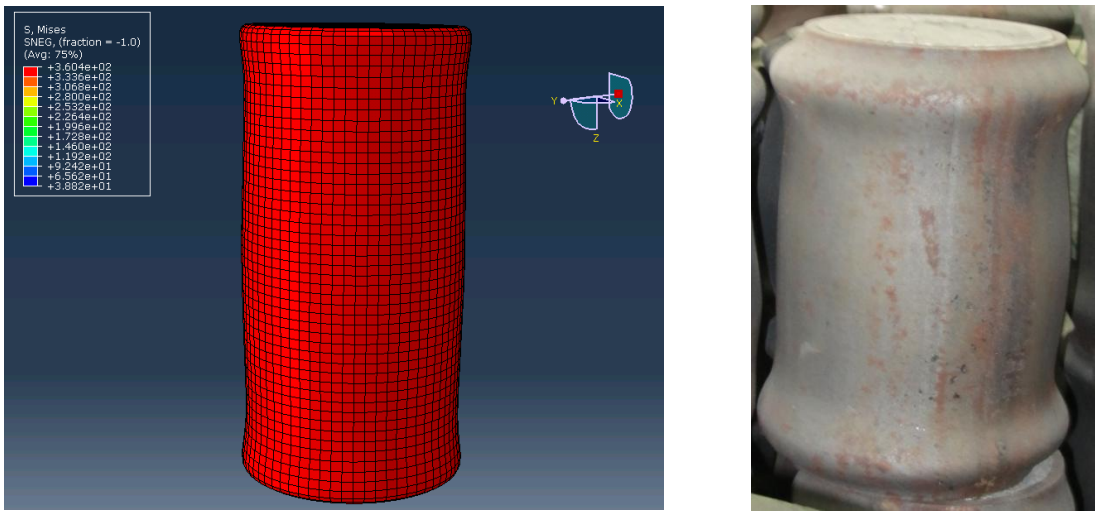

(a) FE model (b) tested specimen

Figure 46: failure mode of CFST column modeled in ABAQUS compared to tested specimen

The axial load vs. axial shortening predicted by the proposed FE model is compared with the experimental results for the same CSFT specimen as shown in Figure 47. The sample stiffness and its ultimate capacity predicted by the FE model are relatively close to the actual tested specimen. . However, the transition from the linear to plastic parts in the experimental results is gradually spread compared to the sudden change in the FE model results.

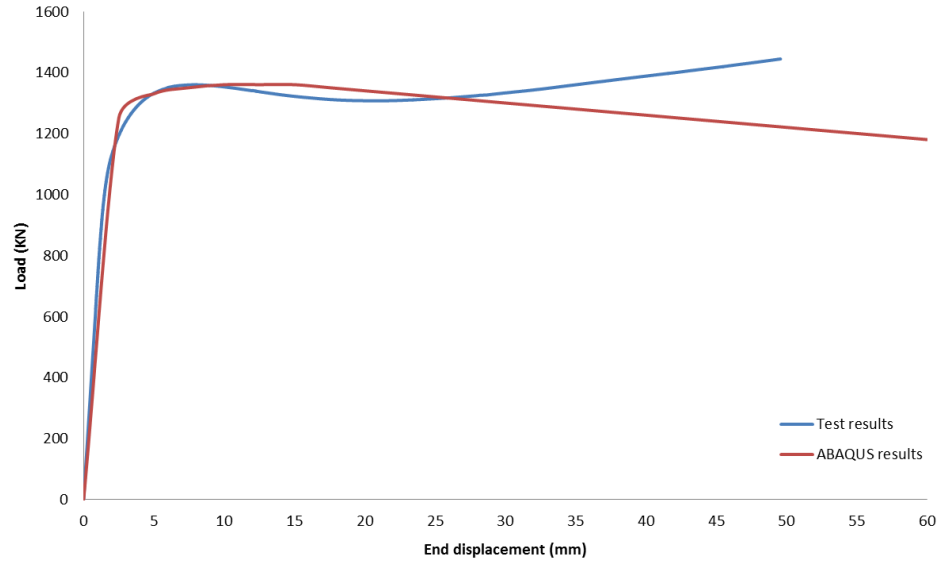

Figure 47: compression between the reaction-end displacement diagrams of the tested and modeled CFST

The axial stresses in the outer mid-height element of the FE model are plotted against their corresponding strains and compared with the experimental stress strains computed using the strain gages as shown in Figure 48. The elastic behavior of the modeled column is relatively close to the experiment despite the shift that is caused by the delays in the strain gages readings. Even though the ultimate stress of the FE data is slightly higher than that of the tested data, both of them are relatively close. Moreover, the FE model results shows early softening as compared to a constant hardening behavior observed during the experimental test.

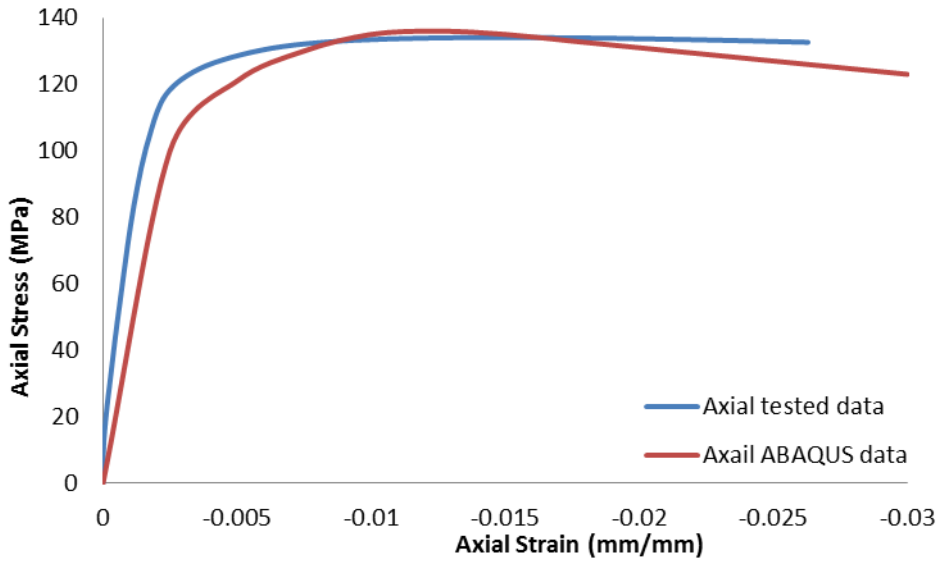

Figure 48: compression between the axial stress- axial strain diagrams of the tested and modeled CFST

As described earlier in the experimental program, a horizontal strain gage was fixed next to the vertical one in each specimen to measure the circumferential strains. The axial applied stresses at the specimens' ends vs. the measured circumferential strains at the column outer mid-height are also compared between the FE model and experiment. Figure 49 shows relatively close results in terms of the overall stress strain behavior of both the FE and experimental results. However, the stiffness of the modeled column is much smaller compared to the experimental results.

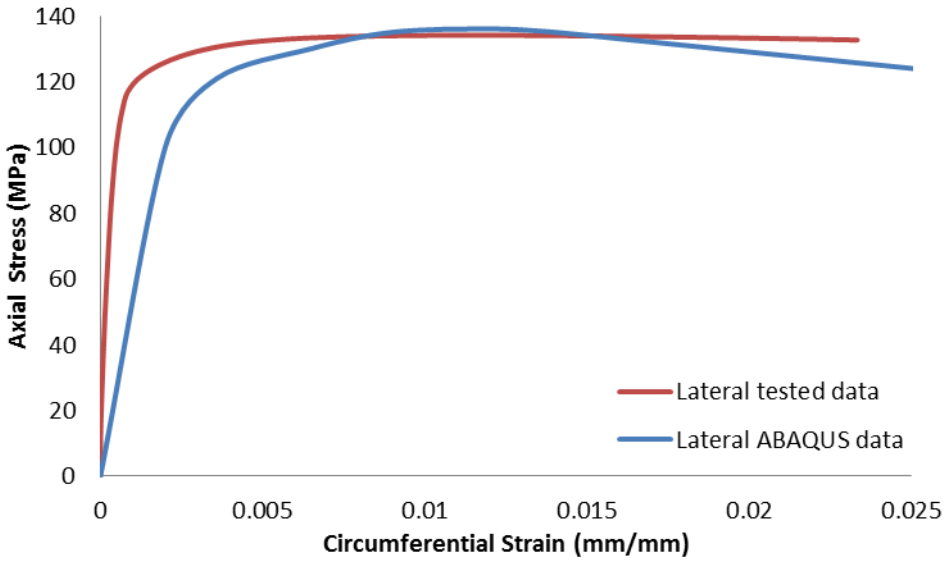

Figure 49: compression between the circumferential stress-strain diagrams of the tested and modeled CFST

Based on the above comparisons it can be concluded that the FE model is relatively verified and can be further used to conduct comprehensive parametric studies to investigate other different parameters that were not included in the proposed experiments.

Chapter 6: Summary and recommendations

6.1 Summary

In this research, the compressive behavior of the Concrete Filled Steel Tubes (CFSTs) and the Confined Concrete Filled Steel Tubes (CCFSTs) under axial compressive loads is experimentally investigated. The CCFST columns are assembled by wrapping CFST members with GFRP sheets to increase the concrete's confinement. The wrapping technique proved to be very effective in increasing the column's axial capacity as illustrated in the presented experimental results. The use of GFRP wraps increased not only the axial capacity of the CFST element but also its ductility.

For the CFST columns, the effects of three main parameters; the concrete compressive strength (f_c'), the diameter-to-thickness (D/t) ratio, and the loading rate are considered in this study. As suggested by conventional wisdom and intuition, the increase in f_c' increases the axial capacity. This increase, however, shows minimal effects on the elements stiffness. It is also noted that the column's ductility decreases as the concrete infill strength increases for higher D/t ratios, but for lower D/t ratios the opposite is true. The increase in the D/t ratio not only reduces the CFST member's stiffness but also its axial strength due to the decrease in the confinement. The increase in the applied loading rate does not seem to affect the sections stiffness, yet it slightly increases its axial strength. Actually, no significant change in the section behavior is noticed under the two different loading rates. This could be attributed to the relatively low rates necessitated by the testing machine's limitations.

Several equations and formulae are investigated to estimate the axial capacity of CFST columns. A comparison between the analytical values using some suggested equations and the presented experimental results are performed in this study. Generally, most of the methods provide conservative estimates, except for the ones proposed by Mander, et al. (1988). The deviations of the estimates from the experimental results reduce as the D/t ratio increases. Also, the estimates are closer for the specimens with higher concrete strength as compared to those having lower strength this could be attributed to the similarities in the experimental program used to develop the equations and this study. Except for Mander, et al. formula, it is found that all the other approaches can be safely used in design due to their inherent conservatism. A nonlinear finite element model using the commercial software ABAQUS is also developed in this study. The FE model is verified with one of the tested CFST samples after incorporating the material nonlinearity of both steel tube and concrete infill. Good agreement between the experimental data and the model's output in terms of the axial capacity and the stresses in the mid-height region are observed. The established FE model can be used for subsequent parametric studies.

6.2 Recommendations

The following directions could be taken to extend this research, address some of the issues encountered, and improve the quality of predictions provided by the FE model:

- Use higher specimen's length to diameter ratio, approximately 3, to further minimize the effects of the end conditions on the behavior of the element during loading.
- Strengthen the specimens' ends with steel or FRP jackets to force the failure in the mid-height region of the samples.

- Use external linear variable differential transformers (LVDT's) to capture the actual axial deflection of the tested specimens.
- Use displacement controlled loading mode for testing the samples to capture the post ultimate behavior accurately.
- Extend the finite element investigation by considering the following:
    - The effects of different Poisson's ratio for the concrete infill while loaded.
    - Higher loading rate for the applied loads.
    - Use the Drucker-Prager model to capture the behavior of concrete
- Test the CFST samples at higher loading rates to study the behavior of the element when impacted.

Bibliography

[1] J. C. McCormac, Structural Steel Design, 4th ed., m. j. horton, Ed., pearson prentice hall, 2007.

[2] R. W. Furlong, "Strength of steel encased concrete beam-columns," *American Society of Civil Engineers,* vol. 93, no. 5, p. 115–30, 1967.

[3] A. Kuranovas and Kvedaras, A. K., "Behaviour of hollow-concrete steel tubular composite elements," *Journal of Civil Engineering and Management ,* vol. II, no. 13, p. 131–141, 2007.

[4] Knowles, R. B. and Park, R., "Axial Load Design for Concrete Filled Steel Tubes," *Journal of the Structural Division, ASCE,* vol. 96, no. 10, pp. 2125-2153, 1970.

[5] Tsuji, B., Nakashima, M. and Morita, S., "Axial Compression Behavior of Concrete Filled Circular Steel Tubes," in *Third International Conference on Steel-Concrete Composite Structures*, Fukuoka, Japan, 1991.

[6] S. T. Zhong, "The Concrete Filled Steel Tubular (CFST) Structures in China," in *the Third International Conference on Steel-Concrete Composite Structures*, Fukuoka, Japan, 1991.

[7] Gourley, B. C., Tort, C., Denavit, M. D., Schiller, P. H. and Hajjar, J. F., "A SYNOPSIS OF STUDIES OF THE MONOTONIC AND CYCLIC BEHAVIOR OF CONCRETE FILLED STEEL TUBE BEAM-COLUMNS," Newmark Structural Laboratory Report Series (ISSN 1940-9826), Urbana, Illinois, 2008.

[8] AISC 360-10, Specification for Structural Steel Buildings, Chicago, Illinois: American Institute of Steel Construction, June 22, 2010.

[9] Teng, J.G. and Hu, Y. M., "Suppression of local buckling in steel tubes by FRP lacketing," in *Second International Conference on FRP Composites in Civil Engineering*, Adelaide, Australia, 2004.

[10] Shaat, A. and Fam, A., "Strengthening of short HSS steel columns using FRP sheets," in *4th International Conference on Advanced Composite Materials in Bridges and Structures*, Galgry, Alberta, Cannada, 2004.

[11] T. Nishino and Furukawa, T., "strength and deformation capacities of circular hollow section steel member reinforced with carbon fiber," in *Seventh Pacific Structural Steel conference*, Long Beach, CA, 2004.

[12] http://en.wikipedia.org/wiki/Fibre-reinforced_plas. [Online].

[13] [Online]. Available: http://www.structuremag.org/images/0108-bb-1.jpg.

[14] [Online]. Available: http://i00.i.aliimg.com/photo/v0/301278334/FRP_bars.jpg.

[15] [Online]. Available: http://ars.sciencedirect.com/content/image/1-s2.0-S0950061803000394-gr10.jpg.

[16] Teng, J. G., Chen, J. F. , Smith, S. T. and Lam, L., FRP Strengthened RC Structures, West Sussex, England: John Wiley and Sons, 2002, pp. pp. 1-10, 100-108, 148-236.

[17] Kelley, D., Graham, J. and Johnson, T., "Different FRP Resin Chemistries for Different Chemical Environments," 2010. [Online]. Available: http://www.aiche-cf.org/Clearwater/2010/Paper2/10.2.6.pdf.

[18] Erhard, G., Designing with Plastics, Munich, Germany: Hanser Grander Publcations, Inc., 2006.

[19] J. A. Pellettiere, "MATERIAL MODEL FOR BONE UNDER IMPACT LOADING," August 1998. [Online]. Available: http://www.asbweb.org/conferences/1990s/1998/280/index.html.

[20] J. S. SEWEL, "Columns for buildings," *Engineering News,* vol. 48, no. 17, p. 36–39, 1902.

[21] K. KLÖPPEL and W. GODER, "raglastversuche mit ausbetonierten Stahlrohen und Aufstellung einer Bemessungsformel," *Der Stahlbau,* vol. 26, no. 1, p. 1–10, 1957.

[22] H. R. SALANI and J. R. SIMS, "Behavior of Mortar Filled Steel Tubes in Compression," *Journal of American Concrete Institute,* vol. 61, no. 10, p. 1271–1283, 1964.

[23] P. K. Neogi, H. K. Sen and J. C. Chapman, "Concrete-filled tubular steel columns under eccentric loading," *The Structural Engineer,* vol. 47, no. 5, p. 187–95, 1969.

[24] S. J. Prichard and S. H. Perry, "The impact behaviour of sleeved concrete cylinders," *The Structural Engineer ,* vol. 68, no. 17, pp. 23-27, 2000.

[25] M. D. O'Shea and R. Q. Bridge, "Design of circular thin-walled concrete filled steel tubes," *Journal of Structural Engineering,* vol. 126, no. 11, pp. 1295-1303, November 2000.

[26] H. Hu, C. Huang, M. Wu and Y. Wu, "Nonlinear Analysis of Axially Loaded Concrete-Filled Tube Columns with Confinement Effect," *Journal of Structural Engineering,* vol. 129, no. 10, pp. 1322-1329, October 2003.

[27] S. P. Schneider, "Axially loaded concrete-filled steel tubes," *Journal of Structural Engineering,* vol. 124, no. 10, p. 1125–1138, 1998.

[28] C. S. Huang, Y. Yeh, G. Y. Liu, H. T. Hu, K. C. Tsai, Y. T. Weng, S. H. Wang and M. H. Wu, "Axial load behavior of stiffened concrete-filled steel columns," *Journal of Structural Engineering,* vol. 128, no. 9, p. 1222–1230, 2002.

[29] J. H. Shan, R. Chen, W. X. Zhang, Y. Xiao, W. J. Yi and F. Y. Lu, "Behavior of Concrete Filled Tubes and Confined Concrete Filled Tubes under High Speed Impact," *Advances in Structural Engineering,* vol. 10, no. 2, pp. 209-218, 2007.

[30] Y. Xiao, W. H. He and K. G. Choi, "Confined concrete filled tubular columns," *ASCE Journal of Structural Engineering,* vol. 131, no. 3, p. 488–497, 2005.

[31] D. Lam and L. Gardner, "Structural design of stainless steel concrete filled columns," *Journal of Constructional Steel Research,* vol. 64, p. 1275–1282, 2008.

[32] Y. Xiao, J. Shan, Q. Zheng, B. Chen and Y. Shen, "Experimental Studies on Concrete Filled Steel Tubes under High Strain Rate Loading," *ASCE Journal of Material in Civil Enginerring,* vol. 21, no. 10, pp. 569-577, October 2009.

[33] J. Huo, Q. Zheng, B. Chen and Y. Xiao, "Tests on impact behaviour of micro-concrete-filled steel tubes at elevated temperatures up to 400 C," *RILEM Materials and Structure,* vol. 42, p. 1325–1334, 2009.

[34] Yu, Z., Ding, F. and Cai, C. S. , "Experimental behavior of circular concrete-filled steel tube stub columns," *Journal of Constructional Steel Research,* no. 63, p. 165–174, 2006.

[35] Liang, Q. Q., Uy, B. and Liew, R., "Strength of Concrete-Filled Steel Box Columns with Local Buckling Effects," in *Australian Structural Engineering Conference*, Newcastle, Australia, 2005.

[36] Tomii, M., Yoshimura, K. and Morishita, Y., "Experimental studies on concrete filled steel tubular stub columns under concentric loading," in *International Colloquium on Stability*, Washington, D.C, 1977.

[37] Ramberg, W. and Osgood, W. R., "Description of stress-strain curves by three parameters," Description of stress-strain curves by three parameters, washington, 1943.

[38] Sakino, K., Nakahara, H., Morino, S. and Nishiyama, I., "Behavior of Centrally Loaded Concrete-Filled Steel-Tube Short Columns," *JOURNAL OF STRUCTURAL ENGINEERING,* vol. 2, no. 130, pp. 180-188, FEBRUARY 2004.

[39] Blanks, R. F. and McNamara, C. C., "Mass concrete tests in large cylinders," *ACI,* no. 31, p. 280–303, 1935.

[40] Gupta, P. K., Sarda, S. M. and Kumar, M. S., "Experimental and computational study of concrete filled steel tubular columns under axial loads," *Journal of Constructional Steel Research,* no. 63, p. 182–193, 2007.

[41] Mander, J. B., Priestley, M. J. N. and Park, R., "Theoretical stress–strain model for confined concrete," *Journal of Structural Engineering,* vol. 8, no. 114, pp. 1804-1826, 1988.

[42] Ellobody, E., Young, B. and Lam, D., "Behaviour of normal and high strength concrete-filled compact steel tube circular stub columns," *Journal of Constructional Steel Research,* no. 62, p. 706–715, 2006.

[43] Giakoumelis, G. and Lam, D., "Axial capacity of circular concrete-filled tube columns," *Journal of Constructional Steel Research,* vol. 7, no. 60, p. 1049–1068, 2004.

[44] Liang, Q. Q. and Fragomeni, S., "Nonlinear analysis of circular concrete-filled steel tubular short columns under axial loading," *JournalofConstructionalSteelResearch,* no. 65, pp. 2186-2196, 2009.

[45] Tang, J., Hino, S., Kuroda, I. and Ohta, T., "Modeling of stress-strain relationships for steel and concrete in concrete filled circular steel tubular columns.," *Steel ConstructionEngineering,* vol. 3, no. 11, pp. 35-46, 1996.

[46] Liang, Q. Q., "Performance-based analysis of concrete-filled steel tubular beam-columns. Part I:Theory and algorithms," *Journal of Constructional Steel Research,* vol. 2, no. 65, pp. 363-373, 2009.

[47] Kuranovas, A., Goode, D., Kvedaras, A. K. and Zhong, S., "LOAD-BEARING CAPACITY OF CONCRETE-FILLED STEEL COLUMNS," *JOURNAL OF CIVIL ENGINEERING AND MANAGEMENT ,* vol. 1, no. 5, p. 21–33, 2009.

[48] Zhong, S. and Zhang, S. M., "Application and development of concrete-filled steel tubes (CFST) in high-rise buildings," *Advances in Structural Engineering,* vol. 2, no. 2, p. 149–159, 1999.

[49] Lan, L. I. U. and Yiyan, L. U., "Axial Bearing Capacity of Short FRP Confined Concrete-filled Steel Tubular Columns," *Jurnal of Wuhan University of Technology-Mater.,* vol. 25, no. 3, pp. 454-458, 2010.

[50] Hu, Y. M. , Yu, T. and Teng, J. G., "FRP-Confined Circular Concrete-Filled Thin Steel Tubes under Axial Compression," *JOURNAL OF COMPOSITES FOR CONSTRUCTION,* vol. 5, no. 5, pp. 850-860, 2011.

[51] [Online]. Available: http://www.mtschina.com/sans01.asp?articleid=103&classid=24.

[52] [Online]. Available: http://forum.luyenkim.org/Thread-universal-testing-machine-instron-5582-67.html.

[53] [Online]. Available: http://www.showa-sokki.co.jp/english/products_e/Strain_Gage_e/strain_gage_standard_e.html.

[54] http://buildingresearch.com.np/services/mt/mt1.php. [Online].

[55] British Standards Institution, Draft for Development. DD ENV 206:1992. Concrete. Performance, production, placing and compliance criteria, London.

[56] ACI., Building code requirements for structural concrete and commentary. ACI, USA: American Concrete Institute, 2011.

[57] Standards Australia, Australian Standard, AS3600-2009 Concrete Structures, Sydney, 2009.

[58] E. 1994-1-1, Eurocode 4: Design of composite steel and concrete structures, Part 1-1 : General rules and rules for buildings, CEN, 2005.

[59] William, K. J. and Warnke, E. P., "Constitutive model for the triaxial behavior of concrete," in *International Association for Bridge and Structural Engineering*, 1975.

[60] Schickert, G. and Winkler, H. , "Results of tests concerning strength and strain of concrete subjected to multiaxial compressive stresses," *Deutscher Ausschuss fur Stahlbeton, Heft 277,* 1979.

[61] Sundarraja M. C. and Prabhu G. G., "Finite element modelling of CFRP jacketed CFST members under flexural loading," *Thin-Walled Structures,* vol. 49, p. 1483–1491, 2011.

[62] Desayi, P. and Krishnan, S., Discussion of 'Equation for the stress–strain curve of concrete', vol. 61, ACI Journal, 1964, p. 1229–1235.

[63] Hu H. T. and Schnobrich W. C., Constitutive modeling of concrete by using nonassociated plasticity, Journal of Materials in Civil Engineering, 1989, p. 199–216.

[64] Montoya E., Vecchio F. and Sheikh S., "Compression field modeling of confined concrete: constitutive models," *Journal of Materials in Civil Engineering,* no. 18, pp. 510-517, 2006.

Appendix

The Appendix has two sections: Appendix A and Appendix B. A sample calculation of each of the presented formulae in Chapter 4: Comparison to theory and code formulae: is illustrated in Appendix A. Also, Appendix B contains additional figures which are referred to in the body of the research.

Appendix A

❖ Sample calculation for R_{60} f_{60} D_{167} $t_{3.2}$ using the theoretical formula is shown below:

$$A_s = \frac{\pi}{4}\left[D^2 - (D - 2 \times t)^2\right]$$

$$= \frac{\pi}{4}\left[167^2 - (167 - 2 \times 3.1)^2\right]$$

$$= 1596\ mm^2$$

$$A_c = \frac{\pi}{4}(D - 2 \times t)^2$$

$$= \frac{\pi}{4}(167 - 2 \times 3.1)^2$$

$$= 20308\ mm^2$$

$$N_{the} = f_c'\ A_c + f_y\ A_s$$

$$= \frac{60 \times 20308 + 350 \times 1596}{1000}$$

$$= 1777\ kN$$

❖ Sample calculation for R_{60} f_{60} D_{167} $t_{3.2}$ using the AISC formula is shown below (repeated values are taken from previous examples):

$$P_{no} = 0.95\, f_c'\, A_c + f_y\, A_s$$

$$= \frac{0.95 \times 60 \times 20308 + 350 \times 1596}{1000}$$

$$= 1716\ kN$$

$$C_3 = 0.6 + 2\left[\frac{A_s}{A_c + A_s}\right]$$

$$= 0.6 + 2\left[\frac{1596}{20308 + 1596}\right]$$

$$= 0.746 \quad \leq 0.9 \qquad ok$$

$$I_c = \frac{\pi}{64}\,(D - 2 \times t)^4$$

$$= \frac{\pi}{64}\,(176 - 2 \times 3.1)^4$$

$$= 1269\ mm^4$$

$$I_s = \frac{\pi}{64}\,[D^4 - (D - 2 \times t)^4]$$

$$= \frac{\pi}{64}\,[167^4 - (167 - 2 \times 3.1)^4]$$

$$= 100\ mm^4$$

$$(EI)_{eff} = E_s\, I_s + C_3\, E_c\, I_c$$

$$= 206733 \times 100 + 0.746 \times 40841 \times 1269$$

$$= 59281828$$

$$P_e = \frac{\pi^2 (EI)_{eff}}{(KL)^2}$$

$$= \frac{\pi^2 \times 59281828}{350^2}$$

$$= 4776 \text{ kN}$$

$$\frac{P_{no}}{P_e} = \frac{1716}{4776}$$

$$= 0.3593 \quad \leq 2.25$$

$$N_{AISC} = P_{no} \left[0.658^{\frac{P_{no}}{P_e}}\right]$$

$$= 1716 \, [0.658^{0.3593}]$$

$$= 1477 \, kN$$

❖ Sample calculation for R_{60} f_{60} D_{167} $t_{3.2}$ using the ACI and AS formula is shown below (repeated values are taken from previous examples):

$$N_{ACI/AS} = 0.85 \, f_c' \, A_c + f_y \, A_s$$

$$= \frac{0.85 \times 60 \times 20308 + 350 \times 1596}{1000}$$

$$= 1594 \, kN$$

❖ Sample calculation for R_{60} f_{60} D_{167} $t_{3.2}$ using the Giakoumelis G. and Lam D. formula is shown below (repeated values are taken from previous examples):

$$N_{Geo} = 1.3\, f_c'\, A_c + f_y\, A_s$$

$$= \frac{1.3 \times 60 \times 20308 + 350 \times 1596}{1000}$$

$$= 2143\ kN$$

❖ Sample calculation for R_{60} f_{60} D_{167} $t_{3.2}$ using the Mander, et al. formula is shown below (repeated values are taken from previous examples):

$$\sigma_\theta = 0.1\, f_y$$

$$= 0.1 \times 350$$

$$= 35\ MPa$$

$$f_1 = \frac{2\ \sigma_\theta\ t}{D}$$

$$= \frac{2 \times 35 \times 3.1}{167}$$

$$= 1.3$$

$$f_{cc}' = f_c'\left(-1.254 + 2.254\sqrt{1 + \frac{7.94\, f_1}{f_c'}} - 2\frac{f_1}{f_c'}\right)$$

$$= 60\left(-1.254 + 2.254\sqrt{1 + \frac{7.94 \times 1.3}{60}} - 2\frac{1.3}{60}\right)$$

$= 69\ MPa$

$$N_{Man} = f'_{cc}\ A_c + f_y\ A_s$$

$$= \frac{69 \times 20308 + 350 \times 1596}{1000}$$

$$= 1951\ kN$$

❖ Sample calculation for R_{60} f_{60} D_{167} $t_{3.2}$ using the Eurocode 4 formula is shown below (repeated values are taken from previous examples):

$$(EI)_{eff\ k} = E_s\ I_s + K_e\ E_c\ I_c$$

$$= 206733 \times 100 + 0.6 \times 40841 \times 1269$$

$$= 51726721$$

$$N_{cr} = \frac{\pi^2\ (EI)_{eff}}{L_{fl}^2}$$

$$= \frac{\pi^2 \times 51726721}{350^2}$$

$= 4168$ kN

$$N_{pl.Rk} = f'_c\ A_c + f_y\ A_s$$

$$= \frac{60 \times 20308 + 350 \times 1596}{1000}$$

$$= 1777\ kN$$

$$\bar{\lambda} = \sqrt{\frac{N_{pl.Rk}}{N_{cr}}}$$

$$= \sqrt{\frac{1777}{4168}}$$

$$= 0.65$$

$$\eta_{a0} = 0.25\left(3 + 2\bar{\lambda}\right)$$

$$= 0.25\,(3 + 2 \times 0.65)$$

$$= 1.0765 \qquad > 1 \qquad \text{use} \quad \eta_{a0} = 1$$

$$\eta_{c0} = 4.9 - 18.5\,\bar{\lambda} + 17\,\bar{\lambda}^2$$

$$= 4.9 - 18.5 \times 0.65 + 17 \times 0.65^2$$

$$= 0.0685 \qquad \geq 0 \quad \text{ok}$$

$$N_{Euro} = \eta_a\, A_s\, \frac{f_y}{\gamma_{Ma}} + A_c \frac{f_c'}{\gamma_c}\left[1 + \eta_c \frac{t}{D}\,\frac{f_y}{f_c'}\right]$$

$$= 1 \times 1596 \times \frac{350}{1.1} + 20308 \times \frac{60}{1.3}\left[1 + 0.0685 \times \frac{3.1}{167}\,\frac{350}{60}\right]$$

$$= 1503 \text{ kN}$$

Appendix B

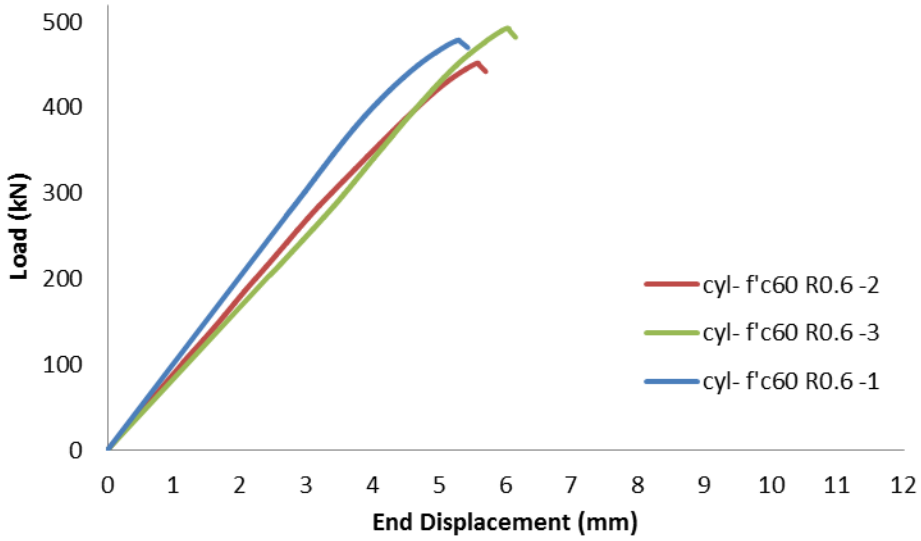

Figure 50: Stress-End displacement diagram of high strength concrete cylinder under loading rate of 0.6kN/s

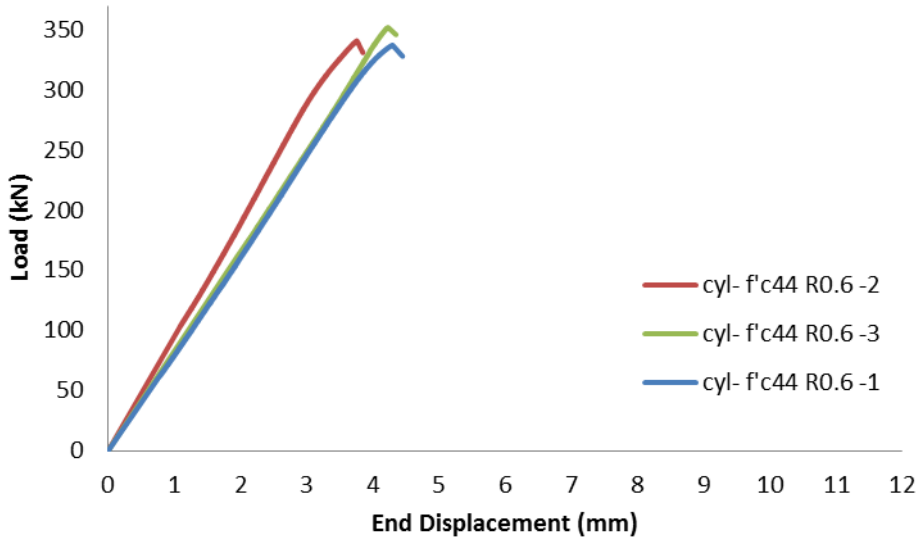

Figure 51: Stress-End displacement diagram of normal strength concrete cylinder under loading rate of 0.6kN/s

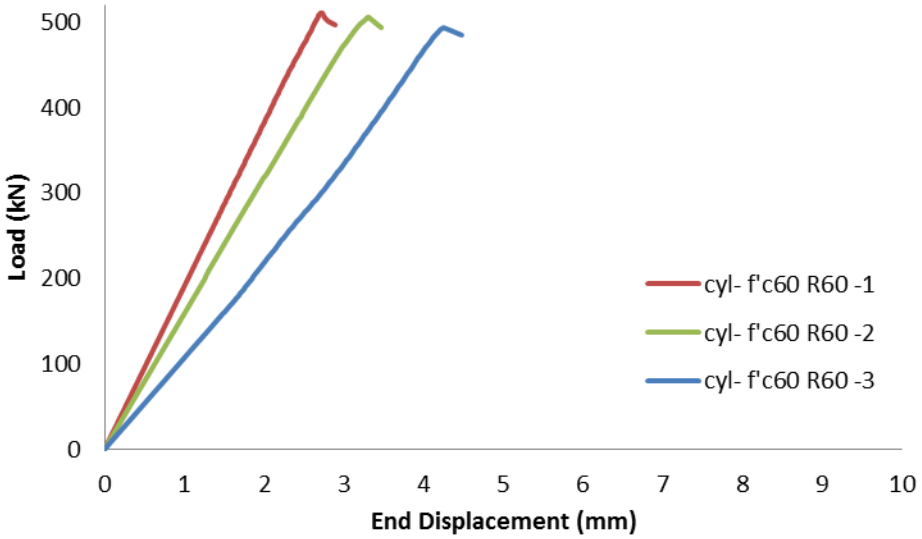

Figure 52: Stress-End displacement diagram of high strength concrete cylinder under loading rate of 60kN/s

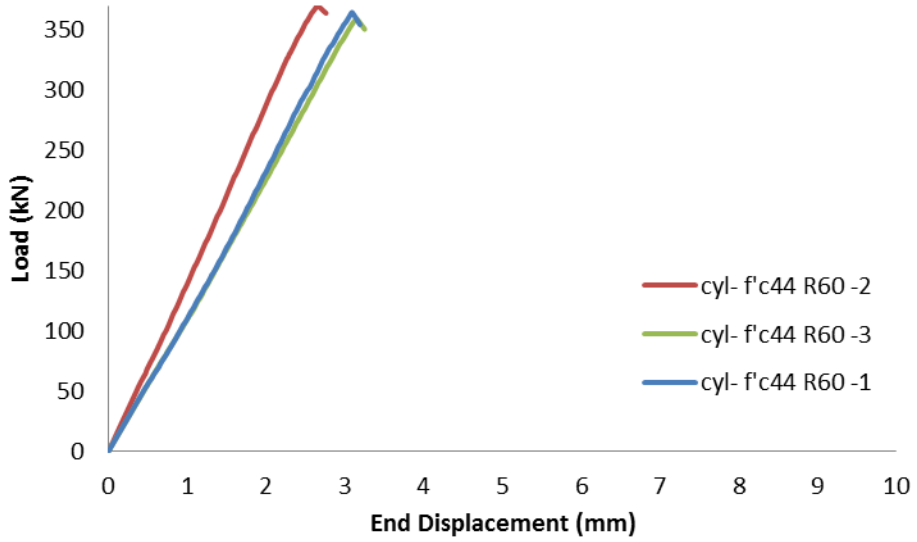

Figure 53: Stress-End displacement diagram of normal strength concrete cylinder under loading rate of 60kN/s

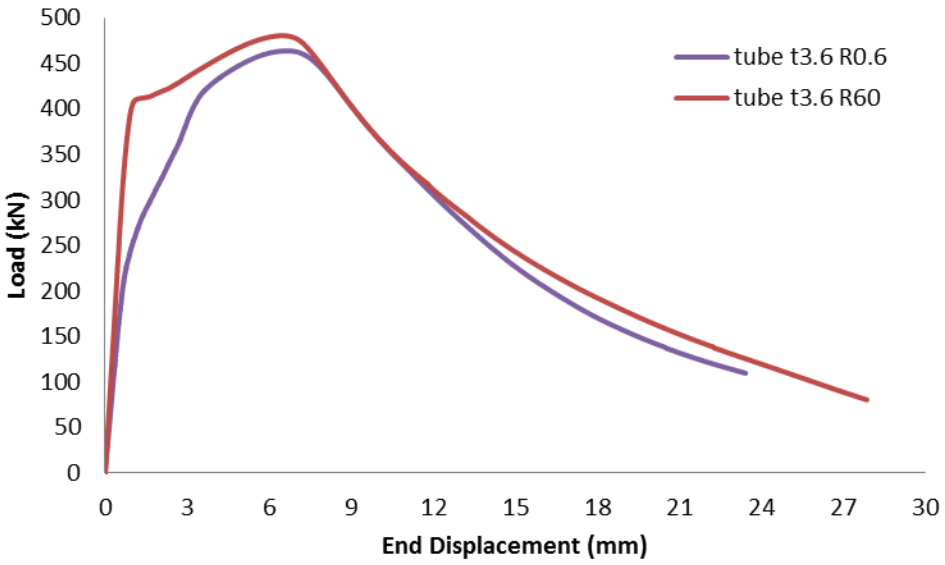

Figure 54: Stress-End displacement diagram of empty steel tube under different loading rates & t=3.6

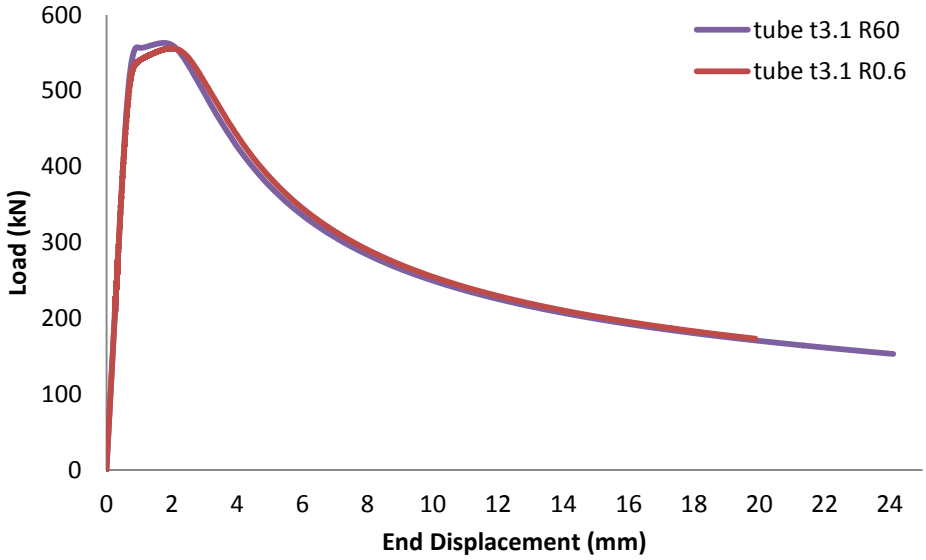

Figure 55: Stress-End displacement diagram of empty steel tube under different loading rates & t=3.1

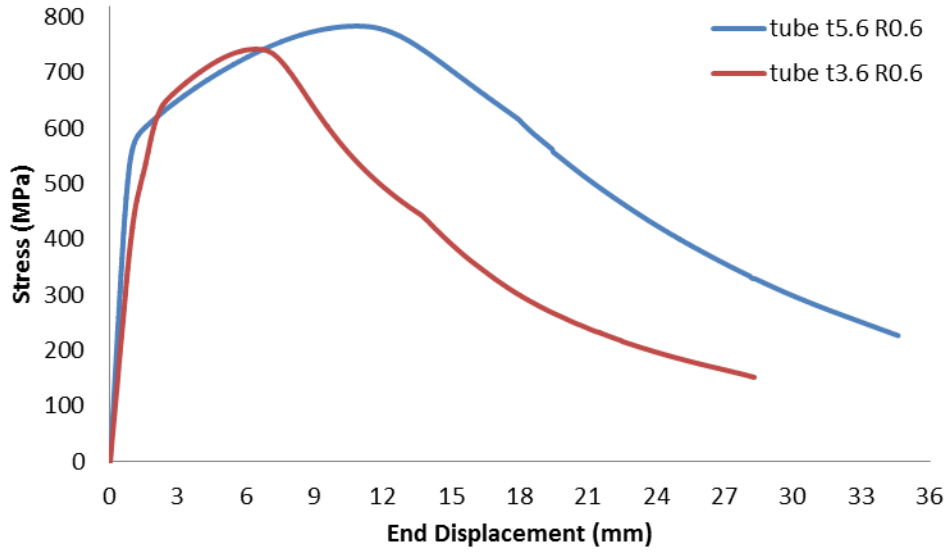

Figure 56: Stress-End displacement diagram of empty steel tube with different thicknesses & Rate=0.6kN/s

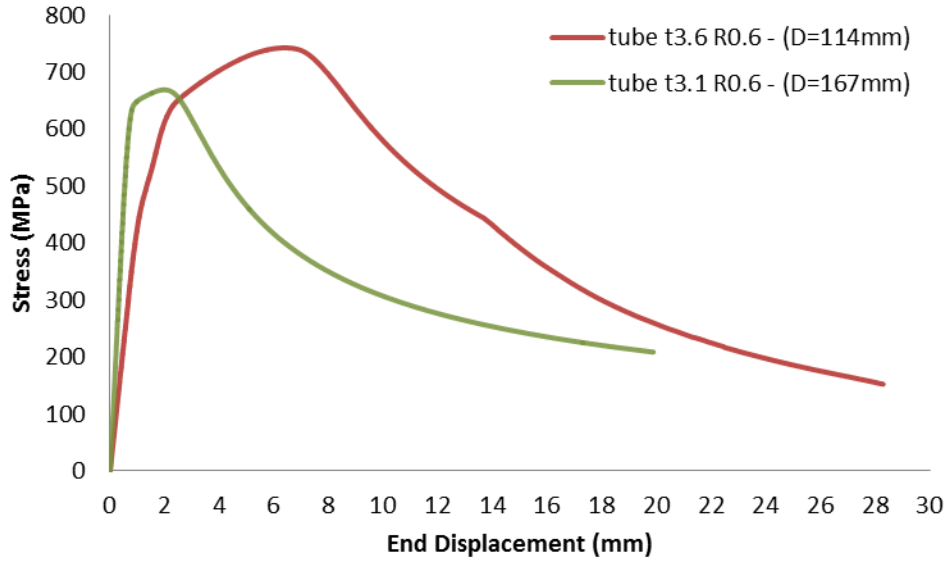

Figure 57: Stress-End displacement diagram of empty steel tube with different outer diameters & Rate =0.6kN/s

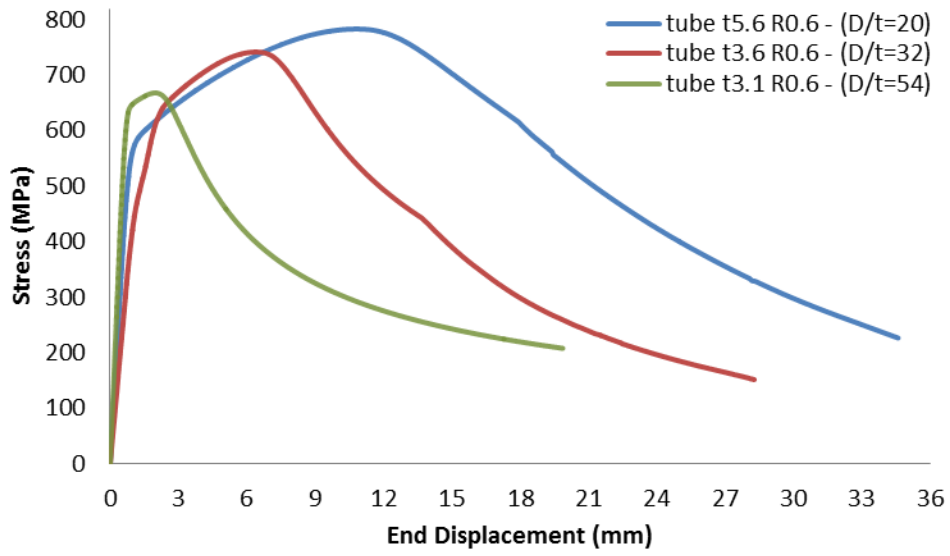

Figure 58: Stress-End displacement diagram of empty steel tube with different $^{D}/_{t}$ ratios & Rate=0.6kN/s

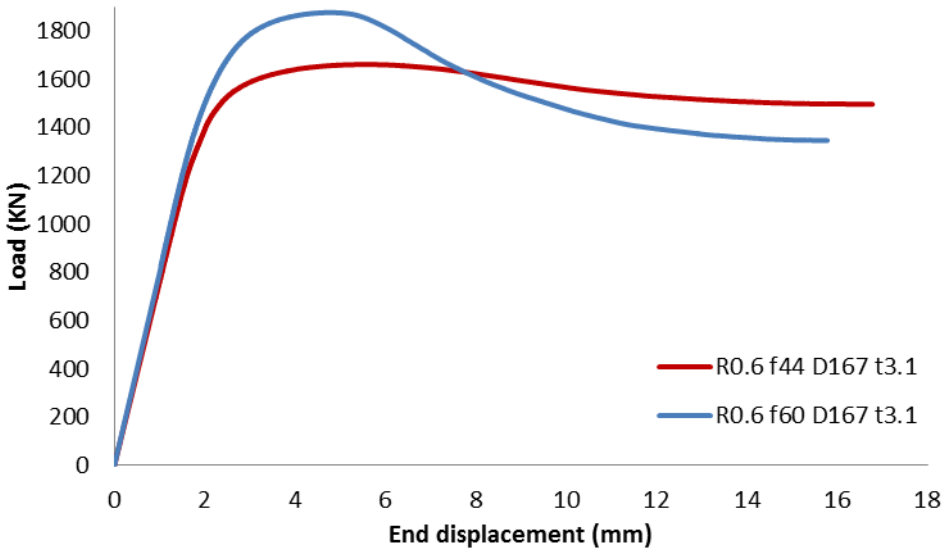

Figure 59: Load-End displacement diagram of CFST element with $^{D}/_{t}$= 54 and different f_c'

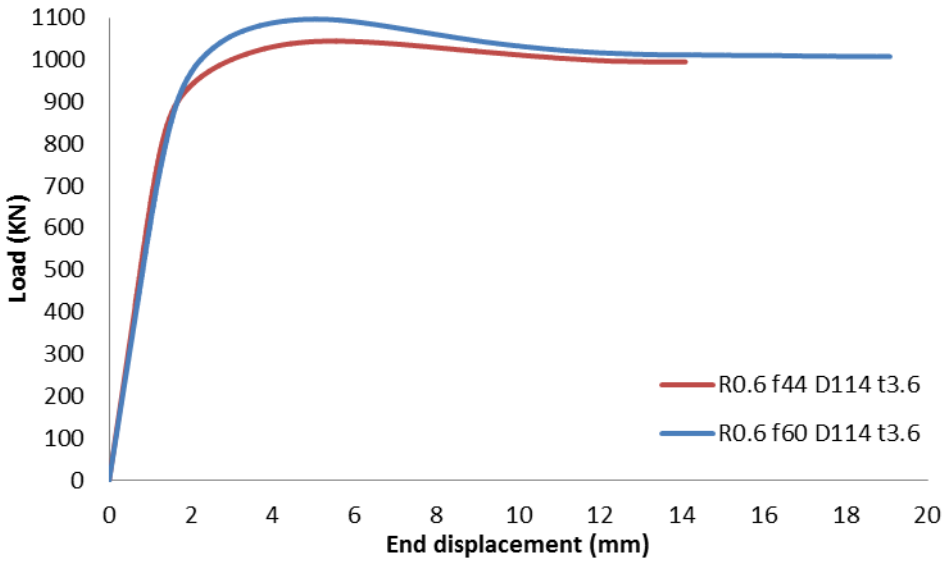

Figure 60: Load-End displacement diagram of CFST element with $^{D}/_{t}$= 32 and different f_c'

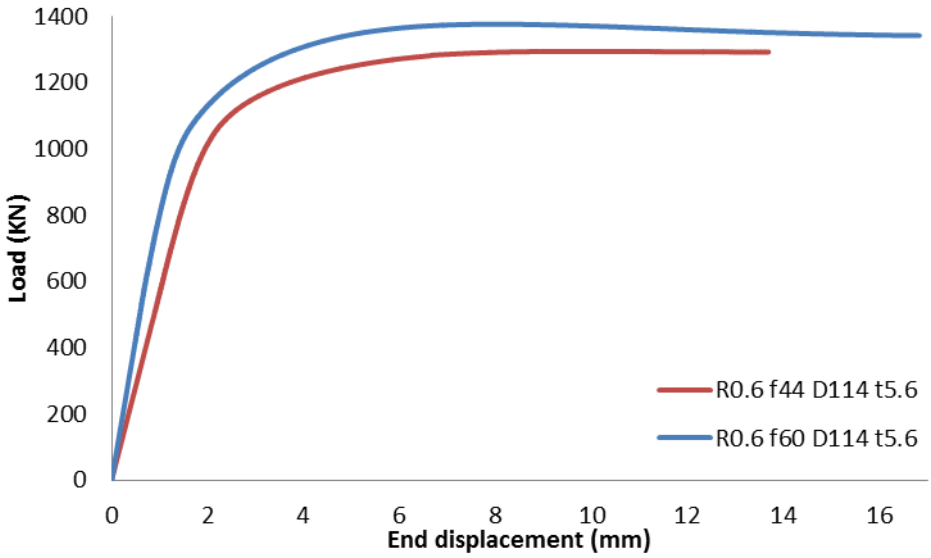

Figure 61: Load-End displacement diagram of CFST element with $^{D}/_{t}$= 20 and different f_c'

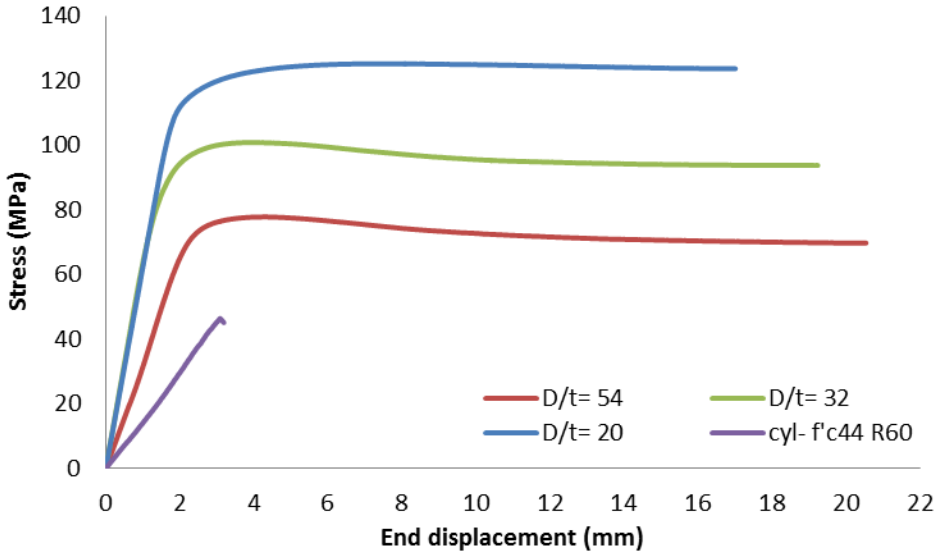

Figure 62: Stress-End displacement diagram of CFST element with loading rates= 60kN/s, f'_c= 44MPa and different $^{D}/_{t}$

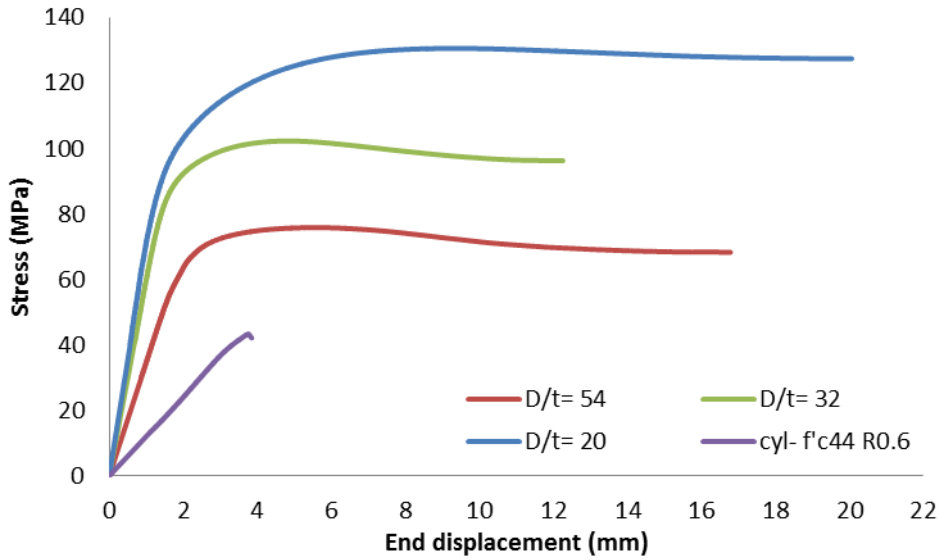

Figure 63: Stress-End displacement diagram of CFST element with loading rates= 0.6kN/s, f'_c= 44MPa and different $^{D}/_{t}$

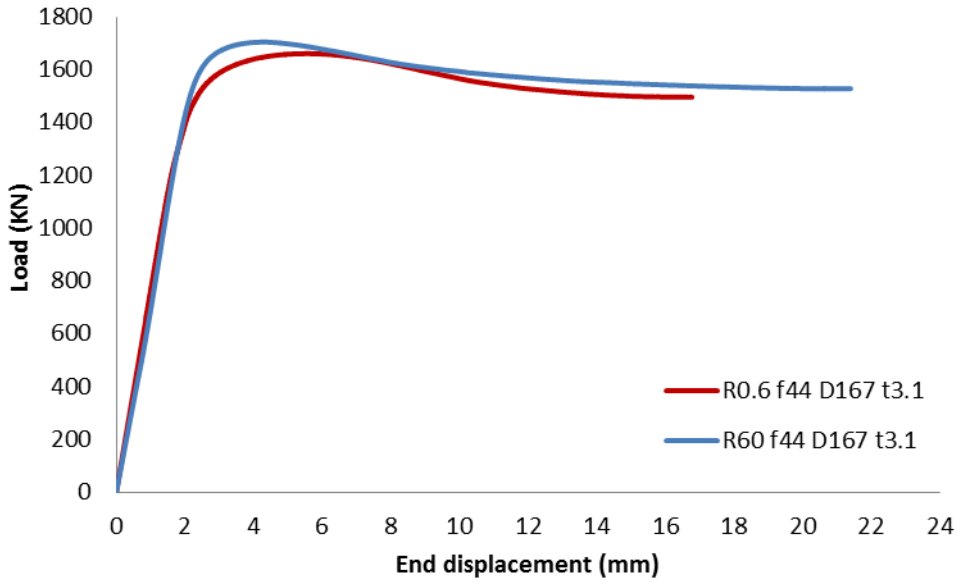

Figure 64: Load-End displacement diagram of CFST element with $^{D}/_{t}$= 54 and different loading rates

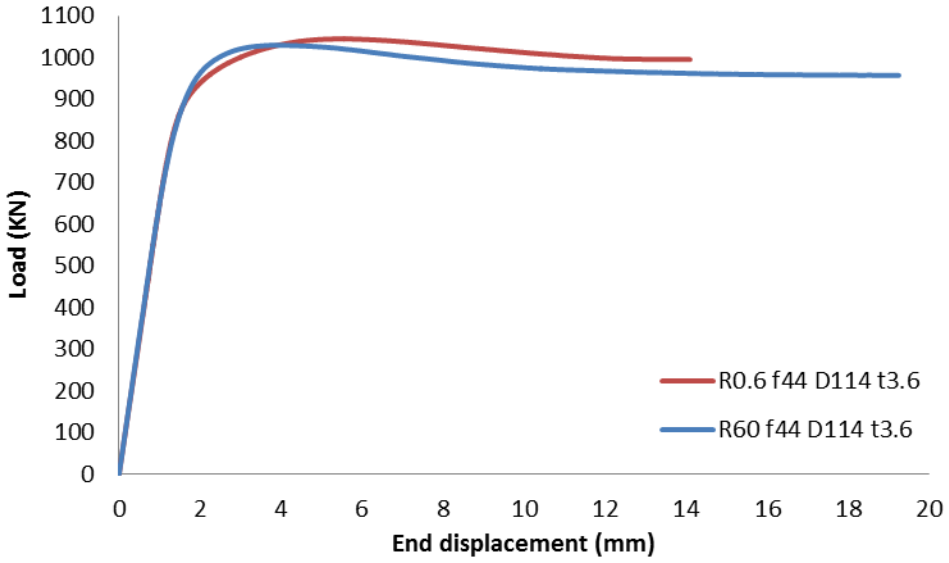

Figure 65: Load-End displacement diagram of CFST element with $^{D}/_{t}$= 32 and different loading rates

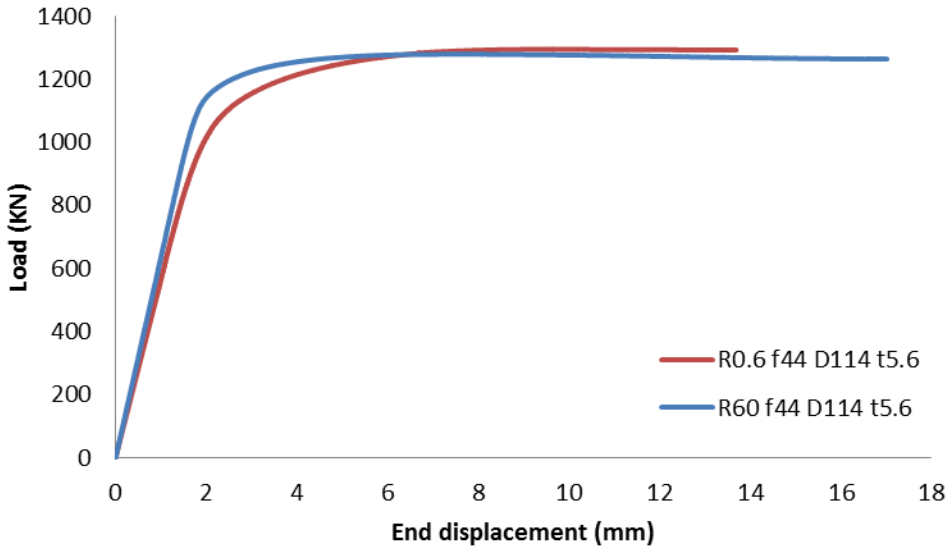

Figure 66: Load-End displacement diagram of CFST element with D/t= 20 and different loading rates

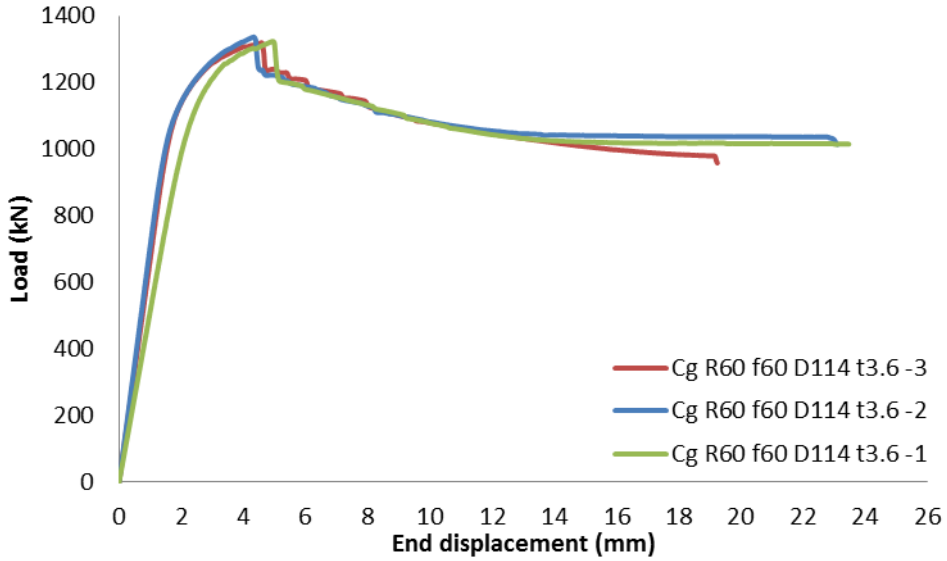

Figure 67: Load-End displacement diagram of three CCFST elements with D/t= 32, f'_c=60MPa and loading rate=60kN/s

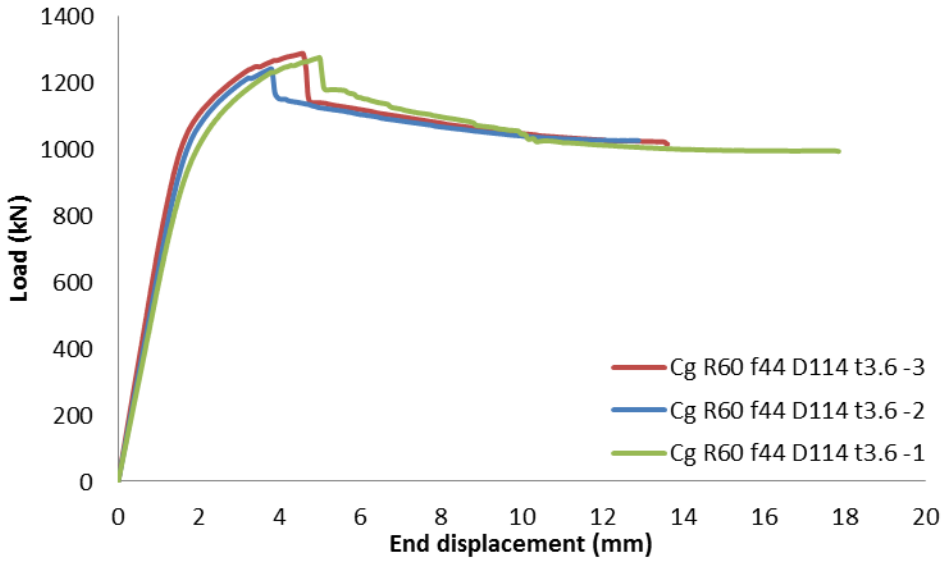

Figure 68: Load-End displacement diagram of three CCFST elements with D/t= 32, f'_c=44MPa and loading rate=60kN/s

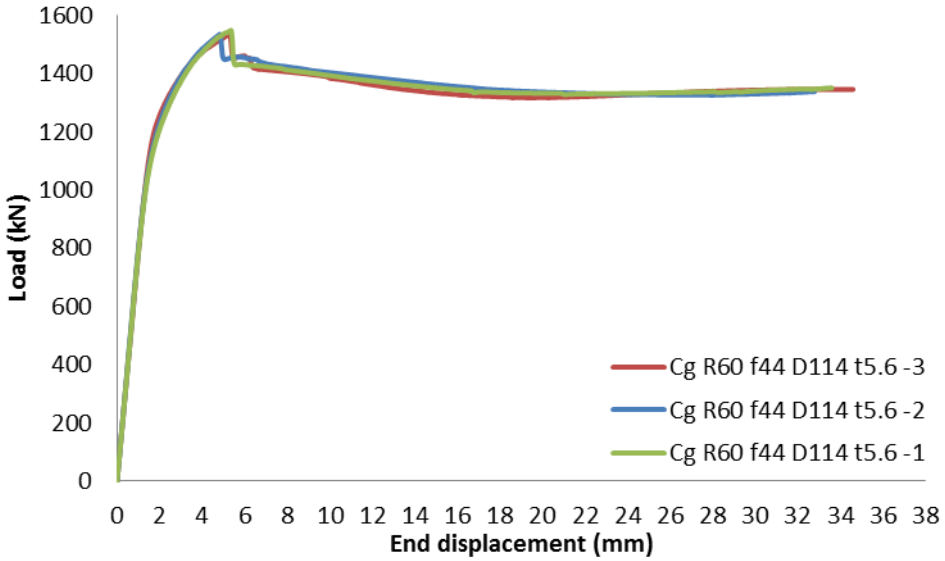

Figure 69: Load-End displacement diagram of three CCFST elements with D/t= 20, f'_c=44MPa and loading rate=60kN/s

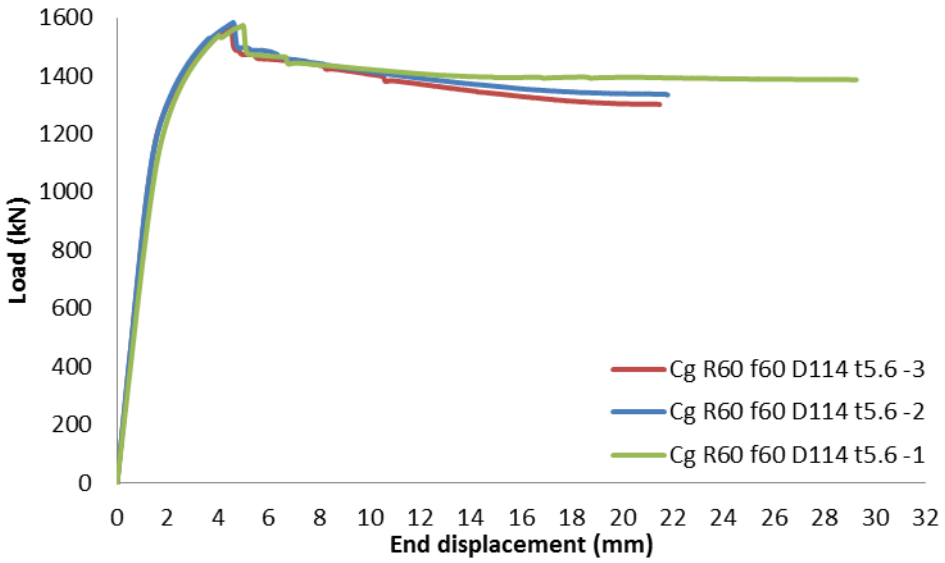

Figure 70: Load-End displacement diagram of three CCFST elements with D/t= 20, f'_c=60MPa and loading rate=60kN/s

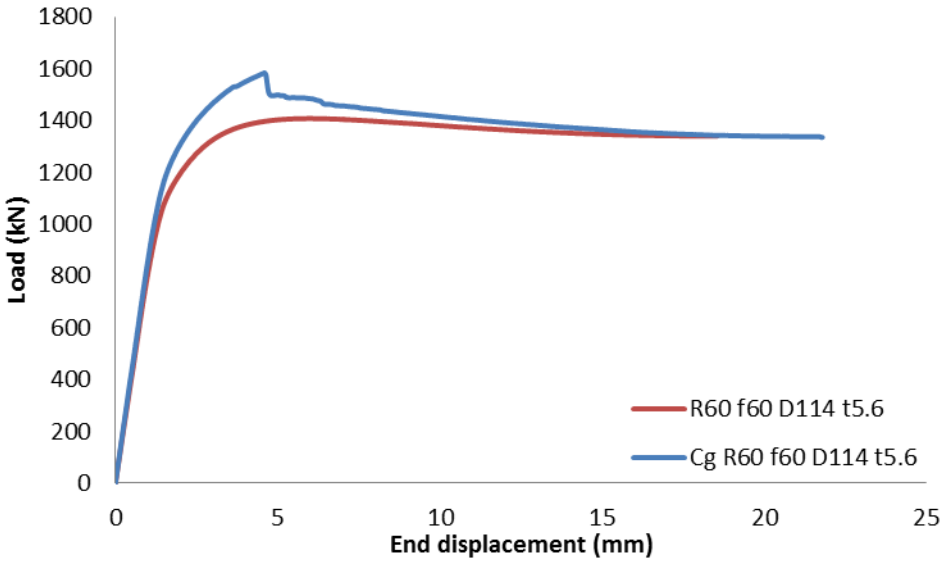

Figure 71: load-displacement diagram of a CCFST specimen and its CFST base D/t=20 & f'_c=60MPa

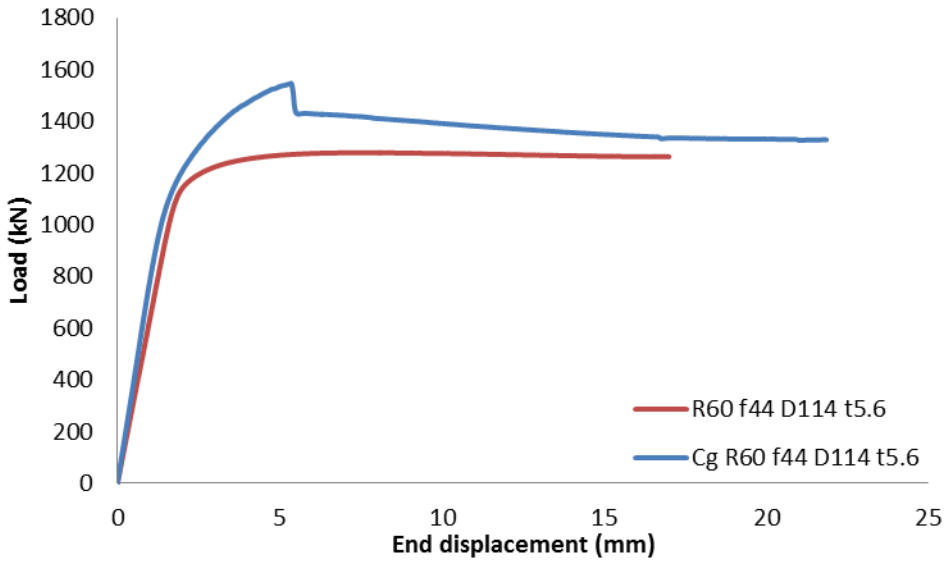

Figure 72: load-displacement diagram of a CCFST specimen and its CFST base D/t=20 & f'_c=44MPa

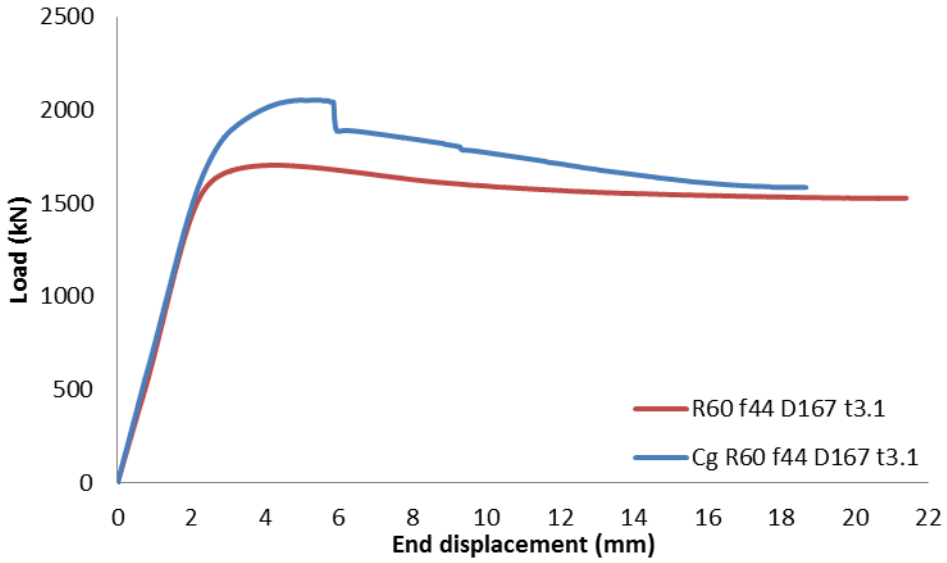

Figure 73: load-displacement diagram of a CCFST specimen and its CFST base D/t=54 & f'_c=44MPa

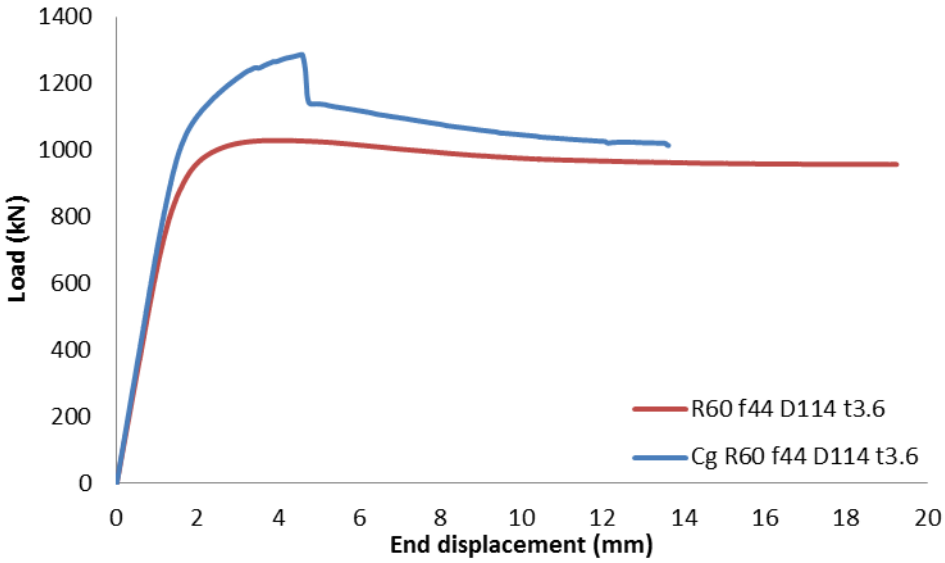

Figure 74: load-displacement diagram of a CCFST specimen and its CFST base $^{D}/_{t}$=32 & f'_c=44MPa

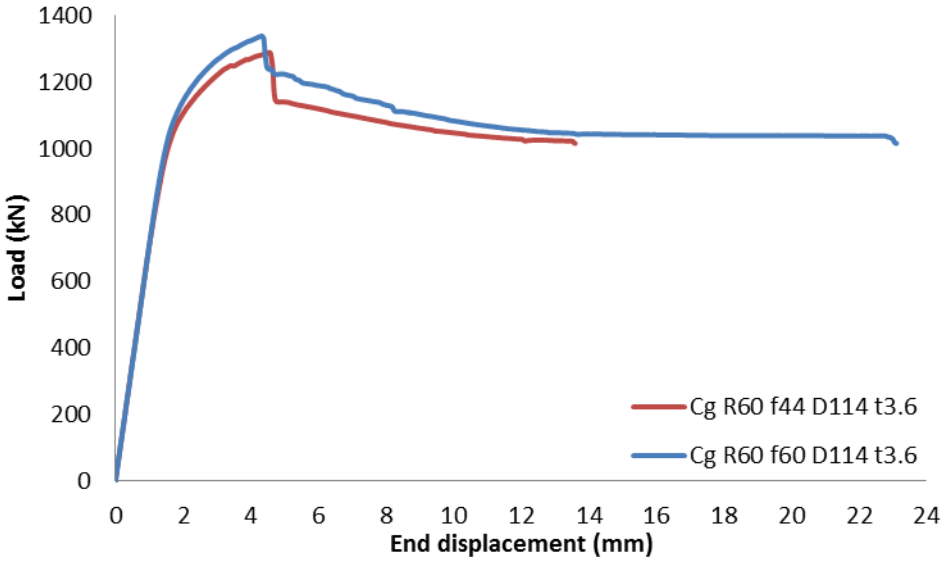

Figure 75: Load-End displacement diagram of CCFST element with $^{D}/_{t}$= 32 and different f'_c

Vita

Suliman Hassan Abdalla was born on October 8, 1987, in Sharjah, UAE. He was educated in local public schools and graduated from Helwan High School as the class valedictorian in 2005. He received a Chancellor's Scholarship to the American University of Sharjah in Sharjah, UAE, from which he graduated magna cum laude, in 2009. His degree was a Bachelor of Science in Civil Engineering. Just after his graduation, Mr. Abdalla received an Assistantship to AUS for the civil engineering master's program. In 2010, he worked as a project engineer in Al-Hashil Construction Contractor for one year. He was awarded the Master of Science degree in Civil Engineering in 2012.